STRUCTURING OF CELLULOSE NANOCRYSTAL DEPOSIT LAYERS DURING CROSSFLOW MEMBRANE FILTRATION

A THESIS SUBMITTED TO
THE GRADUATE SCHOOL OF NATURAL AND APPLIED SCIENCES
OF
MIDDLE EAST TECHNICAL UNIVERSITY

BY

BENGİSU BARIŞ

IN PARTIAL FULFILLMENT OF THE REQUIREMENTS
FOR
THE DEGREE OF MASTER OF SCIENCE
IN
CHEMICAL ENGINEERING

AUGUST 2025

Approval of the thesis:

STRUCTURING OF CELLULOSE NANOCRYSTAL DEPOSIT LAYERS DURING CROSSFLOW MEMBRANE FILTRATION

submitted by **BENGİSU BARIŞ** in partial fulfillment of the requirements for the degree of **Master of Science** i**n Chemical Engineering, Middle East Technical University** by,

Prof. Dr. Naci Emre Altun
Dean, **Graduate School of Natural and Applied Sciences** _____

Prof. Dr. Yusuf Uludağ
Head of the Department, **Chemical Engineering** _____

Prof. Dr. Pınar Zeynep Çulfaz Emecen
Supervisor, **Chemical Engineering, METU** _____

Assoc. Prof. Dr. Emre Büküşoğlu
Co-Supervisor, **Chemical Engineering, METU** _____

Examining Committee Members:

Prof. Dr. Halil Kalıpçılar
Chemical Engineering, METU _____

Prof. Dr. Pınar Zeynep Çulfaz Emecen
Chemical Engineering, METU _____

Assoc. Prof. Dr. Emre Büküşoğlu
Chemical Engineering, METU _____

Prof. Dr. Nihal Aydoğan
Chemical Engineering, Hacetttepe University _____

Asst. Prof. Dr. Necip Berker Üner
Chemical Engineering, METU _____

Date: 26.08.2025

I hereby declare that all information in this document has been obtained and presented in accordance with academic rules and ethical conduct. I also declare that, as required by these rules and conduct, I have fully cited and referenced all material and results that are not original to this work.

Name Last name : Bengisu Barış

Signature :

ABSTRACT

STRUCTURING OF CELLULOSE NANOCRYSTAL DEPOSIT LAYERS DURING CROSSFLOW MEMBRANE FILTRATION

Barış, Bengisu
Master of Science, Chemical Engineering
Supervisor : Prof. Dr. Pınar Zeynep Çulfaz Emecen
Co-Supervisor: Assoc. Prof. Dr. Emre Büküşoğlu

August 2025, 107 pages

This study investigates the formation of deposit layers from TEMPO (2,2,6,6-Tetramethylpiperidin-1-yl)oxyl)-oxidized cellulose nanocrystals (TEMPO-CNCs) and how their structures are affected by TEMPO-CNC concentration, salt concentration and deposition duration. TEMPO-CNCs obtained by TEMPO-oxidation of CNCs synthesized via sulfuric acid hydrolysis were deposited onto porous support membranes using crossflow filtration. 0.2 M $AlCl_3$ was used for the stabilization of the formed cake layers, followed by rinsing with ultrapure water. Characterization techniques including polarized optical microscopy (POM), scanning electron microscopy (SEM), and thermogravimetric analysis (TGA) were employed to investigate flux behavior, resistance, optical behavior, and solid content in the cake. $AlCl_3$ permeation raised solid content without significantly affecting cake resistance, which is attributed to a highly concentrated concentration polarization layer with comparable resistance to the cake layer. Polarized optical microscopy revealed a transition from nematic to cholesteric structure with longer deposition times, indicating structural reorganization in the cake layer. Filtration of TEMPO-CNC suspension with 100 mM NaCl concentration resulted in aggregation on the cake surface. At 5 mM NaCl, cakes prepared with different TEMPO-CNC concentrations exhibited both nematic and cholesteric ordering. The samples prepared with the suspensions of 0.30% TEMPO-CNC and various NaCl concentrations showed both nematic and cholesteric symmetries in their structures. Gel layer concentrations were

estimated around 1 wt.% from limiting flux data, while higher solid contents were calculated using the Kozeny-Carman equation and TGA. This study enabled a better understanding of the relationship between deposition durations, TEMPO-CNC concentration, salt concentration and the structural properties of TEMPO-CNC deposit layers.

Keywords: TEMPO-CNC, Crossflow membrane filtration, Cake formation, Cholesteric phase, Nematic phase

ÖZ

ÇAPRAZ AKIŞLI MEMBRAN FİLTRASYONUNDA SELÜLOZ NANOKRİSTAL BİRİKİMİNİN YAPISI

Barış, Bengisu
Yüksek Lisans, Kimya Mühendisliği
Tez Yöneticisi: Prof. Dr. Pınar Zeynep Çulfaz Emecen
Ortak Tez Yöneticisi: Doç. Dr. Emre Büküşoğlu

Ağustos 2025, 107 sayfa

Bu çalışma, TEMPO (2,2,6,6-Tetrametilpiperidin-1-oksil) ile oksitlenmiş selüloz nanokristallerinden (TEMPO-CNC'ler) çökelti tabakalarının oluşumunu ve yapılarının TEMPO-CNC konsantrasyonu, tuz konsantrasyonu ve biriktirme süresinden nasıl etkilendiğini araştırmaktadır. Sülfürik asit hidrolizi ile sentezlenen CNC'lerin TEMPO-oksidasyonu ile elde edilen TEMPO-CNC'ler, çapraz akışlı filtrasyon kullanılarak gözenekli destek membranları üzerine çökeltilmiştir. Oluşan kek tabakalarının stabilizasyonu için 0.2 M $AlCl_3$ kullanılmış, ardından ultra saf su ile durulanmıştır. Kekteki akı davranışını, direnci, optik davranışı ve katı içeriğini araştırmak için polarize optik mikroskobu (POM), taramalı elektron mikroskobu (SEM) ve termogravimetrik analiz (TGA) gibi karakterizasyon teknikleri kullanılmıştır. Yapıdan $AlCl_3$ geçirilmesi, kek direncini önemli ölçüde etkilemeden katı içeriğini yükseltmiştir, bu da kek tabakasından daha yüksek bir dirence sahip, yüksek konsantrasyonlu bir konsantrasyon polarizasyon tabakasının varlığına işaret etmiştir. Polarize optik mikroskobu, daha uzun biriktirme süreleri ile nematikten kolesterik yapıya bir geçiş olduğunu ortaya çıkarmıştır ve bu da kek tabakasında zamana bağlı yeniden yapılanmanın varlığını göstermiştir. 100 mM NaCl derişimi olan TEMPO-CNC süspansiyonunun filtrasyonu ile kek yüzeyinde agregasyon meydana gelmiştir. 5 mM NaCl ve farklı TEMPO-CNC konsantrasyonları ile hazırlanan kekler hem nematik hem de kolesterik düzen sergilemiştir. %0.30'luk TEMPO-CNC süspansiyonları ve çeşitli NaCl konsantrasyonları ile hazırlanan örneklerin yapılarında

hem nematik hem de kolesterik düzen görülmüştür. Jel tabakası konsantrasyonları, sınırlayıcı akı verilerinden ağırlıkça yaklaşık %1 olarak tahmin edilirken Kozeny-Carman denklemi ve TGA kullanılarak daha yüksek katı içeriği hesaplanmıştır. Bu çalışma, çökelme süreleri, TEMPO-CNC ve tuz konsantrasyonu ile TEMPO-CNC kek tabakalarının yapısal özellikleri arasındaki ilişkinin daha iyi anlaşılmasını sağlamıştır.

Anahtar Kelimeler: TEMPO-CNC, Çapraz akışlı membran filtrasyonu, Kek oluşumu, Kolesterik faz, Nematik faz

To myself, for the journey, and to the people who shaped me into who I am - especially my little sister, Alin

ACKNOWLEDGMENTS

I would like to express my deepest gratitude to my supervisor, Prof. Dr. Pınar Zeynep Çulfaz Emecen, for her constant guidance, encouragement and belief in me throughout this project. I am also sincerely thankful to my co-advisor, Assoc. Prof. Dr. Emre Büküşoğlu, for his patience and encouragement. I feel lucky to have had both of my advisors by my side, opening the doors of the academic world for me.

I want to thank the members of the Membrane for Energy and Water Laboratory, especially Aytöre Arıkan, for her endless motivational speeches, and Rafid Gertani, for making the work in the laboratory lighter and more fun. I am also thankful to the Soft and Functional Materials Laboratory members, particularly Ayşe Nurcan Özşahin Işılak, for her friendship and for always being there when I needed help.

My endless thanks go to my close friends Deniz Ünal, Gülce İlhan, Metin Alp Yurtseven, and Yarengül Çiçek Kurt for being by my side for years and for loving me unconditionally. I am grateful to my close friends Berk Can İçten, Hüseyin Öztürk, and Toprak Çağlar for bringing more joy to my good days and ease to my difficult ones. I am glad to have met and shared this journey with Alican Ertaş, Almira Çaldıklıoğlu, and Selin Karahan.

I feel so lucky to have Oğuzhan Coşğun in my life as both my best friend and my love. This thesis would not have been completed without his constant support and encouragement. He has always made me believe in myself and inspired me to become a better version of who I am every single day.

Finally, and most importantly, I want to thank the greatest gifts of my life: my mother, Zeynep Barış, my father, Mehti Barış, and my sister, Alin Barış. I am endlessly grateful to my parents for raising me with unconditional love, endless care and support. And to my little sister Alin - thank you for making me the luckiest person in the world just by being you. You bring so much love, joy, and light into my life. Everything I have achieved and will achieve is because of them, and nothing makes me happier than sharing this accomplishment with my family.

TABLE OF CONTENTS

LIST OF TABLES

TABLES

LIST OF FIGURES

FIGURES

LIST OF ABBREVIATIONS

ABBREVIATIONS

$AgNO_3$	Silver Nitrate
$AlCl_3$	Aluminum Chloride
CA	Cellulose Acetate
$CaCl_2$	Calcium Chloride
CNC	Cellulose Nanocrystal
Cu	Copper
DLVO	Derjaguin–Landau–Verwey–Overbeek
DMSO	Dimethyl Sulfoxide
H_2SO_4	Sulfuric Acid
HCl	Hydrochloric Acid
HNO_3	Nitric Acid
$K_2S_2O_8$	Potassium Persulfate
LMH	$\frac{L}{h \times m^2}$
N_2	Nitrogen
NaBr	Sodium Bromide
NaCl	Sodium Chloride
NaOCl	Sodium Hypochlorite
NaOH	Sodium Hydroxide
NIR	Near-infrared
PIV	Particle Image Velocimetry
POM	Polarized Optical Microscopy
PWP	Pure Water Permeance
SALS	Small Angle Light Scattering
SAXS	Small Angle X-ray Scattering

SEM	Scanning Electron Microscopy
TEMPO	(2,2,6,6-Tetramethylpiperidin-1-yl)oxyl
TEMPO-CNC	TEMPO-oxidized Cellulose Nanocrystal
TGA	Thermogravimetric Analysis
TMP	Transmembrane Pressure
US	Ultrasound
$\boldsymbol{SC}$	Solid Content

LIST OF SYMBOLS

SYMBOLS

C_{bulk}	Bulk concentration
C_f	Feed concentration
C_{gel}	Gel concentration
C_p	Permeate concentration
D_{ij}	Diffusion coefficient of solute in solvent
$J_{limiting}$	Limiting flux
$R_{fouling\ layer}$	Resistance of the fouling layer
$R_{membrane}$	Resistance of the support membrane
R_{total}	Total resistance
k_c	Mass transfer coefficient
α_f	Specific resistance
δ_{cake}	Cake layer thickness
ε_{vol}	Volume-based porosity
$\rho_{TEMPO-CNC}$	Skeletal density
ρ_{pore}	Pore density
ΔP	Transmembrane pressure
k	Extinction coefficient
p	Pressure
A	Surface area of the membrane
J	Permeate flux
K	Kozeny-Carman constant
P	Permeance
R	Resistance
S	Internal surface area

$\boldsymbol{V}$	Permeate volume
$\boldsymbol{p}$	Cholesteric pitch
$\boldsymbol{s}$	Cake compressibility
$\boldsymbol{t}$	Time
$\boldsymbol{\mathcal{R}}$	Rejection (%)
$\boldsymbol{\beta}$	Empirical coefficient
$\boldsymbol{\varepsilon}$	Porosity
$\boldsymbol{\eta}$	Dynamic viscosity
$\boldsymbol{\mu}$	Permeate viscosity

CHAPTER 1

INTRODUCTION

1.1 Membranes and Membrane Separation

Membranes are semi-permeable barriers that act as a physical barrier between two phases by controlling the rate of permeation of different species. Hence, they are widely used in industrial applications, especially in areas where they are more beneficial than the conventional unit operations in chemical engineering. Their key role is to change the composition of the mixtures by the relative permeation rate of the species (Baker, 2012). Therefore, their main advantage is this selective transport, and they are widely utilized in domestic and industrial water treatment; chemical and metallurgical, biotechnological, pharmaceutical, food and beverage industries. Transport through membranes generates a driving force and this driving force is the result of chemical potential difference across the membrane which can be due to concentration or pressure gradient or electrical field (Mulder, 1996). Some of the remarkable benefits of the membrane separation processes are low energy requirement without a temperature or phase change and being a continuous process at mild conditions without needing an additive.

In the membrane separation processes, there are three important parts: feed, permeate and retentate. The feed is the mixture that contains two or more species which will be separated at the end of the process. Permeate is the part that can pass through the membrane structure. The part that cannot pass through the membrane is called retentate. After the separation, the retentate will be the concentrated portion. Therefore, it can also be defined as concentrate.

Membranes can be categorized according to their morphology: Isotropic (symmetric) membranes and anisotropic (asymmetric) membranes. They are schematically

represented in Figure 1-1 where it is seen that isotropic membranes can be either microporous or nonporous. Microporous membranes have randomly distributed pores, and the separation occurs mainly due to the molecular sizes. Molecules having much smaller sizes than the pores can generally pass through the membrane while the others are rejected (Baker, 2012). On the other hand, nonporous membranes have a dense selective layer, and the separation occurs according to the solubility and diffusivity differences between feed components (Baker, 2012). Thin-film composite anisotropic membranes are commonly used in commercial applications due to higher fluxes. In this kind of membranes, there is a thin surface layer over a support layer that is critical in separation performance. The separation properties are highly affected by the surface layer properties. Generally, the support and surface layers are formed by different polymers. For the polymer choice, mechanical, physical and chemical properties should be considered for the specific usage and purpose of the membranes. For example, tolerance to temperature and pH changes, good flexibility and good chemical resistances are some of the crucial properties of the membrane since a high-performing membrane should be compatible with the changes in the operation environment and parameters (Hadi et al., 2024; Purkait et al., 2018).

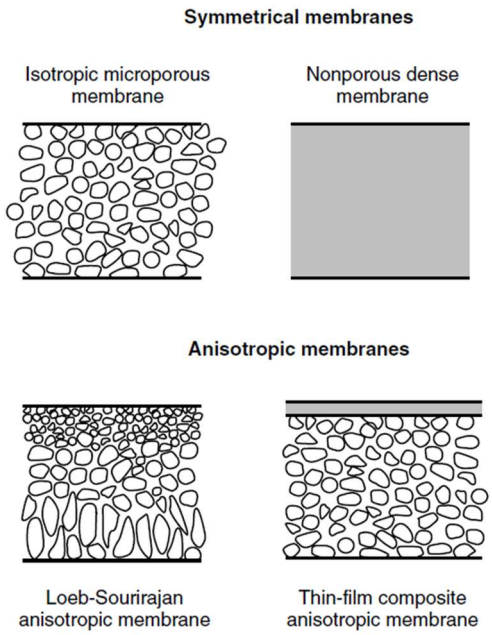

Figure 1-1. Schematic representation of different membrane types

Another type of asymmetric membranes is anisotropic or integrally skinned asymmetric membranes which are first developed by Loeb and Sourirajan (Loeb & Sourirajan, 1963). These membranes have a gradually transitioned structure from a relatively dense structure to a fully porous structure as seen in Figure 1-1. These membranes can be fabricated with the phase inversion method and used as ultrafiltration membranes (Baker, 2012).

1.1.1 Dead End and Crossflow Membrane Filtration

There are two modes of operation in membrane processes: dead-end and crossflow filtrations. In dead-end or in-line filtration mode, all feed is forced through the porous structure of the membrane under pressure without a tangential flow. As filtration proceeds, the concentration of the rejected particles increases in the feed and permeate flux starts to decrease since the rejected particles start to accumulate on the membrane surface or inside the porous structure of the membrane (Mulder, 1996). The pressure which is required for the desired flux is increased due to this accumulation. Hence, crossflow mode might be more preferrable for industrial applications since there exists a feed flow not only through the pores but also tangential to the membrane and this

tangential flow creates a sweeping effect that reduces the particle accumulation. In crossflow filtration, the feed stream is circulated along the membrane and separated into two streams which are permeate stream containing no particle and a concentrated retentate stream containing many particles. Dead-end and crossflow filtration modes are schematically given in Figure 1-2 for a representative microfiltration process.

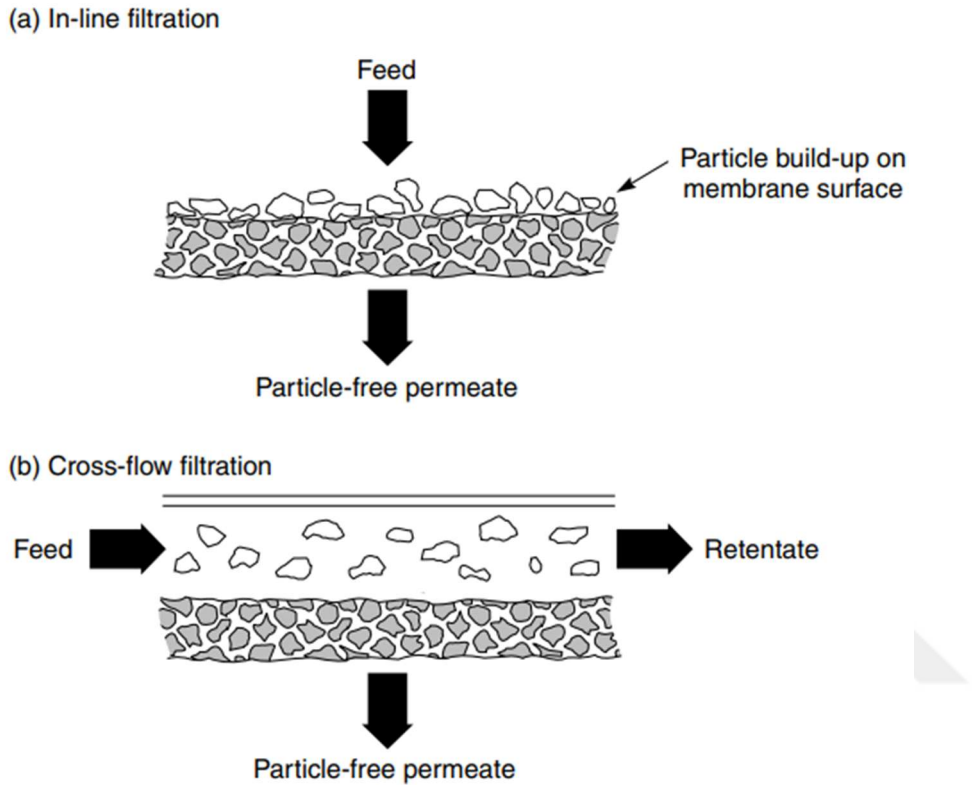

Figure 1-2. Schematic representation of filtration modes in a microfiltration process. (a) Dead-end (in-line) filtration and (b) Crossflow filtration (Baker, 2012)

1.2 Concentration Polarization, Limiting Flux and Membrane Fouling

In both dead-end and crossflow filtrations, there might be a chance of rejected particles' accumulation onto the membrane surface. These extra particle layers result in remarkable changes in the membranes' properties such as flux, resistance or rejection performance.

Average fluid velocity through a porous media like membranes was correlated with average pressure drop through the porous media by Darcy. Thus, Darcy's Law can be used to correlate the flux (J) and resistance (R) of the membranes:

$$R = \frac{\Delta P}{\mu . J} \qquad (1)$$

Where ΔP is the transmembrane pressure, μ is the permeate liquid viscosity and J is the permeate flux.

The permeate flux can be calculated as the following:

$$J = \frac{permeate\ volume}{membrane\ area . time} = \frac{V}{A . t} \qquad (2)$$

Finally, the permeance (P) can be defined as:

$$P = \frac{J}{\Delta P} \qquad (3)$$

For the membrane and fouling layer, there are individual resistances. The resistances can be taken as resistances in series for the calculations:

$$R_{total} = R_{membrane} + R_{fouling\ layer} \qquad (4)$$

Another critical property of the membranes are their rejection performances. This performance is measured by rejection ($\mathcal{R}$).

$$\mathcal{R} = \left(1 - \frac{C_p}{C_f}\right) \times 100 \qquad (5)$$

Where C_p and C_f are the concentrations of the contaminant that is desired to remove from the solution in the permeate and feed, respectively.

During membrane filtration, mass transfer from bulk occurs because of the flow that exists due to the pressure gradient. At the same time, rejected species' concentration increases on the support surface. Meanwhile, the back diffusion also occurs from the support surface to the bulk due to concentration gradient. As a result of balance between mass transfer from bulk and back diffusion from the membrane surface, the surface concentration starts to increase. This is called concentration polarization phenomena. As a result of the concentration polarization, accumulation or build-up of substances on the membrane surface is seen and this build-up or deposition is called membrane fouling (Motsa et al., 2018). If this deposition occurs inside the membrane

pores, this is called internal fouling and if it is deposited on the membrane surface, it is named as external fouling (Tayeh et al., 2025). Furthermore, fouling can be classified according to foulant types: organic, scaling or inorganic, biological and colloidal fouling (Nthunya et al., 2022). Fouling can occur due to the build-up of one type of substances, or it can occur due to the accumulation of more than one type of foulant such as combined fouling of organics and colloids (Mahlangu et al., 2015). Membrane fouling mechanisms can be classified under four main categories: complete blocking, intermediate blocking, standard blocking and cake formation (Aliasghari Aghdam et al., 2015). These mechanisms are schematically summarized in Figure 1-3.

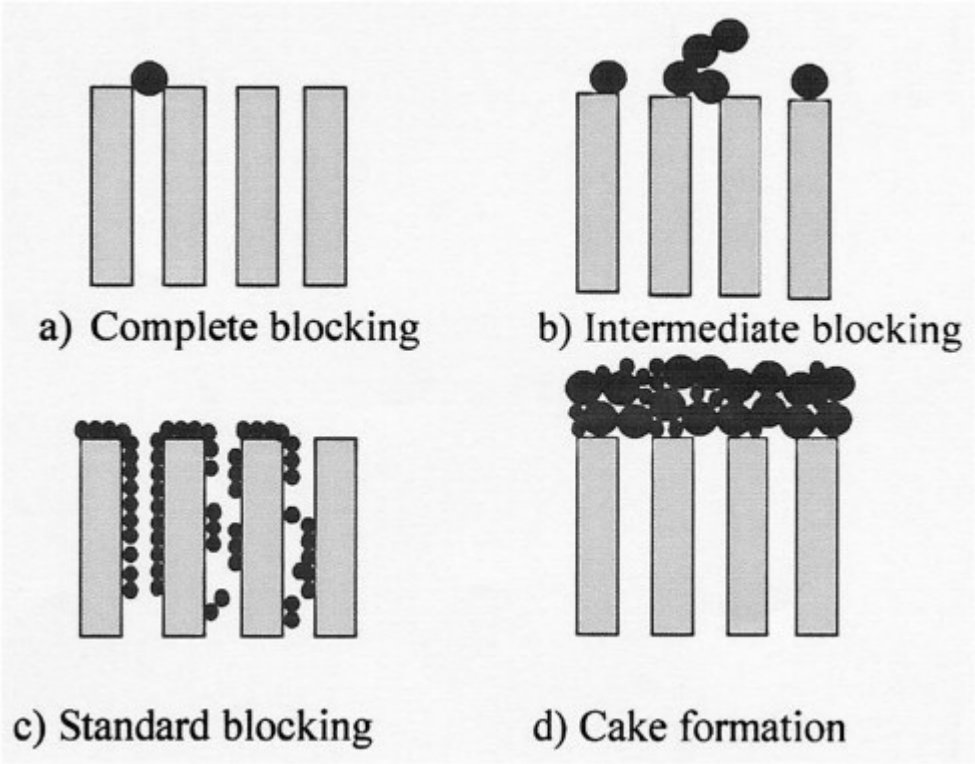

Figure 1-3. Schematic representation of fouling mechanisms (Aliasghari Aghdam et al., 2015)

Membrane fouling can be divided into two according to the degree of attachment of the foulants onto membrane: reversible and irreversible fouling (Al-Najar et al., 2020). Reversible fouling can be removed with physical removal methods such as backwashing, air flushing or relaxation for different types of membrane processes (Gul et al., 2021). The removal can be done with the help of chemicals such as acidic or alkaline solutions like HCl, HNO_3 or NaOH solutions (Blanpain-Avet et al., 2009) or

mixtures of acidic and alkaline solutions together with some surfactants (Madaeni et al., 2001).

As the surface concentration increases due to the concentration polarization, permeate flux of the membrane decreases. This deviation from membrane pure water flux can be seen in Figure 1-4. Moreover, the gel or cake layer formation occurs if the concentration of the rejected species' concentration exceeds the solubility limit or gel concentration in the solvent (Baker, 2012). The cake layer is assumed to be soft and compressible and for the compressible cakes, the specific cake layer resistance increases as the pressure increases (Iritani et al., 1993; Sioutopoulos et al., 2010). This physical relation has been correlated with the following equation:

$$\propto_f = \frac{R}{\delta_{cake}} = \beta \Delta P^s \quad (6)$$

where $\propto_f$ is specific cake layer resistance, β is the empirical coefficient, ΔP is the transmembrane pressure and s is the cake compressibility (Belfort et al., 1994; Sioutopoulos & Karabelas, 2016; Yang et al., 2022). As seen in Equation 6, when the compressibility factor, s, is equal to 0, which means the cake is incompressible, specific cake layer resistance cannot depend on the operating pressure.

The gel layer formation results in "limiting flux" which is the maximum flux that can be achieved with any operating conditions. When the limiting flux is achieved, it cannot be altered by increasing the operating pressure. Increase in pressure after the limiting flux only results in an increase in the thickness of the cake layer.

As seen in Figure 1-4, a small pressure like p_1 does not result in high flux and the effect of concentration polarization is too small for gel layer formation. Moreover, there is only a slight deviation from the membrane's pure water flux. When the pressure is increased further to p_2, the flux increases and effects of concentration polarization are not negligible anymore. Rejected particles' concentration starts to increase on the surface. Finally, if the pressure increases up to p_3, concentration polarization becomes enough to form a gel layer on the surface. At this point, the limiting flux is reached and further increase in the pressure creates thicker gel layer, not higher permeate flux. If this gel layer is not desirable for an application, then, the operating conditions should

be chosen with caution. In order to eliminate gel formation chance, the applied pressure should be between p_2 and p_3, most preferably just below p_3 for better long-term performances (Baker, 2012).

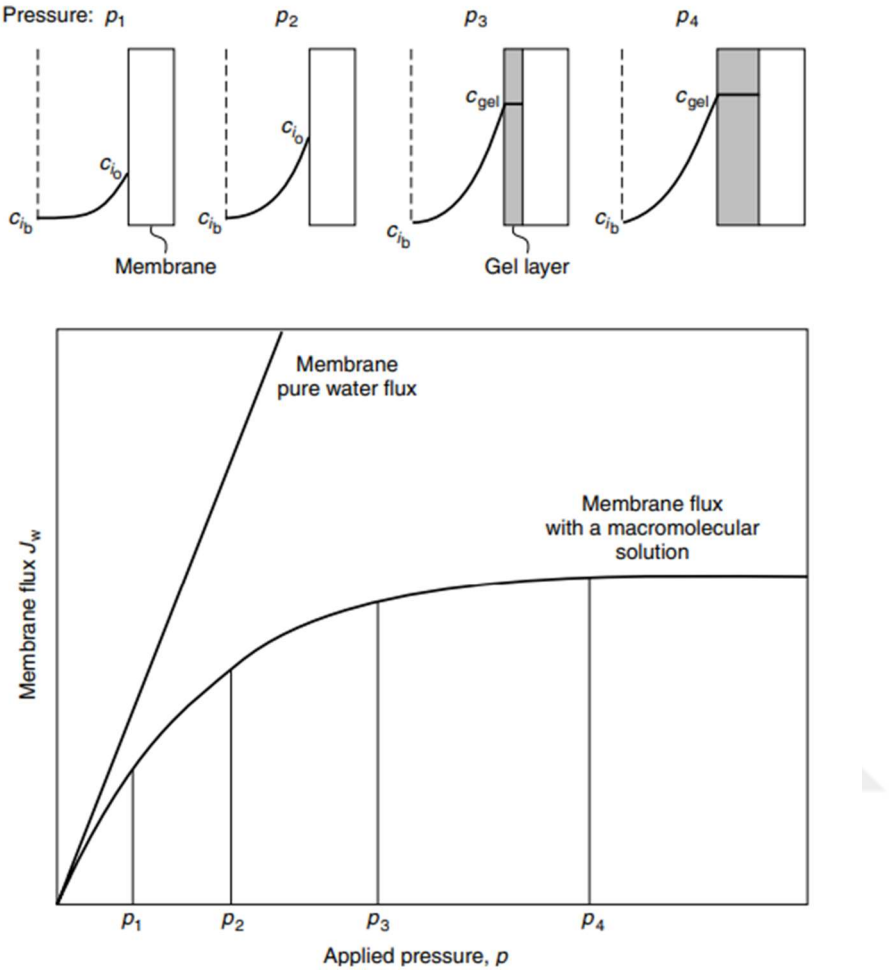

Figure 1-4. The effect of pressure on the permeate flux of the membrane in ultrafiltration (Baker, 2012)

The formed gel layer's concentration can be predicted by Equation 7, if the rejection of the species is 100% (Baker, 2012).

$$\frac{C_{gel}}{C_{bulk}} = \exp\left(\frac{J\delta}{D_{ij}}\right) = \exp\left(\frac{J}{k_c}\right) \quad (7)$$

In Equation 7, C is the concentration of the species either in the gel layer or in the bulk, J is the flux, D_{ij} is the diffusion coefficient of the solute in the solvent and k_c is the mass transfer coefficient.

Concentration polarization is not desired in membrane processes since it results in membrane fouling and decline of membrane performance. Generally, it leads to replacement of the membrane at the end and diminishes the cost efficiency of the process (Mulder, 1996). Hence, crossflow filtration mode is preferred since it allows to control membrane fouling at some extent by manipulating the mass transfer with the choice of crossflow velocity. On the other hand, concentration polarization can be quite useful for some applications (May et al., 2021). For instance, it can be helpful in the preparation of the composite membranes. The gel layer can be utilized as a thin selective layer onto a porous support layer (İçten et al., 2024; Kocaman et al., 2021). For these membranes, the morphology of this gel layer is one of the most important parameters that affects the permeance and rejection performance of the membranes. The thickness, tortuosity and porosity of the gel layer have crucial effects on the membrane permeance and rejection performances. Therefore, knowing this information helps to characterize the prepared membranes.

1.3 Characterization of the Cake Layer with Kozeny-Carman Equation

The porosity of cake layer can be determined by the Kozeny-Carman equation if the specific cake layer resistance is known for the membranes. This equation was developed by Carman in 1937, after Hagen-Poiseuille equation and Darcy's law concept were combined by Kozeny in 1927 (Carman, 1997).

$$\frac{J}{\Delta P/_{\Delta x}} = \frac{\varepsilon^3}{K.\eta.S^2.(1-\varepsilon)^2} \qquad (8)$$

In Equation 8, ε is the volume of pore space per volume of the cake i.e., porosity, K is the Kozeny-Carman constant, S is the internal surface area, and η is dynamic viscosity (Carman, 1997; Mulder, 1996).

1.4 Anisotropic Colloids in Crossflow Filtration

Previous studies showed that anisotropic colloids can be utilized in crossflow filtrations for various purposes: to characterize the fouling formation mechanisms or

to directly characterize the fouling layer structure and morphology. In some cases, this deposited cake/gel layer of colloids were utilized as the selective layer for the membrane separation processes (İçten et al., 2024; Kocaman et al., 2021).

1.4.1 Cellulose Nanocrystals and Their Properties

Cellulose nanocrystals (CNCs) have optical properties that can be useful for characterization of the fouling layer and its formation mechanisms, and tuning the membrane performances of the fouling layers utilized as selective layer of the separation.

CNCs are nano rods that are derived from lignocellulosic natural resources. They are generally rod-shaped with a diameter of 5−15 nm and length of 100−300 nm. They are commonly used in many engineering applications due to their renewability, abundance, high surface area, low toxicity, biocompatibility and optical properties (Parker et al., 2018). They form one of the colloidal lyotropic liquid crystal phases with self-organized helical structure after a specific concentration due to being intrinsically chiral on molecular level and having asymmetric surface charge distribution (Lagerwall et al., 2014; Parton et al., 2022a). The mesophase chirality in the repeating glucose unit is transferred from molecular level to colloidal level which induces a helical twist and cholesteric self-assembly of CNCs at colloidal level (Abbasi Moud, 2022; Parton et al., 2022b). Liquid crystals can flow like a liquid but possess characteristic long-range ordering reminiscent of solid crystals. Lyotropic liquid crystal phases occur when the rod-shaped particles exist in a solvent, and their concentration determines the phase transitions (Hamley, 2013). In the nematic phase, the anisotropic particles possess a long-range orientation order towards the same direction called director. In chiral nematic (cholesteric) phase, the rod-shaped particles have a chiral structure which can be described as the helical twist occurs along the axis perpendicular to the local director. As seen in Figure 1-5 (c), CNCs show a cholesteric helical structure after a critical concentration. An important property of this cholesteric helical structure is cholesteric pitch (p). Cholesteric pitch is the distance along the helical axis between the nanorods that have the same orientation after a full 360°

rotation (Parker et al., 2018). This structured cholesteric phase exhibits the birefringence due to the alignment of the nanorods, and it is easily recognizable under POM (Polarized Optical Microscopy) with the presence of characteristic fingerprint pattern which can be seen in Figure 1-5 (c) (Revol et al., 1992).

As seen in Figure 1-5 (a), aqueous suspensions of CNCs that are synthesized by sulfuric acid hydrolysis show isotropic phase at lower concentrations in which CNCs are randomly distributed in the suspension due to the electrostatic repulsion between the negatively charged sulfate groups (Parker et al., 2018). As concentration increases, the phase transition from isotropic to biphasic region occurs due to the decreasing repulsive interactions between the crystals. Both isotropic and liquid crystalline phases coexist in the biphasic region. For more increased concentrations, phase transition from biphasic to anisotropic phase takes place (Habibi et al., 2010; Parker et al., 2018).

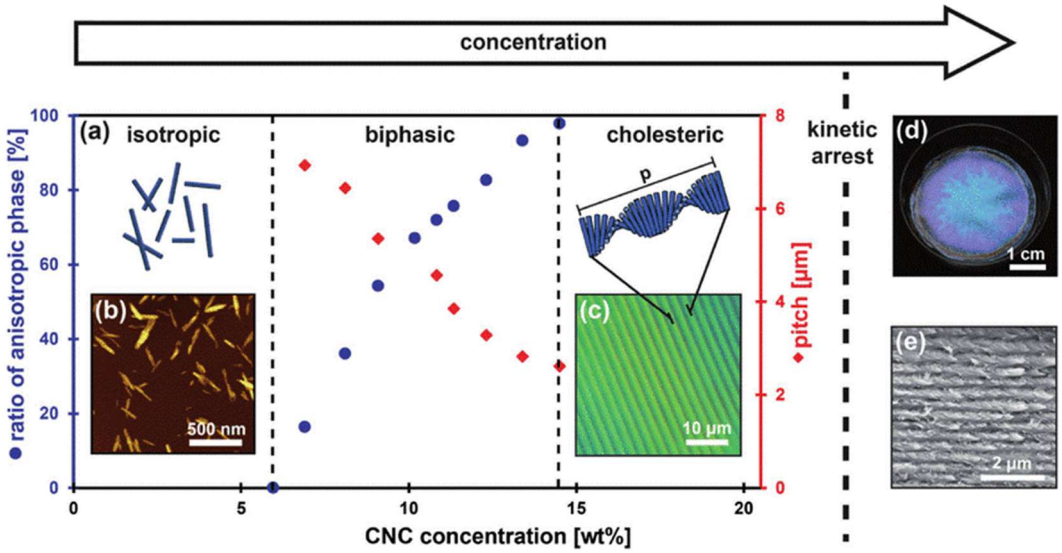

Figure 1-5. The self-assembled chiral nematic (cholesteric) helical structure of CNCs. (a) Phase diagram showing the transition from isotropic phase to cholesteric phase with increasing concentration (blue) and corresponding pitch (red) (b) AFM image of CNCs (c) POM image of the fingerprint pattern of cholesteric CNCs (d) POM image of dried CNC film (e) Cross-section SEM image of the dried CNC film that shows the characteristic Bouligand arches (Parker et al., 2018).

Cholesteric colloidal CNCs have the ability to sustain their helical structure after drying. It was seen that the dried film showed iridescent behavior under POM as seen in Figure 1-5 (d). This is caused by Bragg reflection phenomena which occurs in

periodical structures, and it takes place by the selective reflection of incident light of certain wavelengths. The wavelength of the reflected light depends on refractive indices, the angle between the incident light and the surface, and pitch of CNC (Wang et al., 2025). This dependence can be seen in the following equation for a cholesteric liquid crystal:

$$\lambda = 2n.\left(\frac{p}{2}\right).sin\theta \quad (9)$$

In Equation 9, λ is the wavelength of reflected light, n is the average refractive index of the material, p is the cholesteric pitch of the material and θ is the angle between incident light and the surface (St. John et al., 1995; Thiruganasambanthan et al., 2022a). Note that the average refractive index of CNC films was reported to be close to 1.56 in numerous studies (Dumanli et al., 2014; Espinha et al., 2016; Solhi et al., 2023; Thiruganasambanthan et al., 2022b).

Furthermore, the cross-section SEM image of the dried CNC film showed the presence of Bouligand arches as seen in Figure 1-5 (e). Both observations proved that cholesteric structure of CNCs were sustained during the drying process.

As mentioned previously, the optical properties of CNCs are highly dependent on the helical pitch since the reflection color changes with changing helical pitch. Hence, observing the Bragg reflection of a CNC based material under polarized optical microscopy allows to comprehend the structure of CNCs. In addition, this helical pitch of the CNCs is tunable with various methods for different applications. One of the studies showed that addition of D-(+)-glucose to 5.2 wt % CNC casting suspensions results in red color shift in the appearance of casted films under POM (Mu & Gray, 2014). It is known that the addition of electrolytes like NaCl, KCl or HCl decreases the cholesteric pitch of CNC suspensions and results in blue color shift (Xue et al., 1996). Blue color shift also occurs in CNC films while they are drying. The rate of drying is also crucial for the change in pitch size. A recent previous study showed that rapid drying of CNC films resulted in non-homogenous color shift and rainbow films, but slow and humidity-controlled drying created more uniform blue color shift and evenly blue colored films (Chang & Oh-e, 2022). Thus, the optical properties of dried CNC films are dependent on both the drying environment and also the drying rate.

1.5 Characterization of Chiral Self-Assembly of CNC during Filtration

In the literature, crossflow ultrafiltration of starch nanocrystal (SNC) and cellulose nanocrystal (CNC) with ultrasound (US) was reported in 2015 (Hengl et al., 2014; Jin et al., 2014). Real time *in-situ* small angle X-ray scattering (SAXS) was utilized to nanoscale investigation of filtration together with macro scale analysis with flux behavior. Both macro scale and nanoscale analysis results of 0.7% CNC filtration at 1.1 bar with 0.3 L/min were presented in Figure 1-6 (Jin et al., 2015).

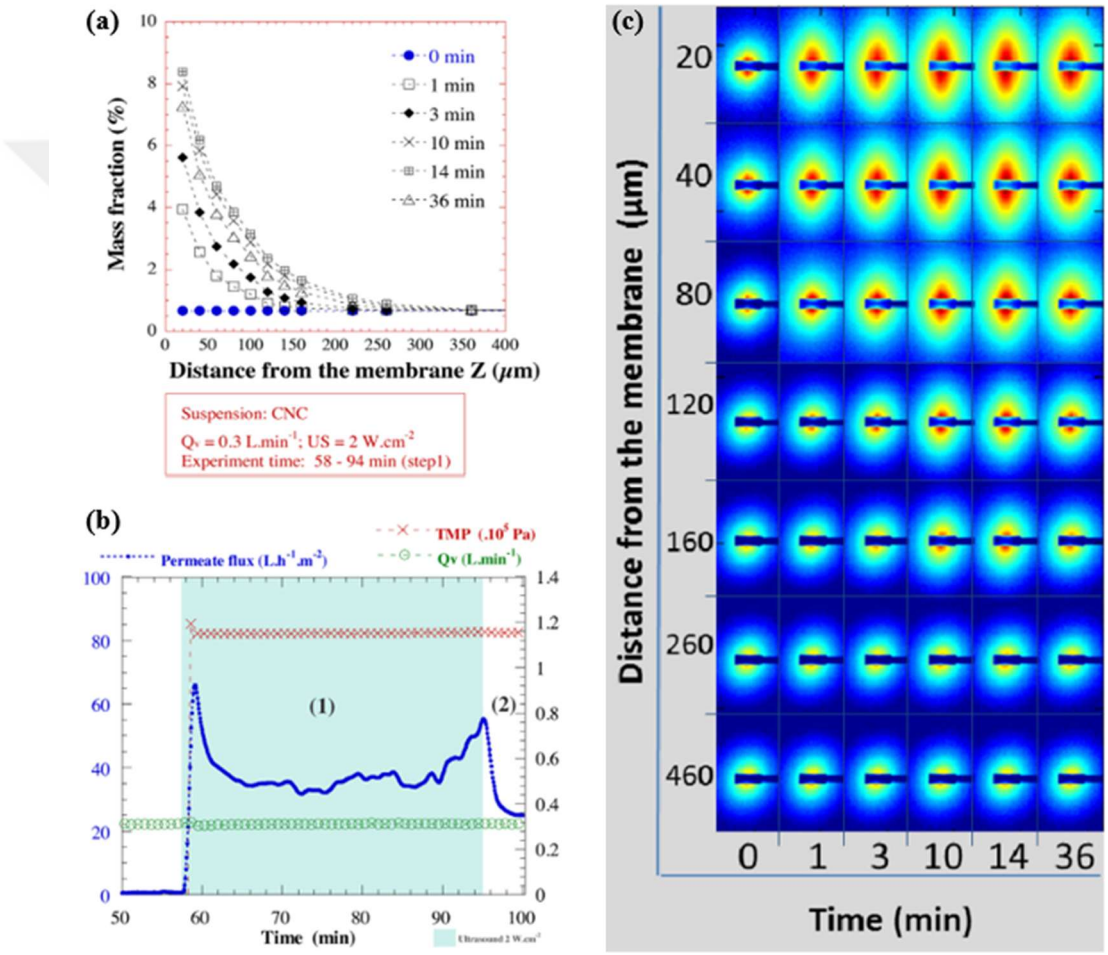

Figure 1-6. Macro and nanoscale results of 0.7% CNC filtration at 1.1 bar with 0.3 L/min. (a) Filtration curve. Green region indicates the presence of ultrasound application. (b) Concentration profile. (c) SAXS patterns for different distances from the membrane (Jin et al., 2015).

It was reported that there existed a sharp decline in the permeate flux when the TMP (transmembrane pressure) was applied due to formation of concentrated layer when the filtration started. This concentration increase can be seen in Figure 1-6 (a), even at the first minute of the filtration (black empty squares). As filtration took place, both the concentration and the thickness of formed layer continued to increase with increasing time. As seen in Figure 1-6 (b), CNC particles formed aggregates due to applied TMP, before applying US. When the US application started at region (1) (green region), a progressive disruption of CNC aggregates took place and at the end of region (1) dispersion of CNCs was achieved. It was reported that permeate flux has declined from 55 LMH to 25 LMH at the beginning of region (2) due to the removal of applied US. The rest of the filtration results were provided in Figure 1-7.

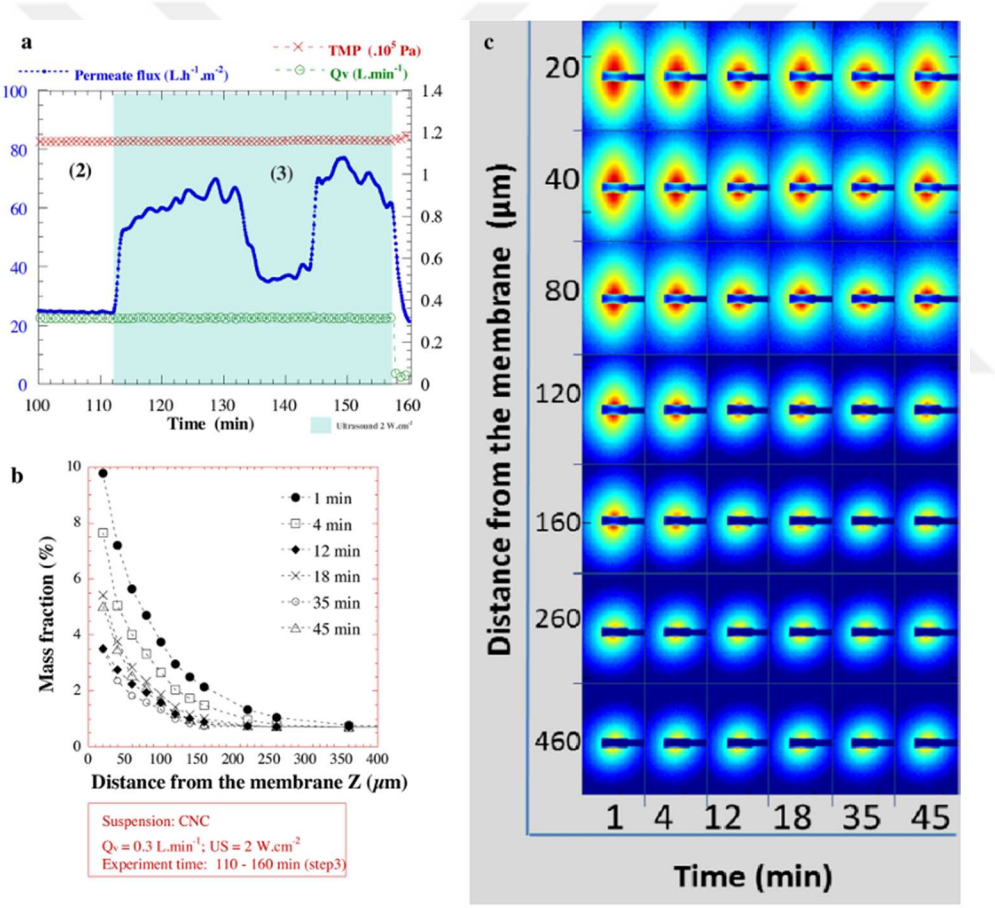

Figure 1-7. Macro and nanoscale results of 0.7% CNC filtration at 1.1 bar with 0.3 L/min. (a) Filtration curve. Green regions (2 and 3) indicate the presence of ultrasound application. (b) Concentration profile. (c) SAXS patterns for different distances from the membrane (Jin et al., 2015).

Some kind of reorganization has observed in the concentration profile as seen in Figure 1-7 (b) when the US application started which was also in line with the oscillatory behavior in the permeate flux as visible in Figure 1-7 (a). These behaviors in the flux and concentration can be explained by the competition between ultrasonic force, hydrodynamic force and convective force (Jin et al., 2014).

As seen in SAXS patterns given in Figure 1-6 (c), there existed a preferential orientation in the X-ray scattering patterns when the filtration without US started at t=0 min. as the filtration proceeded, it was observed that the anisotropic appearance in the X-ray scattering patterns were increased. This increasing anisotropy indicated that alignment of CNCs have occurred during the filtration. This concluded that higher concentration yielded in higher anisotropy in the CNC structure (Jin et al., 2015).

Another study conducted about the crossflow ultrafiltration of CNCs revealed the concentration and velocity profiles of concentration polarization and fouling layers with *in situ* Small Angle X-ray Scattering (SAXS) and second time-resolved *in situ* micro–Particle Image Velocimetry (micro-PIV). Concentration profile, SAXS pattern and permeate flux data of 0.7 wt.% (0.437 vol.%) CNC filtration at 1.1 bar were given in Figure 1-8. Due to applied transmembrane pressure, lowering of membrane (350 μm) was observed in that study. As seen from the concentration profile (Figure 1-8 (a)), the concentration was almost 2 vol.% at 350 μm above the surface at the beginning and decreased to initial concentration at 500 μm above the surface. As the filtration time increased, the concentration at 350 μm above the surface increased and the recovery to the initial concentration happened at further distances from the membrane surface. It concluded that the thickness of concentrated layer increased with increasing filtration times. It was seen that this layer thickness was same for 99 min. and 116 min. filtrations, which was 800 μm above the surface. However, the concentration at 350 μm above the surface was significantly higher when the filtration time was 116 min. Stabilization of permeate flux with respect to time can be seen in Figure 1-8 (c). 2D-SAXS patterns (Figure 1-8 (b)) revealed that the anisotropy increased with decreasing distance from the membrane surface and with increasing filtration times (Rey et al., 2019).

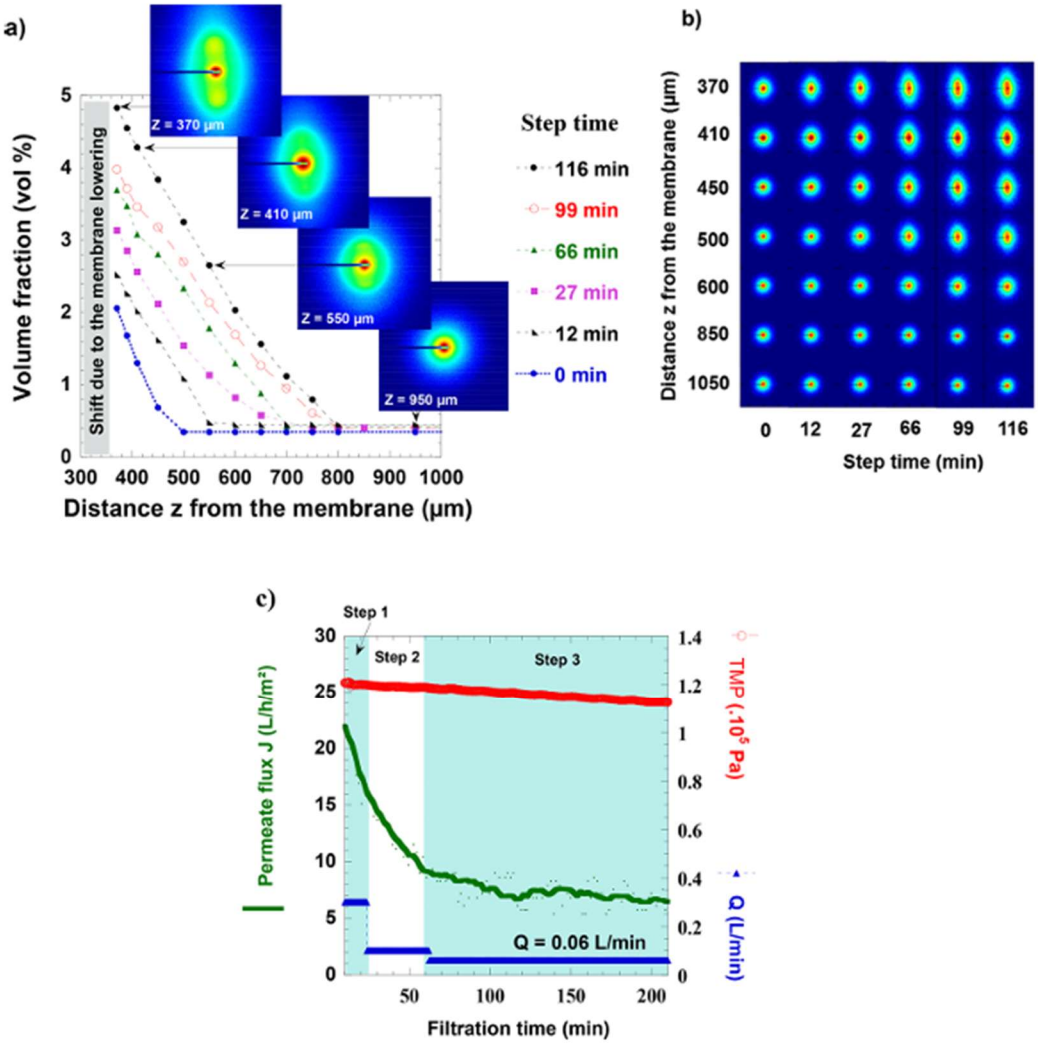

Figure 1-8. Results for crossflow ultrafiltration of 0.7 wt.% CNC suspension at 1.1 bar: (a) concentration profile (b) SAXS pattern (c) permeate flux (Rey et al., 2019)

Additionally, shear rate and shear stress profiles in the accumulated concentrated layers were generated in that study and they were provided in Figure 1-9. These shear rate profiles were calculated from the velocity field measured by micro-PIV. As seen in Figure 1-9 (a), there were two distinct behaviors in the shear rates: regions B and C. In region B, the flow started in the concentrated layer as deducted from the increase in the shear rate. Furthermore, this resulted in decrease in the volume fraction. In the beginning of region C, there was no concentrated layer that impacted the flow and the shear rate decreased along the distance from the membrane surface. For longer filtrations, there existed a third region, region A, as seen in Figure 1-9 (b) and (c). In this region, both shear stress and shear rate had values of zero which implies the

presence of a thick concentrated layer where no flow occurs. It was noted that the volume fraction reached 3.75 vol. % and 4.8 vol % at 66 min. and 116 min., respectively. Moreover, it was noted that the rheological behavior changed from Newtonian to shear-thinning at these corresponding volume fractions (Rey et al., 2019). This study highlighted the formation of gel layer and gave important information about the presence of concentration polarization layer, its thickness and impacts on the concentration and velocity profile during the crossflow filtration of CNC suspension.

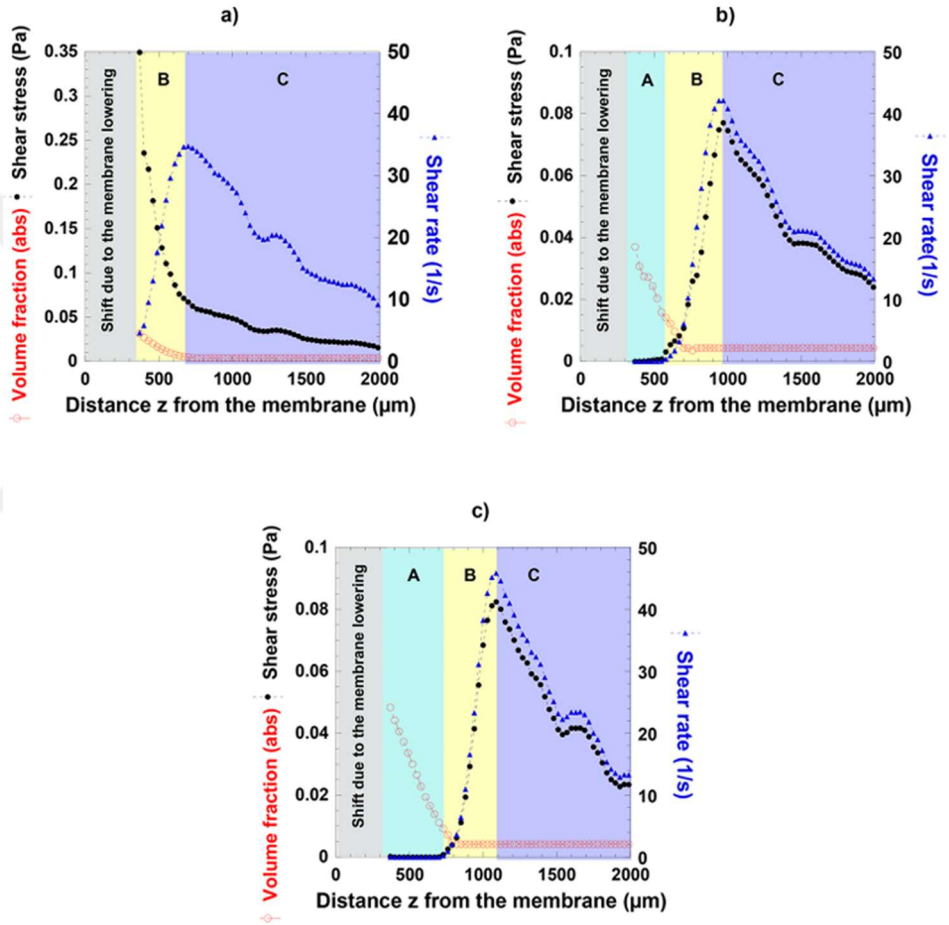

Figure 1-9. Results for crossflow ultrafiltration of 0.7 wt.% CNC suspension at 1.1 bar: (a) t=27 min. (b) t=66 min. (c) t=116 min. (Rey et al., 2019)

It was aimed to characterize the structural organization of CNCs during ultrafiltration and relaxation in one of the recent studies by using *in situ* small angle X-ray and light scattering analysis (Mandin et al., 2024). To see the effect of initial CNC concentration, 6 wt% that is in the biphasic region and 2 wt% that is in the isotropic

region CNC suspensions were filtrated with a transmembrane pressure of 1.2×10^5 Pa for 270 min and 220 h, respectively. (Mandin et al., 2024). As seen in Figure 1-10, CNC concentration increases while the pitch size decreases as time increases. Additionally, concentration decreases along the distance from the membrane surface. Inversely, cholesteric pitch increases as moving away from the membrane. During the relaxation, it is seen that both concentration and pitch size profiles were shifted. The gradient started to diminish, and concentration became more homogeneous. 2D scattering patterns show that cholesteric structures were preserved and they moved upwards along the z-direction without going through a remarkable change in their orientation and structures.

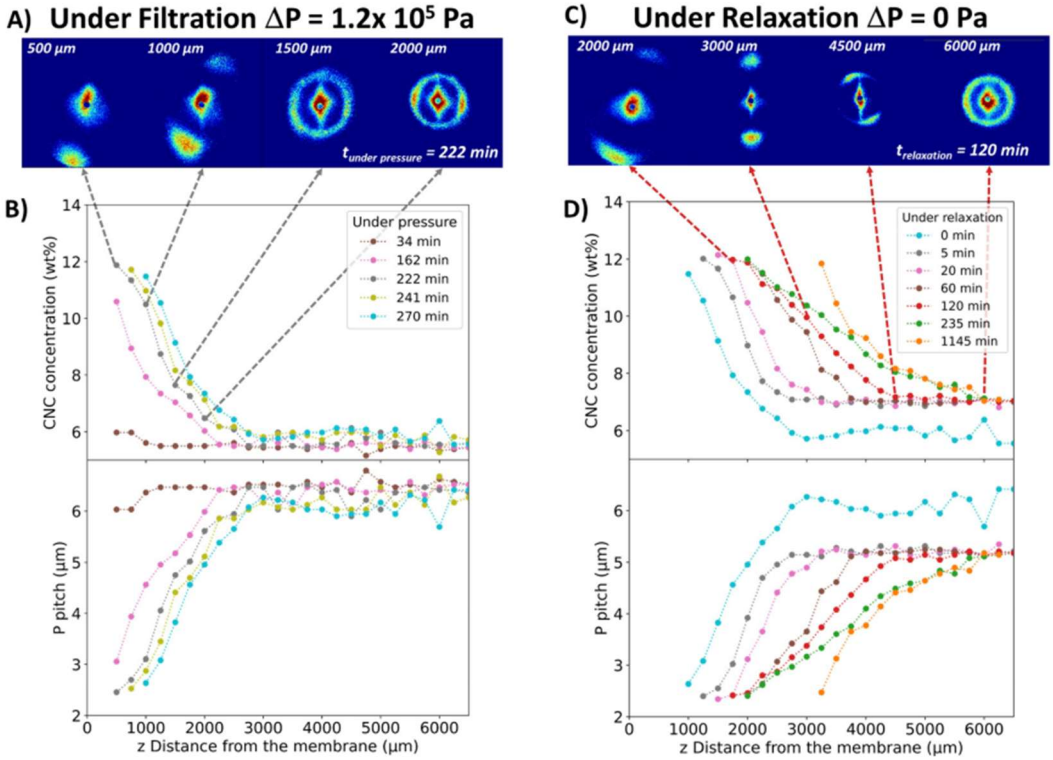

Figure 1-10. Characterization of chiral self-assembly of 6 wt% CNC suspension during filtration and relaxation. A) 2D SALS result obtained during the filtration. B) Concentration and pitch size distribution with respect to distance in z-direction and filtration time. C) 2D SALS result obtained during the relaxation. D) Concentration and pitch size distribution with respect to distance in z-direction and relaxation time. (Mandin et al., 2024a).

As seen in Figure 1-11, filtration of initially isotropic CNC suspension (2 wt%) also results in a concentration gradient along z-direction as in the filtration of 6 wt% CNC suspension. The concentration of the deposit layers increases over time. However, this increase is slower than the increase in the filtration of more concentrated suspension. The pitch of cholesteric structure decreased as time passed, and layer became more concentrated. It was seen that CNCs oriented more vertically in this dilute case when the 2D SALS (Small Angle Light Scattering) patterns of the two cases were observed.

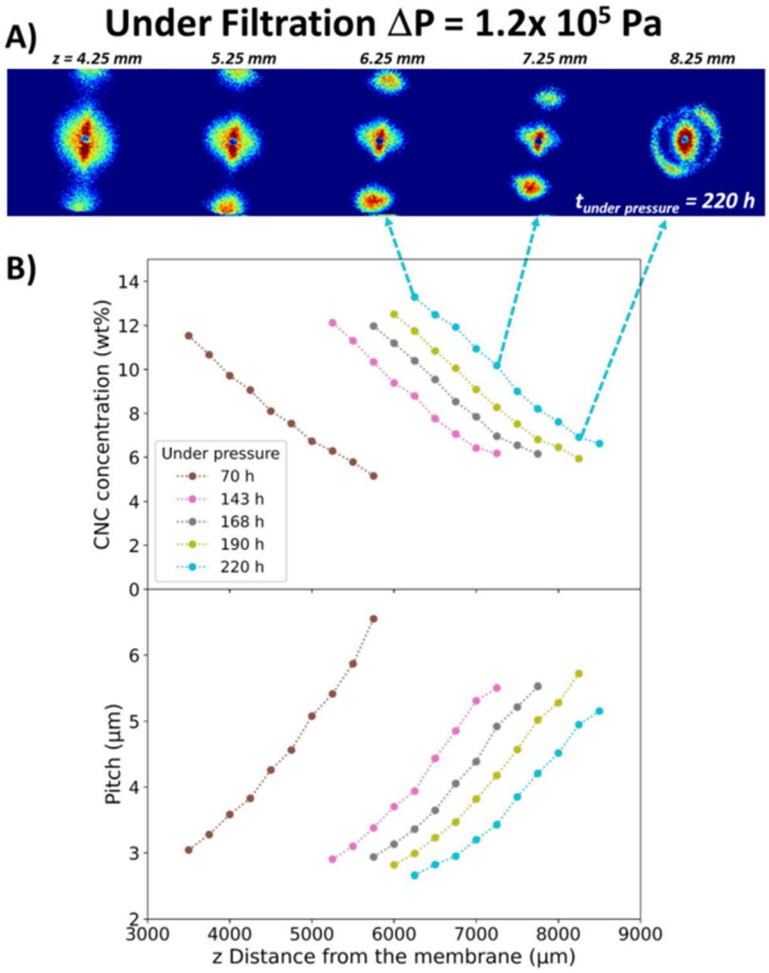

Figure 1-11. Characterization of chiral self-assembly of 2 wt% CNC suspension during filtration. A) 2D SALS result obtained during the filtration. B) Concentration and pitch size distribution with respect to distance in z-direction and filtration time. (Mandin et al., 2024)

The relaxation of the cake layer prepared with 2 wt% CNC suspension also showed similar behaviors with the concentrated one: the concentration gradient was lost, and the concentration became homogenous around a point (Mandin et al., 2024).

1.6 Alignment of CNCs and Control of the Alignment

Since the optical appearance of CNC deposits are highly dependent on the alignment of CNCs, it is one of the most important points to control and manipulate this alignment for many applications, for instance in sensor applications. Thus, this section explains some of the proven methods for controlling CNC alignment.

One of the most used methods for controlling the alignment is inducing hydrodynamic shear to CNC suspensions. Applying low shear rates induces only partial alignment (Geng et al., 2024; P. X. Wang et al., 2016). However, at higher shear rates, nanorods align parallel to the shear direction (T. Ebeling et al., 1999). It was also seen that high shear applied to cholesteric CNCs results in the disruption of helical structure and yield in nematic alignment (Hongladarom & Burghardt, 1993). The presence of nematic alignment can be checked via POM. Under POM, nematically aligned CNCs show strong birefringence, which is the phenomenon that explains the splitting of light wave into ordinary and extraordinary light due to anisotropy (Juárez-Rivera et al., 2021; Wang et al., 2025). Cholesteric liquid crystals can also show birefringence but there is a remarkable difference in optical behaviors of nematic and cholesteric liquid crystals: cholesteric ones particularly show Bragg reflection at specific wavelengths while the nematic ones show no wavelength-selective reflection (Mitov, 2012).

Recent studies showed that it is possible to provide quantitative control on CNC alignment even in confined spaces by utilizing the microfluidics system. Solution based shear is used to create thin film of nematically aligned CNC in a sub-millimeter tall channel by forcing CNC suspension to flow through that channel with a high flowrate (Jinkins et al., 2021).

Furthermore, studies showed that alignment of CNCs can be achieved and controlled by using spin coating (Cranston & Gray, 2008) or blade coating (Hoeger et al., 2011) methods. Other than applying shear, creating electric or magnetic field can be useful to achieve CNC alignment and to have control on that (Tatsumi et al., 2014).

Alignment of CNCs can be utilized in membrane separation processes. It is reported that the dead-end filtration of CNCs was utilized as a membrane preparation method

in the literature (Volkan, 2020). In a previous study, aqueous CNC layers deposited with the crossflow filtration are used as the selective layer of ultrafiltration membrane (Kocaman et al., 2021). For the tuning of CNC layers' morphology, surface shear rates are chosen as parameters. The CNC deposition is completed at a crossflow cell by utilizing the tangential flow as seen in Figure 1-12. For the CNC layers' stabilization, $AlCl_3$ is permeated in a dead-end-cell after the CNC deposition step. As a result of this study, it is concluded that the nematic alignment in CNC layer is increased with increasing surface shear rates applied and cholesteric structure in CNC layer was observed at the lowest surface shear rate (Kocaman et al., 2021). Additionally, the Blue Dextran and β-lactoglobulin probes rejections are increased as the shear rates and therefore the CNC layer alignment increase. It was also shown that membranes prepared with higher surface shear rates had higher permeances and specific layer resistances after the salt permeation. Thus, it can be concluded that higher nematic alignment in CNC layer resulted in membranes with higher permeance and more compact structure (Kocaman et al., 2021). This study implies that the CNC layers can be utilized as the selective layers for ultrafiltration membranes and the rejection performances can be adjusted by tuning the CNC morphology with applied surface shear rates.

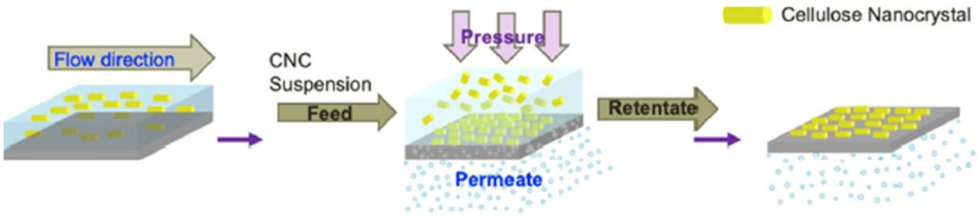

Figure 1-12. The schematic summary of fabrication of ultrafiltration membranes with CNC as the selective layers. This method utilizes the shear-alignment of CNC layers as the tuning parameter (Kocaman et al., 2021).

Previous experimental studies showed that the aggregation kinetics of CNCs are in good agreement with the estimations done with classical DLVO (Derjaguin–Landau–Verwey–Overbeek) theory. In terms of colloidal stability, it was seen that trivalent salts like $AlCl_3$ were more effective in the destabilization of CNC suspensions (Cao & Elimelech, 2021). It is also known that the increase in the ionic strength of CNC suspensions results in decrease in Debye length and thickness of the electrical double

layer. Furthermore, CNC nanorods become closer to each other and the effective aspect ratio become higher as a result of this increase in the ionic strength of CNC suspensions (Kádár et al., 2021). It was shown that regulation of electrostatic repulsions of CNCs with addition of NaCl resulted in decrease in Debye length in the suspension and decrease in cholesteric pitch size of dried CNC film (Kong et al., 2024). In one of the previous studies of our group, it was shown that ionic strength and pH of the CNC suspension can be other tuning parameters of CNC membranes' permeance and rejection performance. $CaCl_2$ and $AlCl_3$ salts were not suitable for filtration to prepare CNC membranes since they induced extensive aggregation in the suspension. Conversely, NaCl salt with a concentration range of 0 mM - 50mM was compatible for filtration since the CNC suspensions with NaCl was still stable during the deposition (Kocaman et al., 2022). Thus, it is decided to utilize sodium chloride salt in this study to increase the ionic strength of the feed solution by decreasing the electrostatic repulsions between the TEMPO (2,2,6,6-Tetramethylpiperidin-1-yl)oxyl)-oxidized CNCs (TEMPO-CNCs) . The previous study also shows that increase in ionic strength and pH of the CNC suspensions results in more compact membrane structure, regardless of the applied shear stress and final CNC ordering (Kocaman et al., 2022).

A previous study shows that chemical crosslinking with $AgNO_3$ and $K_2S_2O_8$ can be utilized for the stabilization of CNCs instead of $AlCl_3$ permeation (İçten, 2023). In order to achieve this crosslinking, a surface modification on CNCs should be done first. Hence, CNCs synthesized by the sulfuric acid hydrolysis are modified with TEMPO-mediated oxidation. During this modification, it is possible to introduce carboxylate groups (–COO−) at CNCs' surface as seen in Figure 1-13 (Le Gars et al., 2020).

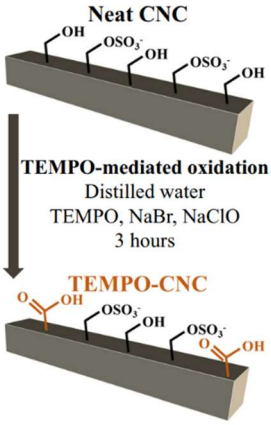

Figure 1-13. The surface modification of CNC via 2,2,6,6-tetramethyl-1-piperidinyloxy (TEMPO)-mediated oxidation process (Le Gars et al., 2020)

After the TEMPO-oxidation, CNCs are filtrated in a crossflow module with a crossflow rate of 62 mL/min and deposition of TEMPO-CNC onto porous support is achieved. To achieve more stabilization, it is decided to add salt inside the TEMPO-CNC suspensions just before the deposition to achieve concentration of 100 mM NaCl. SEM and POM images of the dried membrane samples show that cholesteric self-assembly of TEMPO-CNCs has occurred. Additionally, this study indicates that a remarkable rejection performance for long term can be achieved by utilizing the cake layer prepared with crossflow filtration of TEMPO-CNC suspensions having 100 mM salt content and stabilization with chemical crosslinking with 0.08 wt. % $K_2S_2O_8$ and 0.36 wt. % $AgNO_3$ for 2 hours (İçten et al., 2024).

This study aims to investigate TEMPO-CNC deposition and cake layer formation with crossflow filtration. This investigation focuses on the impacts of TEMPO-CNC deposition duration and TEMPO-CNC and NaCl concentration on the structure of deposit layers. To observe these effects, different TEMPO-CNC suspensions having different salt and TEMPO-CNC concentrations were filtrated onto porous support membrane with constant crossflow rate and transmembrane pressure but for various durations. The deposit layers were characterized by POM, SEM, flow resistance calculation, and TGA to measure solid content. The structural and morphological properties of the TEMPO-CNC cake layers were tried to be understood in this study.

CHAPTER 2

EXPERIMENTAL PROCEDURES

2.1 Materials

Dimethyl sulfoxide (DMSO, 99.0%) , Ethanol (99%) were purchased from *Isolab*; Cellulose (cotton linter, medium), Cellulose acetate (CA, Average molecular weight 50000), Sulfuric acid (95-97%), Sodium hydroxide, Sodium Bromide (NaBr, 99.99% trace metal basis), 2,2,6,6-tetramethyl-1-piperidinyloxy (TEMPO, 99%) were purchased from *Sigma-Aldrich*; Sodium chloride (99%), Hydrochloric acid (Fuming, 37%) were purchased from *Merck*; Aluminum chloride hexahydrate (99%) was purchased from *Tekkim*; Sodium hypochlorite from *Aromel.*

Pure water having a conductivity of 18.2 MΩ.cm was used in preparation of the solutions, membrane performance tests, washing and wetting of the samples and dialysis.

2.2 Support Membrane Preparation

CA was dried overnight in vacuum oven before the membrane solution preparation. 10 wt.% CA and 90 wt.% DMSO were mixed with a magnetic stirrer and a roller mixer until the casting solution became homogeneous. Then, the solution was left still for 1 or 2 days to remove the air bubbles formed during the mixing process.

Flat sheet support membranes were prepared by using the casting solution and 250 µm casting bar. The membrane solution was cast on a glass plate at room conditions. The cast polymer layer was immersed in a reverse osmosis water bath for phase separation. Then, cast support membrane was put in reverse osmosis water a couple of times to wash the remaining solvent completely. The washed support membrane was stored inside vol.20% ethanol solution to prevent microorganisms' growth. These steps for support membrane fabrication are schematically shown in Figure 2-1.

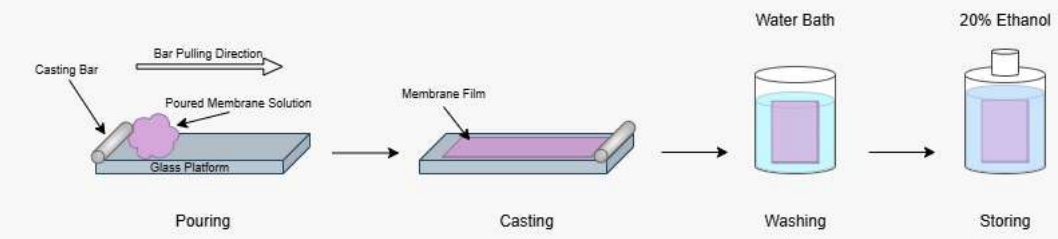

Figure 2-1. Schematic representation of support membrane fabrication steps

2.3 Preparation of TEMPO-CNC Suspensions

2.3.1 Synthesis of CNC

Prior to CNC preparation, cellulose was dried overnight at 80 °C and stored in a vacuum oven. 150 ml of sulfuric acid (96 %) was added to 80 ml of pure water in a beaker. Then, the mixture was heated in a water bath until its temperature reached 45 °C. In another beaker, 28.8 g of dried cellulose was hydrated with 58 ml of pure water. After the addition of hydrated cellulose, the final acid concentration has become 50%. Then, the sulfuric acid solution was added and rigorously mixed with hydrated cellulose. The final solution was placed in a water bath for 30 minutes for the reaction to proceed until it was quenched with chilled pure water by diluting to 1 L. The remaining sulfuric acid and produced salts were removed from the CNC suspension by first decanting and discarding the clear portion until there was no phase separation. Then, the remaining part was dialyzed against pure water until its conductivity matched that of pure water. The acid hydrolysis of cotton linter, quenching with cold ultrapure water and dialysis steps were schematically shown in Figure 2-2.

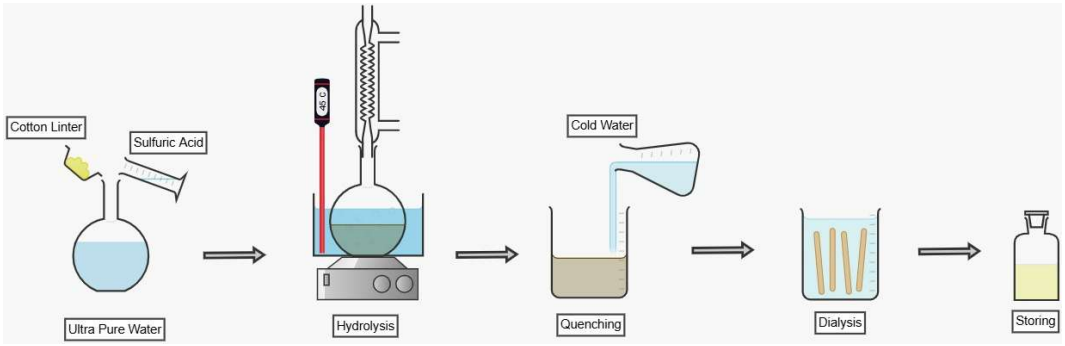

Figure 2-2. The schematic representation of CNC synthesis steps

2.3.2 TEMPO-Oxidation of CNC

CNC solutions that were previously prepared were further modified by TEMPO oxidation. Into 1 g oven dried CNC basis suspension, 0.0295 g TEMPO, 0.324 g NaBr, and 6 g of 12% NaClO equivalent were added, and left to react for 3 hours. During this operation, pH of the solution was kept in the 10-10.5 range by adjusting with NaOH solution. The reaction was quenched by adding 3.7 ml ethanol to form chloroform with unreacted NaClO. Then, pH of the suspension was adjusted to 1.5 to convert deprotonated CNCs to protonated form for both carboxyl and sulphate half ester groups. Finally, the suspension is dialyzed against pure water until its conductivity matches that of pure water.

2.3.3 Crossflow Filtration of TEMPO-CNCs

TEMPO-CNC films were fabricated by crossflow filtration of TEMPO-CNC crystals on the support membrane surface. To illustrate, 0.15 wt. % TEMPO CNC without salt was prepared and sonicated for 20 minutes using a Bandelin SonoPlus mini with MS 2.5 probe at 100 % amplitude, followed by filtration of the suspension through a support membrane under a crossflow configuration where crossflow flow rate was set to 64 mL/min by measuring the retentate flow rate. Filtration continued until the limiting flux reached at the constant pressure of 1 bar. For the longer depositions, the duration was kept around three hours. For the preparation of some TEMPO-CNC cake layer samples, shorter depositions were done. During the filtrations, flux was measured

by collecting the data of permeate flowrate regularly. To do this, permeate was collected with a graduated cylinder. Crossflow filtration of TEMPO-CNC suspensions is schematically summarized in Figure 2-3.

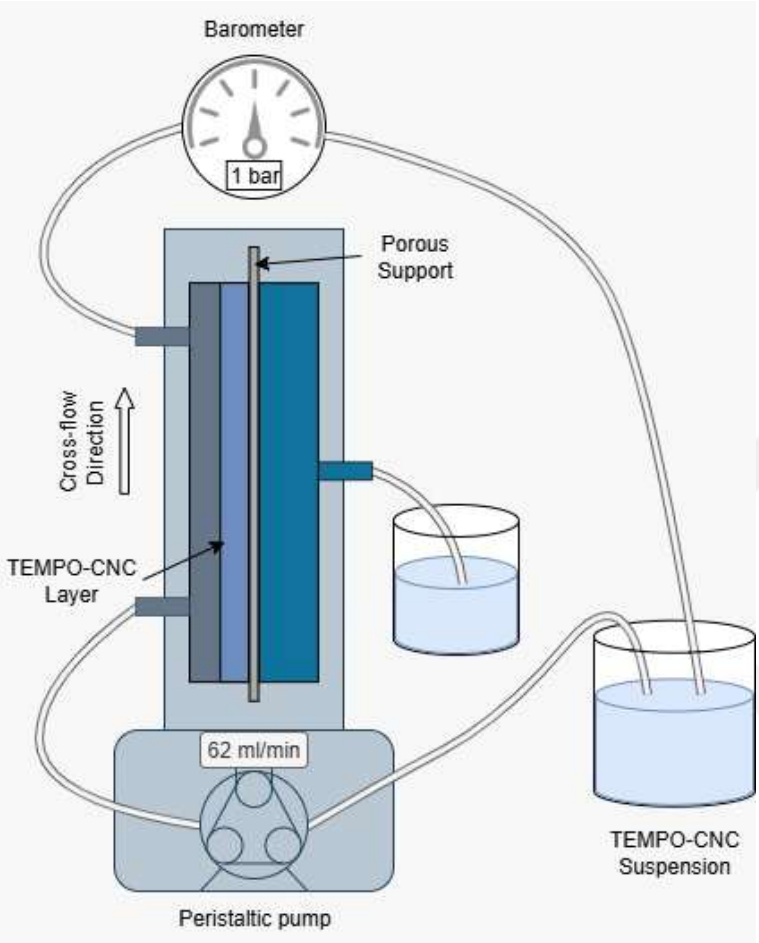

Figure 2-3. The schematic representation of crossflow filtration of TEMPO-CNC

2.3.4 $AlCl_3$ Treatment of TEMPO-CNC Deposit Layer

After TEMPO-CNC deposition , a 200 mM aqueous $AlCl_3$ solution was permeated through the deposit layers in dead-end mode to induce irreversible coagulation of TEMPO-CNCs on the support membrane surface. Lastly, excess $AlCl_3$ within the deposit layer was washed out by pure water permeation in dead-end mode, and pure water permeance values of TEMPO-CNC-deposited films were measured. TEMPO-CNC deposit layer resistances of fabricated films were then predicted using Darcys

law and resistances in series model after the TEMPO-CNC deposition and after the physical stabilization of deposits with $AlCl_3$ permeation.

2.3.5 Rheological Analysis

Rheological properties were analyzed using an Anton Paar MCR 320 rheometer with an Anton Paar CP50-2 cone and plate geometry with a cone angle of 2.008° and 0.21 mm spacing at minimum at 25 ºC. After achieving target concentrations, samples were sonicated for 20 minutes using a Bandelin SonoPlus mini20 with an MS 2.5 probe with 100 % amplitude. Steady shear viscosities of various suspensions were measured at a shear rate range of 0.01 - 100 s^{-1}.

2.3.6 Thermogravimetric Analysis

A Shimadzu DTG-60H Thermogravimetric analyzer was used for the thermal gravimetric analysis for wet and dry TEMPO CNC deposit layers. Analyzed TEMPO-CNC layers were first prepared with the previously mentioned membrane preparation method. The films were dried overnight at room temperature and open to the atmosphere. After complete drying, it was put in pure water and kept overnight for complete wetting of the previously dried gel layer. Lastly, the sample was cautiously taken from the pure water, and excess water is removed with a tissue before the analysis. The wet TEMPO-CNC samples were analyzed without further treatment. Approximately 50 mg of TEMPO-CNC gel layer was taken from the samples' support layers. Analyses were completed between approximately room temperature to 150 °C in an N_2 environment with a 10 °C/min heating rate. After all water content was removed from the sample, the stabilized masses of the samples were recorded, and solid contents of both dry and wet samples were calculated.

2.3.7 Membrane Performance Tests

Membrane performance tests were completed with Sterlitech CF042 crossflow filtration cell at 1 bar with a reported effective membrane area of 42 cm^2. The tests

lasted until a steady membrane flux was observed. Not only the pure water permeance of support but also the final permeance of the TEMPO-CNC deposited films were measured before and after the $AlCl_3$ treatment. These permeances were utilized to calculate resistances of the TEMPO-CNC cake layers. For these calculations, Darcys Law and resistances-in-series-model were used.

2.3.8 Polarized Optical Microscopy

An Olympus BX53M Microscope equipped with an analyzer and polarizer were used to obtain polarized optical microscopy images. Samples were prepared with the exact procedure mentioned in the membrane preparation steps. Both wet and dry samples were analyzed. The dry samples were observed under POM in reflection mode to see the color of deposit layers when they are completely dried.

For the wet samples, the observation under the POM was done in two different ways. In the first way, TEMPO-CNC deposit layers' images were directly taken with the support layer. For the second way, deposit layers were transferred on a glass microscope slide with caution. In that way, the reflection and transmission images of the deposit layers can be taken separately. Also, the images were taken from both the support membrane and the bulk flow side by placing another glass slide onto the transferred layer and changing the upper side. In the reflection mode, the crucial point is to observe the color appearance of the layer.

In the transmission mode, the transferred deposit layer sample was placed at 0, 45, 90, 135 and 180 degrees with respect to analyzer. Furthermore, the drying process was also visually investigated with POM in reflection mode to observe whether the color shift from red to blue is present. The POM images were analyzed by using ImageJ.

2.3.9 Scanning Electron Microscopy

Liquid nitrogen was used to freeze and fracture TEMPO-CNC deposit layer samples prior to 40 nm sputter coating with Cu coating with Leica EM ACE200. SEM micrographs of the coated samples were obtained with TESCAN-VEGA 3 electron

microscope with secondary electron mode with a working distance of 12 mm, 10 kV high voltage, and beam intensity of 8 or 10. ImageJ software was used for the analyses of micrographs.

CHAPTER 3

RESULTS AND DISCUSSIONS

In this study, crossflow filtration of TEMPO-CNC on a porous support was aimed to be observed. TEMPO-CNC filtration was investigated by the deposition of TEMPO-CNC suspensions with different concentrations. Investigation was done by observing the effect of NaCl content and filtration duration.

3.1 Preparation and Characterization of TEMPO-CNC Deposit Layer in Terms of Permeance and Resistance

TEMPO-CNC suspensions with different TEMPO-CNC concentration and NaCl content were deposited on the support membranes by the crossflow filtration with a transmembrane pressure of 1.0 bar. After deposition procedure was continued with permeating 0.2 M $AlCl_3$ solution through the layer and washing with pure water as a last step. As an example, the permeance and resistance plots of a sample prepared by the deposition of 0.075% TEMPO-CNC with 0 mM NaCl suspension were provided in Figure 3-1 and Figure 3-2. For the sake of better illustration, permeance data was normalized against the pure water permeance (PWP) of the support membrane that was measured before the TEMPO-CNC deposition as explained in 2.3.7. The time interval for experimental data collection was four minutes, and this is shown with error bars in Figure 3-1 and Figure 3-2.

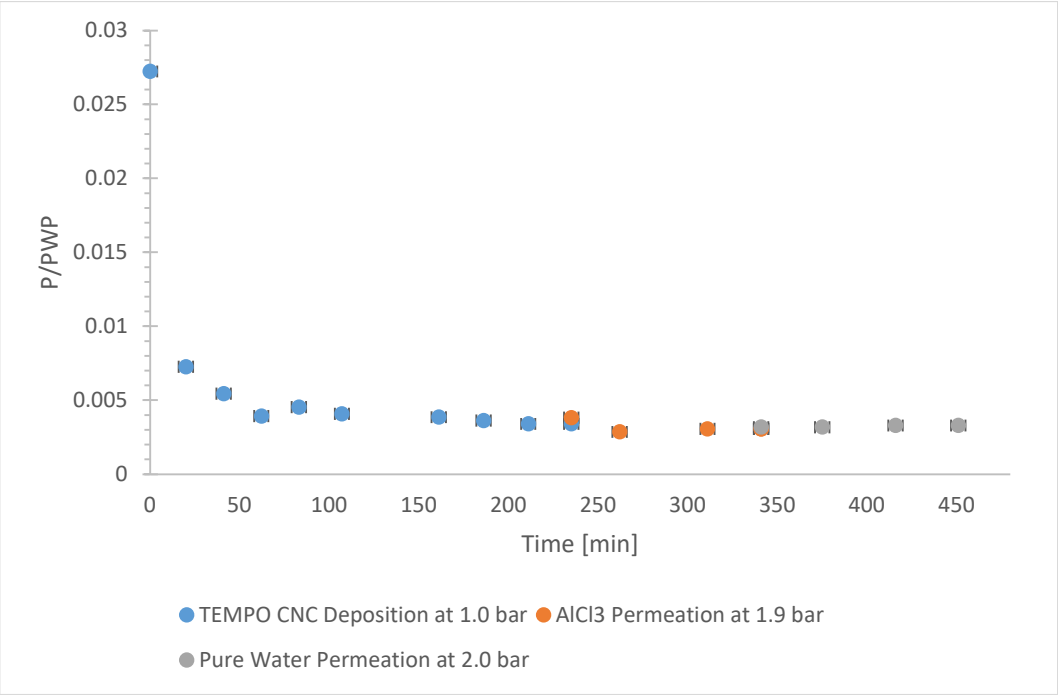

Figure 3-1. Permeance data with respect to time obtained during the fabrication of TEMPO-CNC deposit layer

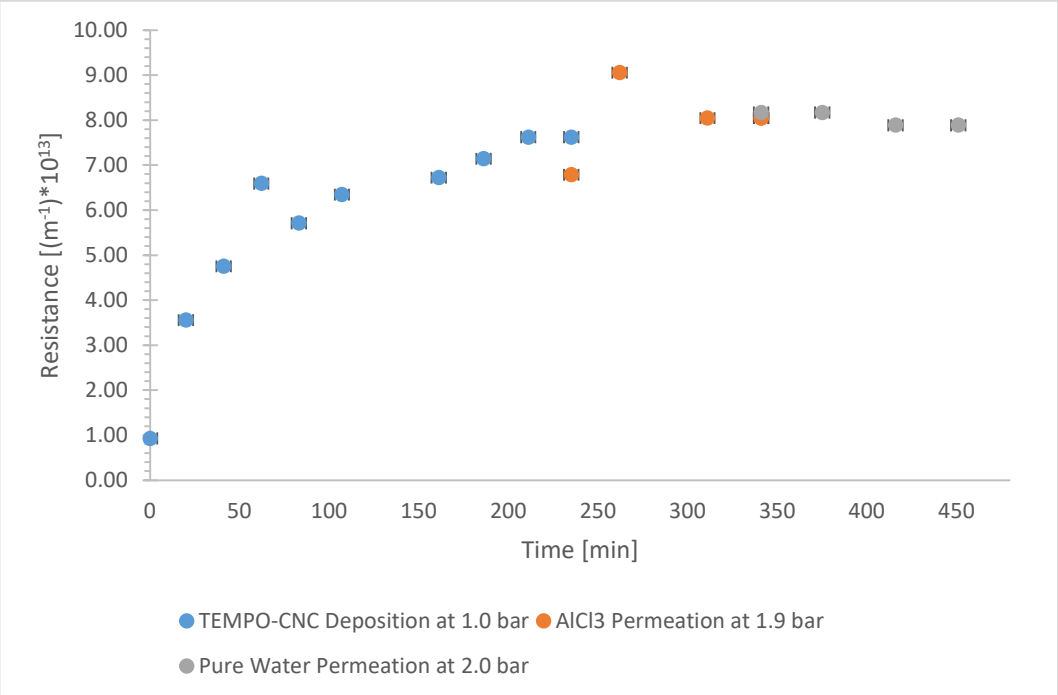

Figure 3-2. Resistance data with respect to time obtained during the fabrication of TEMPO-CNC deposit layer

As seen in Figure 3-1, the permeance started to decline instantly when the TEMPO-CNC filtration started. It completed its decline at the beginning of filtration, in approximately the first hour. As the filtration continued, permeance slightly decreased and became steady at around 16 LMH. While changing from TEMPO-CNC suspension to $AlCl_3$ solution, permeance started to decrease as seen from the first orange dot in Figure 3-1. As $AlCl_3$ permeation proceeded, permeance decreased to 11 LMH. The washing process of excess $AlCl_3$ did not change the permeance significantly and the final permeance was noted as approximately 13 LMH at the end.

The resistance of the layer increased sharply at the beginning of TEMPO-CNC filtration as seen in Figure 3-2. Then, it continued to increase mildly and became steady at around 2.5×10^{13} m^{-1}. At the beginning of $AlCl_3$ permeation, an instant jump in the resistance was observed. After that, the resistance became constant at around 3.5×10^{13} m^{-1}. As seen from the grey dots in Figure 3-2, the washing of excess $AlCl_3$ resulted in a slight decrease in the resistance and it became 3.0×10^{13} m^{-1} at the end of the TEMPO-CNC deposit layer fabrication process.

Note that these behaviors of TEMPO-CNC deposit layers' permeance and resistance are quite similar for all samples although their initial TEMPO-CNC concentration and salt content were different than this representative sample. It was seen that $AlCl_3$ and pure water permeations that follow the TEMPO-CNC deposition did not create a significant change in the permeance and resistance. However, the permeance and resistance of the cake layer highly depend on the suspension composition, and duration of TEMPO-CNC deposition.

3.2 Effect of TEMPO-CNC Deposition Duration

As mentioned previously, permeance and resistance of the deposit layers in all samples showed a dependency on the duration of TEMPO-CNC filtration. In order to investigate this dependency in more detail, numerous samples were prepared with 0.30% TEMPO-CNC and 5 mM salt and the data collected with respect to time is analyzed. The TEMPO-CNC deposition times were selected as 10, 30, 60, 90, and 180 minutes.

3.2.1 Effect of Deposition Time on Permeate Flux and TEMPO-CNC Layer Resistance

As seen in Figure 3-3, the permeate flux tends to decrease for longer deposition times, with a higher decrease rate at first which then continued with a slower decrease rate. It is noted that the permeate fluxes were in quite good agreement for all samples. Two of the repeated samples, the ones with the longest deposition times, were only included in these plots for the sake of simplicity. One should note that the average limiting flux for these samples are 7.9±0.9 LMH. One important result that can be deduced from Figure 3-3 is that the rate of decrease in the fluxes is different at the beginning and at the of the filtrations. At first, the permeate fluxes sharply decline due to the sudden deposition of the first TEMPO-CNCs. Then, this decrease rate becomes slower as the deposition proceeds. It can be said that permeate flux profile with respect to time has two distinct parts: one with the higher decreasing rate and other with significantly lower decreasing rate.

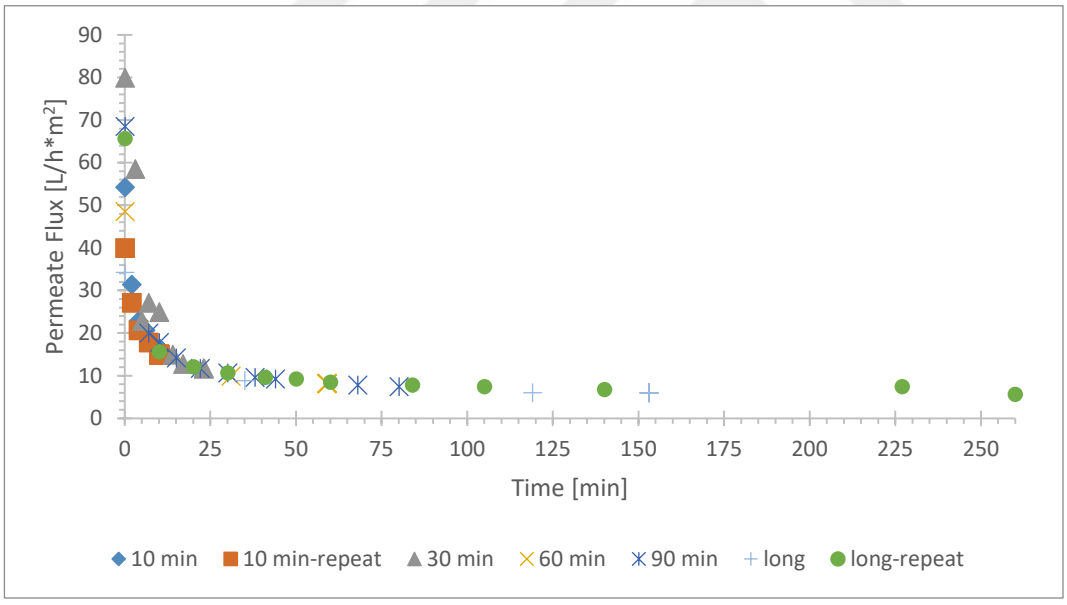

Figure 3-3. Permeate flux vs deposition time of the samples prepared with 0.30% TEMPO-CNC and 5 mM NaCl

Similar to the limiting flux, TEMPO-CNC layer resistances were consistent for the samples. The sample with the longer deposition time has the highest resistance as seen in Figure 3-4. As deposition time increases, the permeate flux decreases while the

resistance increases. Again, resistance values for two representative samples were included in the plot for simplicity. The average resistance for the samples prepared with the longest deposition time is $(7.1\pm1.5)\times10^{13}$ m^{-1}.

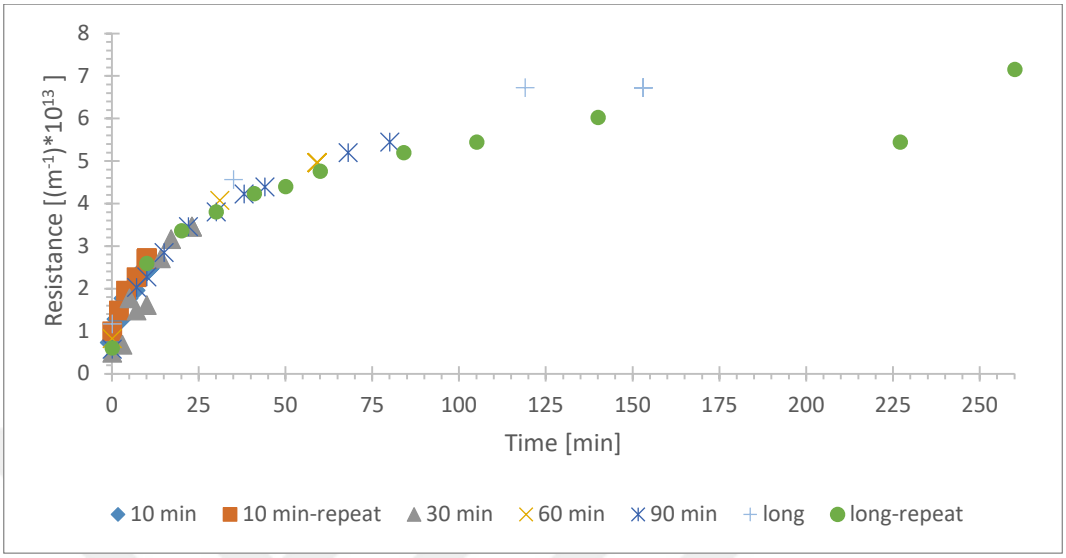

Figure 3-4. TEMPO-CNC layer resistance vs deposition time of the samples prepared with 0.30% TEMPO-CNC and 5 mM NaCl

Cake layer thicknesses of the samples with different deposition durations were plotted as seen in Figure 3-5 (a). These thicknesses were measured from the cross-section SEM images of the dried cakes, and these images can be seen Figure 3-6. The cake layer thickness of the samples did not significantly increase as seen in Figure 3-5 (a). Similar observation was made when the specific resistances of the deposit layers were calculated and plotted with respect to time, as seen in Figure 3-5 (b). Specific resistance of the deposit layers did not show a significant change with respect to time. Even though the cake layer thickness and specific resistance did not change significantly with deposition time, the morphology of the deposits were different for various deposition durations as will be discussed later. The possible explanation of this difference might be the reorganization occurred in the deposits as deposition time increases.

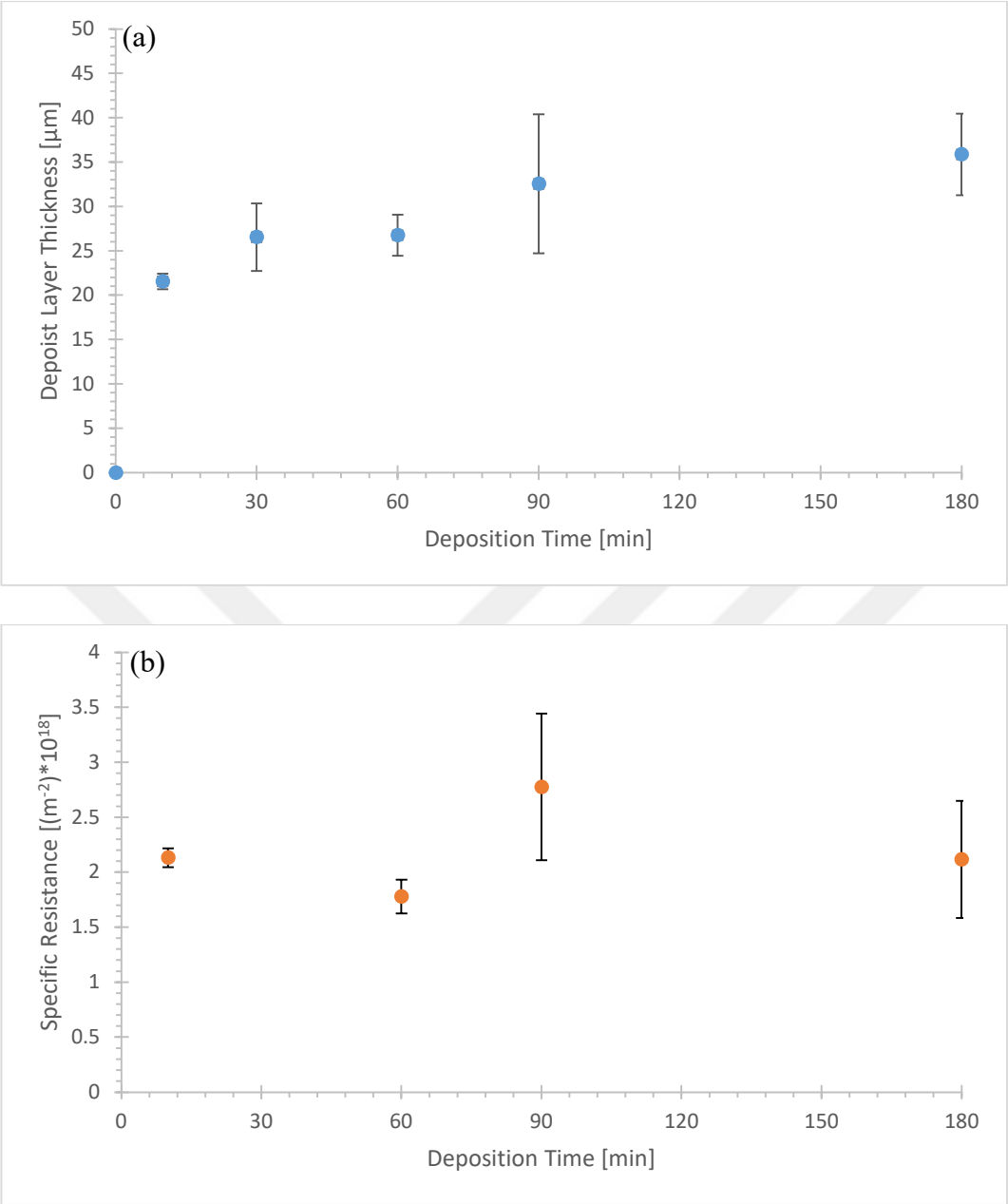

Figure 3-5. (a) Cake layer thicknesses, (b) Specific resistances of the samples prepared with different deposition durations of 0.30% TEMPO-CNC and 5 mM NaCl suspensions

Cross-section SEM images of the dried cake layers may provide useful information regarding the time-dependent phase formation of TEMPO-CNCs. These images for the samples prepared by various deposition durations were given in Figure 3-6.

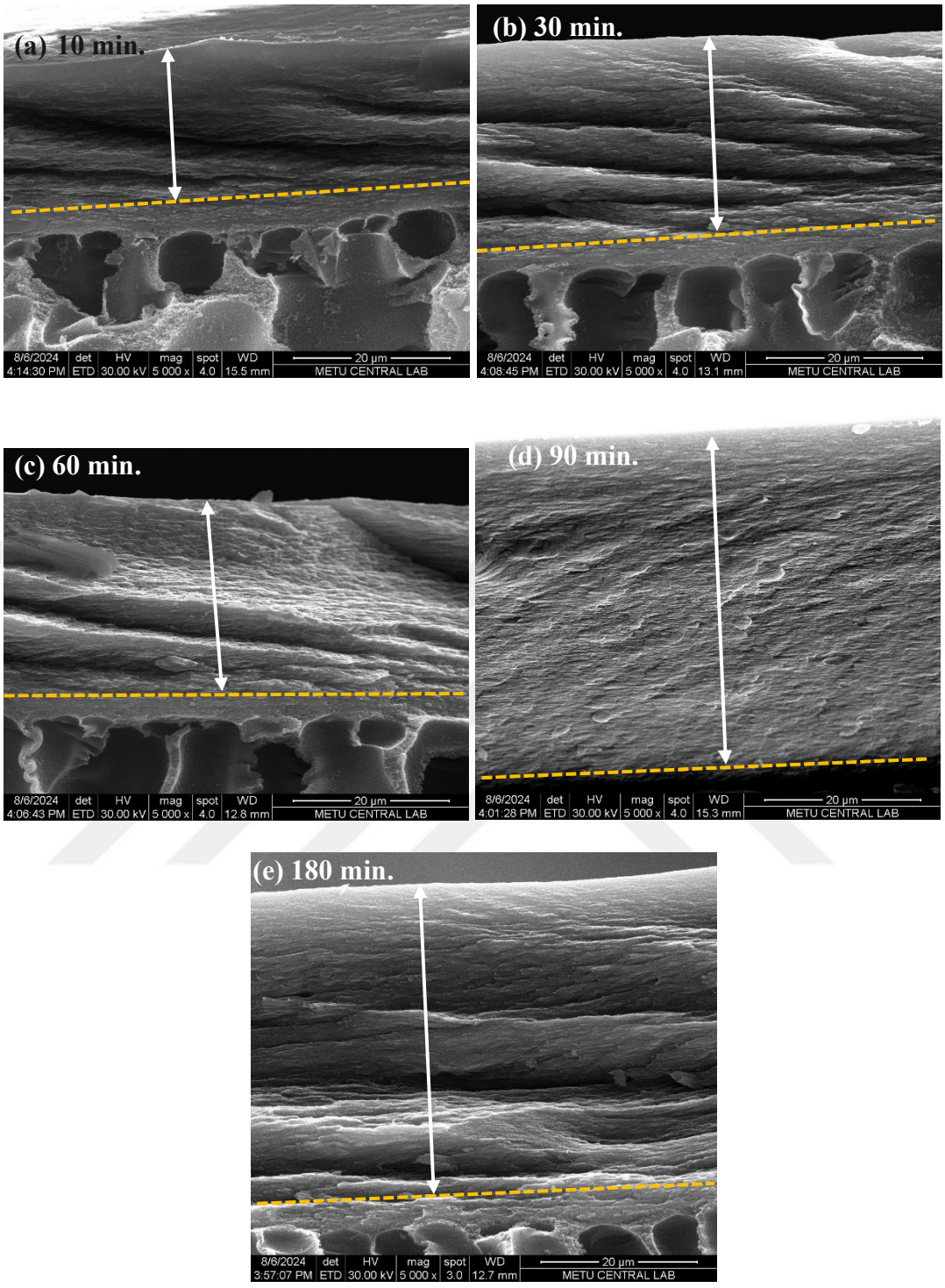

Figure 3-6. SEM images of the cross-sections of dried samples prepared by the deposition of 0.30% TEMPO-CNC, 5 mM NaCl for (a) 10 min. (b) 30 min. (c) 60 min. (d) 90 min. (e) 180 min. White arrows indicate the cross-section of TEMPO-CNC deposit layers. Yellow dashed lines represent the boundary between support and deposit layers. Scale bars indicate 20 µm.

As previously seen in Figure 3-5 (a), TEMPO-CNC deposit layer thickness of the sample with 180 minutes of deposition is larger than the thickness of the sample with 10 minutes of deposition. This thickness difference can be visually seen with the help of white arrows in Figure 3-6. The thicknesses were measured as 22.5±0.7 µm and 34.7±3.7 µm for the membranes with 10 minutes and 180 minutes of depositions, respectively. As stated before, the deposit layer thickness slightly increases as the duration of deposition increases and did not change significantly especially after 30 minutes of deposition.

For the comparison, magnified cross-section SEM images of the deposits prepared with shortest and longest depositions were given in Figure 3-7. As seen in Figure 3-7 (b), periodic and layered structure exist in the cross-section image of the deposit prepared with 180 minutes of deposition. This layered and periodic appearance is an indicator of cholesteric structure (Frka-Petesic et al., 2023; Geng et al., 2024b; Mandin et al., 2024b; Parker et al., 2018). However, the sample prepared by 10 minutes of deposition lacks this layered structure as visible in Figure 3-7 (a).

This different behavior might be also observable in the POM images of the wet samples. POM images of the samples prepared by the filtration of 0.30% TEMPO-CNC and 5 mM NaCl for various durations were given in Figure 3-8.

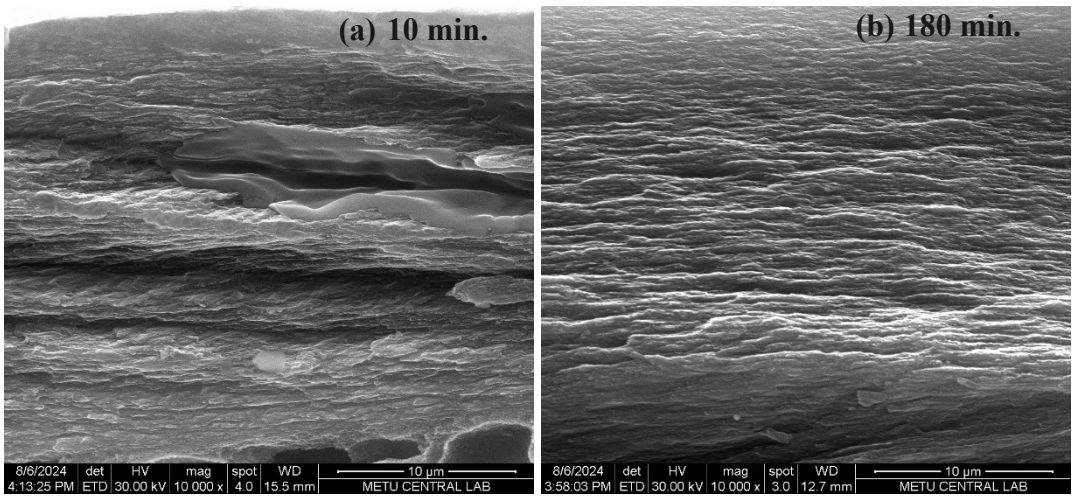

Figure 3-7. Magnified cross-section SEM images of the dried deposits prepared by the shortest and longest depositions of 0.30% TEMPO-CNC, 5 mM NaCl for (a) 10 min. (b) 180 min. Scale bars: 10 µm for both images.

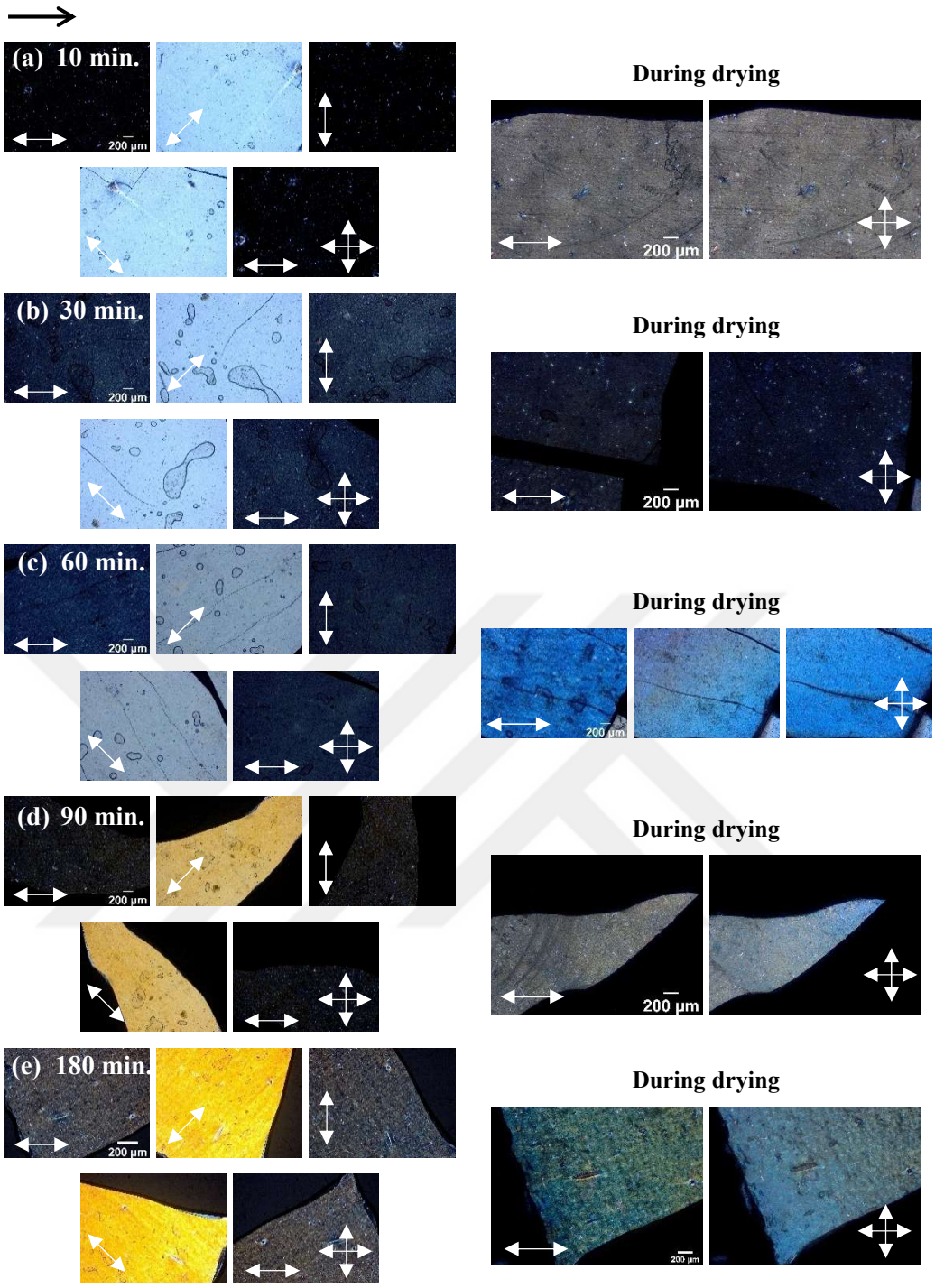

Figure 3-8. POM images of samples with 0.30% TEMPO-CNC, 5 mM NaCl: Transmission images of wet samples (left). Reflection images of the samples during drying (right). Deposition times: (a) 10 min, (b) 30 min, (c) 60 min, (d) 90 min, (e) 180 min. Black arrow shows the direction of flow during the deposition. Single white arrow shows the sample position according to the analyzer. Cross white arrows show the direction of analyzer and polarizer. Scale bars: 200 µm for all images.

Samples prepared with the deposition of 0.30% TEMPO-CNC, 5 mM NaCl for180 minutes, 90 minutes, 60 minutes, 30 minutes and 10 minutes were analyzed under the POM to determine the dominant liquid crystal phase. When wet samples were placed so that the feed flow direction during the deposition is 45° with the polarizer, brighter appearance was observed for all five samples in the transmission mode. Thus, it can be said that all samples showed birefringence to some extent which indicates the presence of nematic alignment of TEMPO-CNCs. The intensity of this bright appearance is the same at 10 and 30 minutes, which decreases as the deposition time increases from 60 minutes to 180 minutes as can be seen from Figure 3-8 (c) to Figure 3-8 (e).

As seen in Figure 3-8 (a) and (b), there were strong birefringence in the transmission images and no blue color shift in the reflection images of the drying samples. Therefore, TEMPO-CNCs were aligned nematically at the depositions of 10 minutes and 30 minutes. However, when the deposition time was increased to 1 hour, a slight blue color shift, as seen in the right image of Figure 3-8 (c), was observed in the reflection mode of drying sample. Thus, it is possible to conclude that chiral nematic structure was present in this one. Similarly, the blue color shift was seen in the right image of Figure 3-8 (d) during the drying of the sample with 90 minutes deposition. The blue color shift was even more obvious at sample prepared with 180 min deposition in the right image of Figure 3-8 (e), indicating a dominant cholesteric behavior in the sample.

To observe the role of duration of the applied shear during the deposition instead of the deposition time of TEMPO-CNC itself, another experiment was performed. TEMPO-CNC (0.30%) with 5 mM NaCl was fed to system for the first half an hour of the deposition. Then, for the remaining 2.5 hours, the feed was switched to a solution that has the same NaCl concentration and pH, but no TEMPO-CNC. This TEMPO-CNC-free solution was obtained by the dead-end filtration of original TEMPO-CNC suspension (0.30%, 5 mM NaCl) with a commercial membrane. With the help of this dead-end filtration, all TEMPO-CNCs were retained on the membrane and formed a gel layer while the permeate only consists of NaCl at the same pH. In this way, the same shear was applied for the whole 3 hours of deposition but, TEMPO-CNC

deposition took place only during the first 30 minutes. Hence, the individual and isolated contribution of shear, independent of TEMPO-CNC deposition, could be investigated.

The limiting flux and the resistance values of the sample prepared without TEMPO-CNC were much more different than the samples with TEMPO-CNC. The limiting flux and the TEMPO-CNC layer resistance of the samples without TEMPO-CNC are 9.3±0.5 LMH and (4.6±0.4) $\times 10^{13}$ m^{-1}, respectively. The limiting flux is much higher, and the resistance is much lower than the samples prepared with TEMPO-CNC. This comparison can be seen in Figure 3-9 and Figure 3-10.

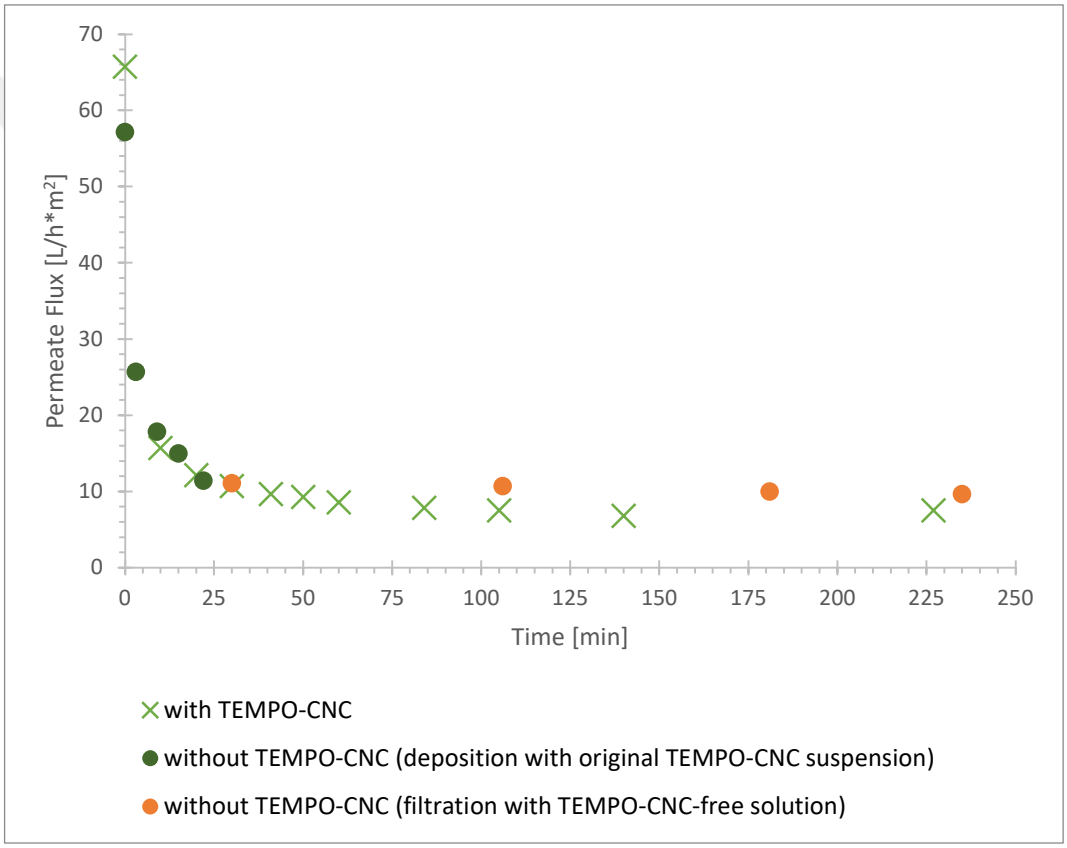

Figure 3-9. The comparison of permeate flux of the samples prepared with and without 0.30% TEMPO-CNC with 5 mM NaCl

As seen in Figure 3-9, the permeate fluxes of the two samples were quite similar for the first thirty minutes. After that point, the permeate flux of the sample with TEMPO-CNC continued to decrease to approximately 5 LMH. On the contrary, the permeate flux of the sample without TEMPO-CNC stayed almost constant at around 10 LMH.

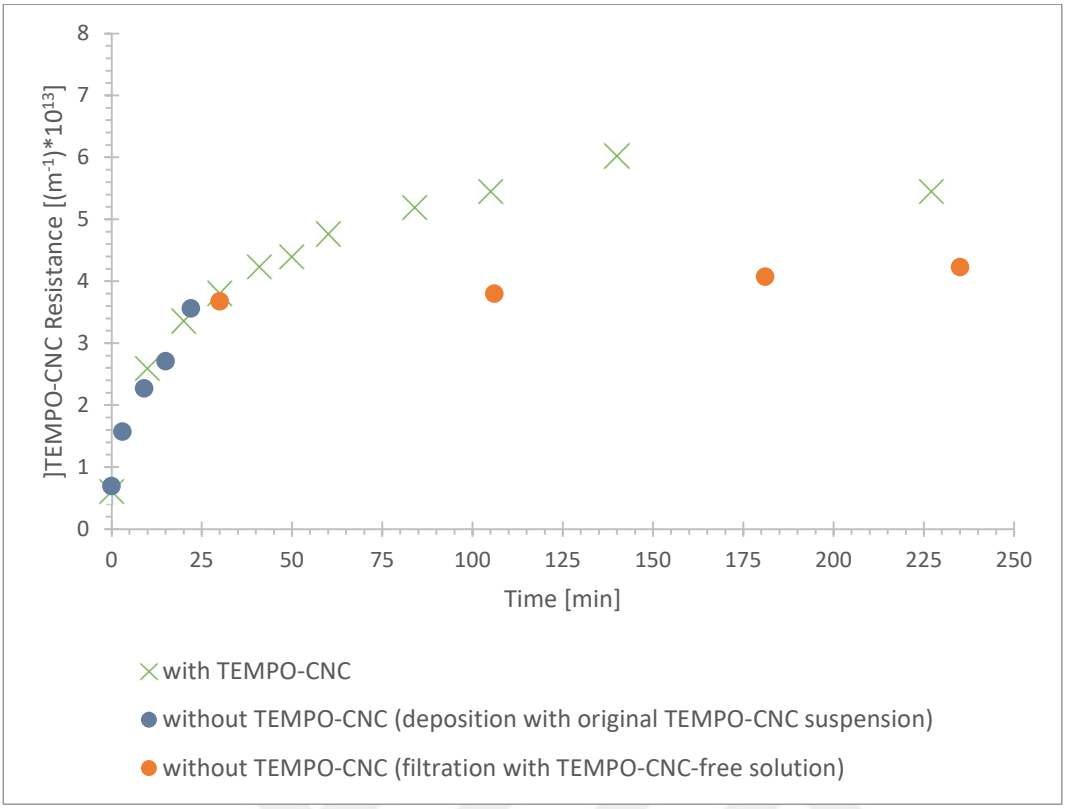

Figure 3-10. The comparison of TEMPO-CNC layer resistance of the samples prepared with and without 0.30% TEMPO-CNC with 5 mM NaCl

When Figure 3-10 was examined, it was seen that TEMPO-CNC layer resistances of both samples were quite similar up to thirty minutes, like the permeate fluxes. After half an hour, resistance of the sample with TEMPO-CNC increased up to 7 $\times 10^{13}$ m^{-1} . On the other hand, resistance of the sample without TEMPO-CNC did not increase much and stayed around 4 $\times 10^{13}$ m^{-1}.

As shown in Figure 3-9 and Figure 3-10, the resulting properties were not similar even though the same amount of shear was applied for the same time in both samples. Thus, the crucial point was not only the duration of applied shear but also how long the deposition of TEMPO-CNC took. Investigation of the optical properties of the samples prepared with the long deposition without TEMPO-CNC might be helpful. Thus, POM images of these samples without TEMPO-CNC were provided in Figure 3-11 and Figure 3-12.

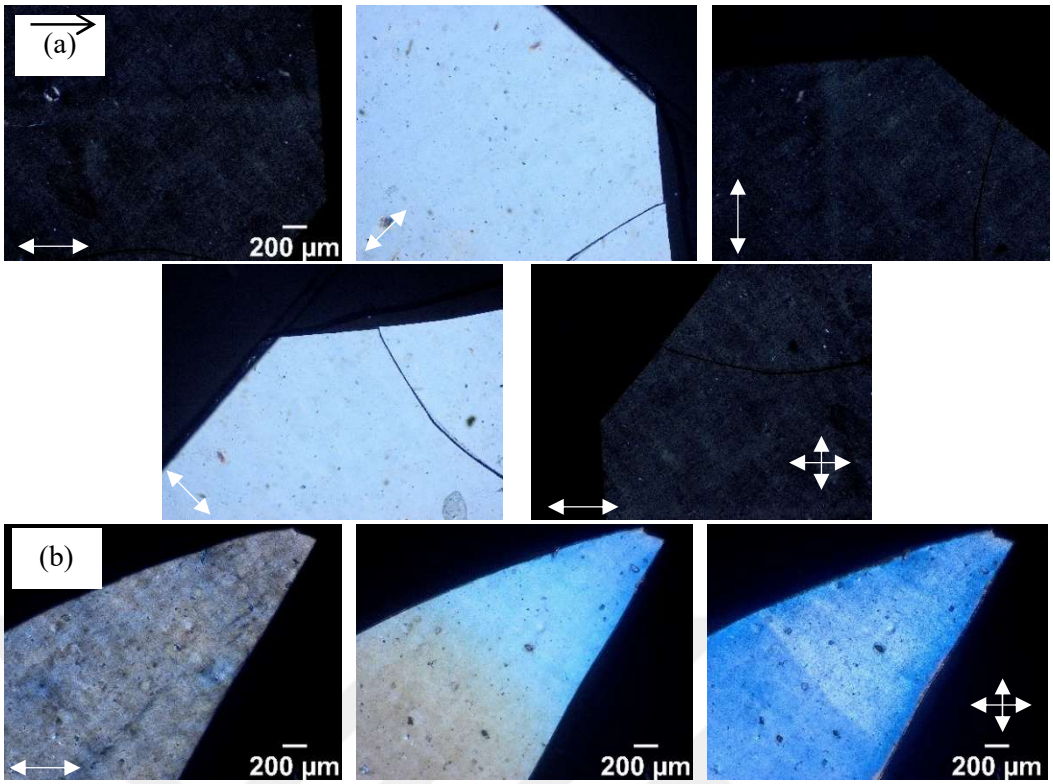

Figure 3-11. POM images of the sample prepared with a short deposition of 0.30% TEMPO-CNC and 5 mM NaCl, followed by the filtration without TEMPO-CNC. (a) Transmission images of the wet sample. (b) Reflection images of the sample during drying. Black arrow shows the direction of flow during the deposition. Single white arrow shows the sample position according to the analyzer. Cross white arrows show the direction of analyzer and polarizer.

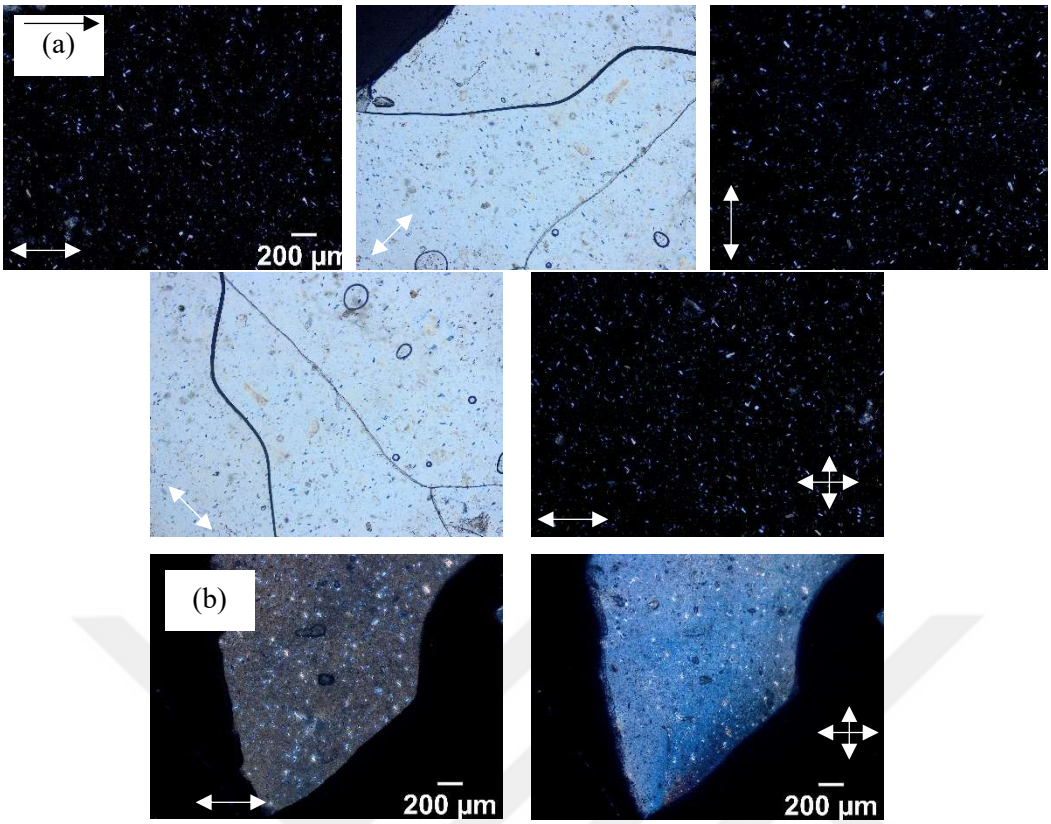

Figure 3-12. POM images of the sample prepared with a short deposition of 0.30% TEMPO-CNC and 5 mM NaCl, followed by the filtration without TEMPO-CNC. (a) Transmission images of the wet sample. (b) Reflection images of the sample during drying. Black arrow shows the direction of flow during the deposition. Single white arrow shows the sample position according to the analyzer. Cross white arrows show the direction of analyzer and polarizer.

When the wet samples were placed at 45° and 135° with the polarizer, strong birefringence was observed in the transmission mode under POM as seen in Figure 3-11 (a) and Figure 3-12 (a). This implies that the majority of TEMPO-CNCs were nematically aligned as seen in Figure 3-8 (b), the sample prepared by 30-minutes-long-deposition. Slight blue color shifts were observed for the drying samples as in Figure 3-11 (b) and Figure 3-12 (c), the reflection images. This slight shift was an indicator of a minor cholesteric structure present in these samples. A similar optical behavior was seen in the sample prepared with the deposition of 90 min and 1 h, as visible in Figure 3-8 (c) and Figure 3-8 (d) . At first glance, they could appear similar with the images of the longest deposition (Figure 3-8 (e)). However, it can be seen after a detailed look that the color shift from red to blue or at least from green to blue was more obvious in the drying images of the longest deposition. This color shift from red

to blue is mainly associated with the cholesteric phase as previously explained with the Bragg reflection. As can be seen from Equation 9, a decrease in the cholesteric pitch results in a decline of the wavelength of the reflected light. With the information that drying decreases the cholesteric pitch, it can be said that drying should induce a blue color shift due to decreased wavelength of the reflected light. However, as in Figure 3-11 (b) and Figure 3-12 (b), the dried samples instantly appeared as blue, rather than gradually appearing as blue while drying. Since they showed lack of selective reflection or Bragg reflection during drying, the dominant structure is determined to be nematic for the samples.

If the applied shear alone had the dominant role in the final structure, both nematic and cholesteric phases would present as in the sample with the longest deposition time (Figure 3-8 (e)). However, it was seen that the dominant phase is nematic as in the samples prepared with shorter depositions, 60 or 90 minutes. On the other hand, if only effective parameter was the TEMPO-CNC deposition duration, the sample prepared without TEMPO-CNC would be same as the sample prepared with 30-minutes deposition. However, the sample prepared without TEMPO-CNC was different than the sample having the same TEMPO-CNC deposition duration. Thus, the crucial role in the TEMPO-CNCs' phase is neither the duration of TEMPO-CNC deposition alone nor the applied shear only. Both shear and TEMPO-CNC duration affected the final structure. As the deposition time increases, there is a higher chance for the deposited layer to reorganize. Since the TEMPO-CNC deposit layer is a compressible gel, the layer is getting more compact as the deposition continues with the effect of applied transmembrane pressure. Deposition of more TEMPO-CNC particles resulted in higher density and concentration in the deposit layer. Thus, this increase in the TEMPO-CNC gel layer's concentration and density induced a reorganization in the layer as the TEMPO-CNC deposition proceeds. As a result of this reorganization in the layer structure, deposit layer with increased chiral symmetry was observed in the samples with longer depositions. For the shorter depositions, the majority of TEMPO-CNC particles were nematically aligned. As the deposition time increases, chiral nematic behavior is observed more due to the aforementioned rearrangement in the

deposit layer. As previously concluded, both nematic and cholesteric structures were present at the longest deposition.

Cholesteric and nematic phase formation mechanisms were investigated in detail. Since both nematic and chiral nematic structures are present in the samples prepared with the deposition of 0.30% TEMPO-CNC and 5 mM NaCl for 3 hours, further analysis was made with these samples. One of the questions that was tried to be answered is whether the first deposited TEMPO-CNC particles were nematic or cholesteric. It was thought to be that nematic structure was first formed since the longer depositions resulted in more cholesteric behavior. To understand when and where the cholesteric and nematic phases were formed, POM and SEM images were utilized. Deposited gel layer of TEMPO-CNC was cautiously taken from the support membrane to the surface of cover glass. Then, its images were taken in reflection and transmission modes under the cross-polarized microscope.

Reflection and transmission POM images of the formed TEMPO-CNC gel layer was given in Figure 3-13 and Figure 3-14. The difference in optical behaviors can be useful for understanding phase formation during the TEMPO-CNC depositions. Gray values of the images were calculated to see the intensity change between the figures. For these samples, the gray values plotted against the distance were provided in Appendix B. The difference in gray values between the images at 0° and 45° was calculated for both samples' transmission images. When the upper surface is bulk flow side, the average gray values are 74 and 135 at 0° and 45°, respectively. The maximum gray values are 94 and 157 at 0° and 45°. An intense birefringence was observed with these gray values, also in Figure 3-13, when the bulk flow side is the upper surface of the gel layer. Intense birefringence might be the result of higher amount of nematically aligned TEMPO-CNCs. When the upper surface is support membrane side, the average gray values are 121 and 104 at 0° and 45°, respectively. The maximum gray values at 0° and 45° are 139 and 132, respectively. Thus, a slight intensity change at 45° and 135° with the polarizer was observed in the POM images when the support membrane side is the upper surface as also visible in Figure 3-14. Thus, it can be deduced that the upper part of the gel layer, which is closer to the bulk flow, is more nematically aligned than the lower part of the gel layer that is closer to the support.

TEMPO-CNCs close to the support layer had higher tendency to have cholesteric structure. The opposite seemed to be more possible by considering the increase in cholesteric behavior with increasing deposition time. On the other hand, the possible reorganization of the structure with time should be taken into account, as previously discussed. Thus, the upper part of the deposit layer might have more nematically aligned TEMPO-CNCs even though samples prepared with shorter depositions showed strong nematic ordering and samples prepared with longer depositions showed more cholesteric behavior.

At this point, it is also important to consider the absorbance of TEMPO-CNC gel layers. There is a term called extinction coefficient (k) which is the combination of absorption and scattering coefficients and it indicates the total loss due to absorption and scattering. Having a higher extinction coefficient result in more light absorbance for the materials (Javadi et al., 2013). It was previously reported that cellulose and cellulose nanofiber films have significantly low extinction coefficients at the visible region of the light spectrum. Furthermore, it was stated that the extinction coefficient of cellulose nanofiber films was close to zero ($k \approx 0.0004$) for different film thicknesses (Duzik et al., 2019; Niskanen et al., 2019). Thus, the extinction coefficient of TEMPO-CNC films might also be assumed to be significantly low which means that the absorption per unit length of these films is not significantly high. It should be noted that the thickness of dried TEMPO-CNC gel layers are several tens of microns as previously seen in the cross-section SEM images. Wet gel layers should have even higher thickness than dried ones due to the shrinkage effect during drying. Even though the absorbance per unit length is significantly low, the total absorption can be nonnegligible in wet TEMPO-CNC gel layers. Therefore, the reflection from both the surface and a portion of the gel layer itself might contribute to the collected images. Still, the difference between the bulk flow and support membrane side exists in the transmission mode, as seen from Figure 3-13 (a) and Figure 3-14 (a). Thus, it is still valid to conclude that upper part of the TEMPO-CNC gel layer has more nematic ordering.

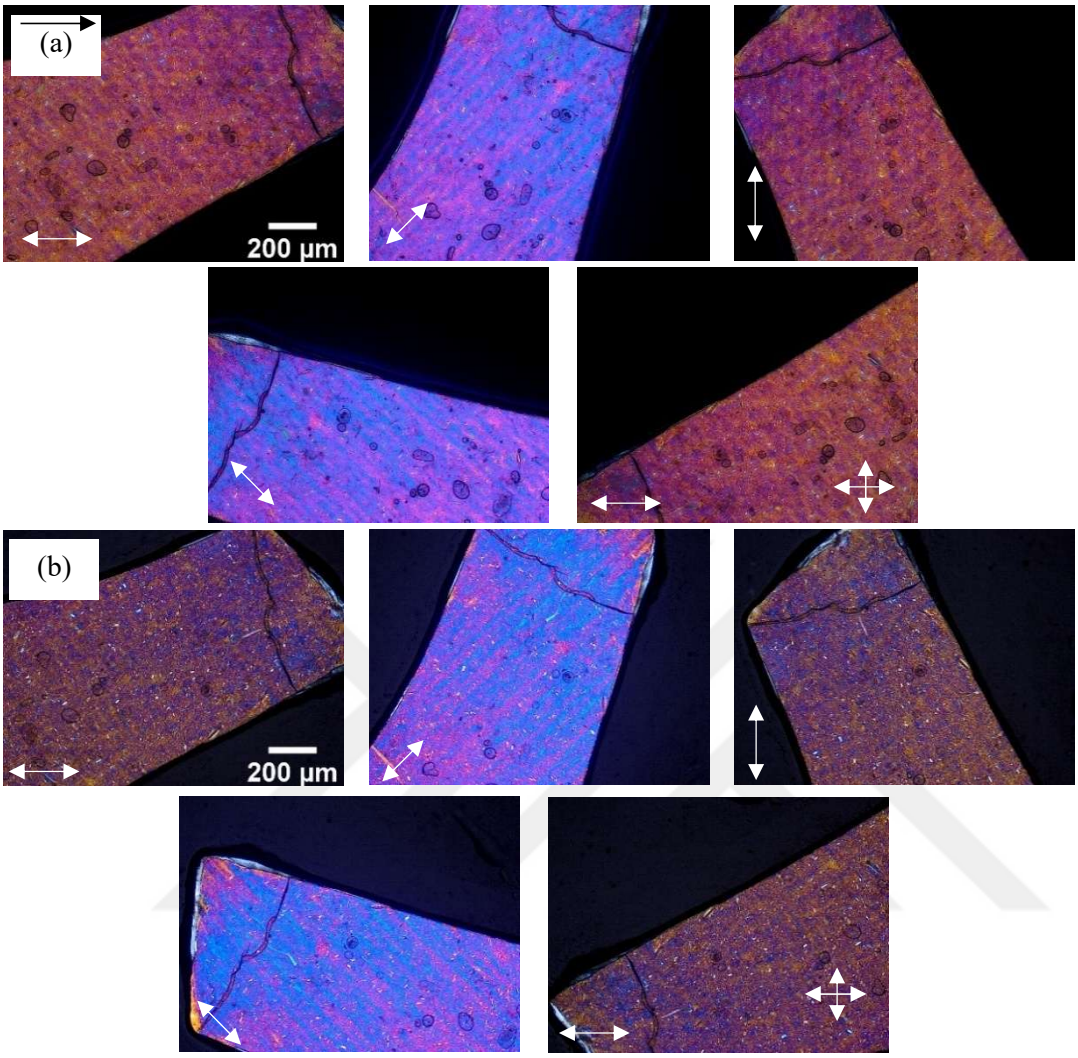

Figure 3-13. POM images of the sample with 0.30% TEMPO-CNC, 5 mM NaCl. Upper surface is the bulk flow side. (a) Reflection images of wet TEMPO-CNC gel layer. (b) Transmission images of wet TEMPO-CNC gel layer. Black arrow shows the direction of flow during the deposition. Single white arrow shows the sample position according to the analyzer. Cross white arrows show the direction of analyzer and polarizer.

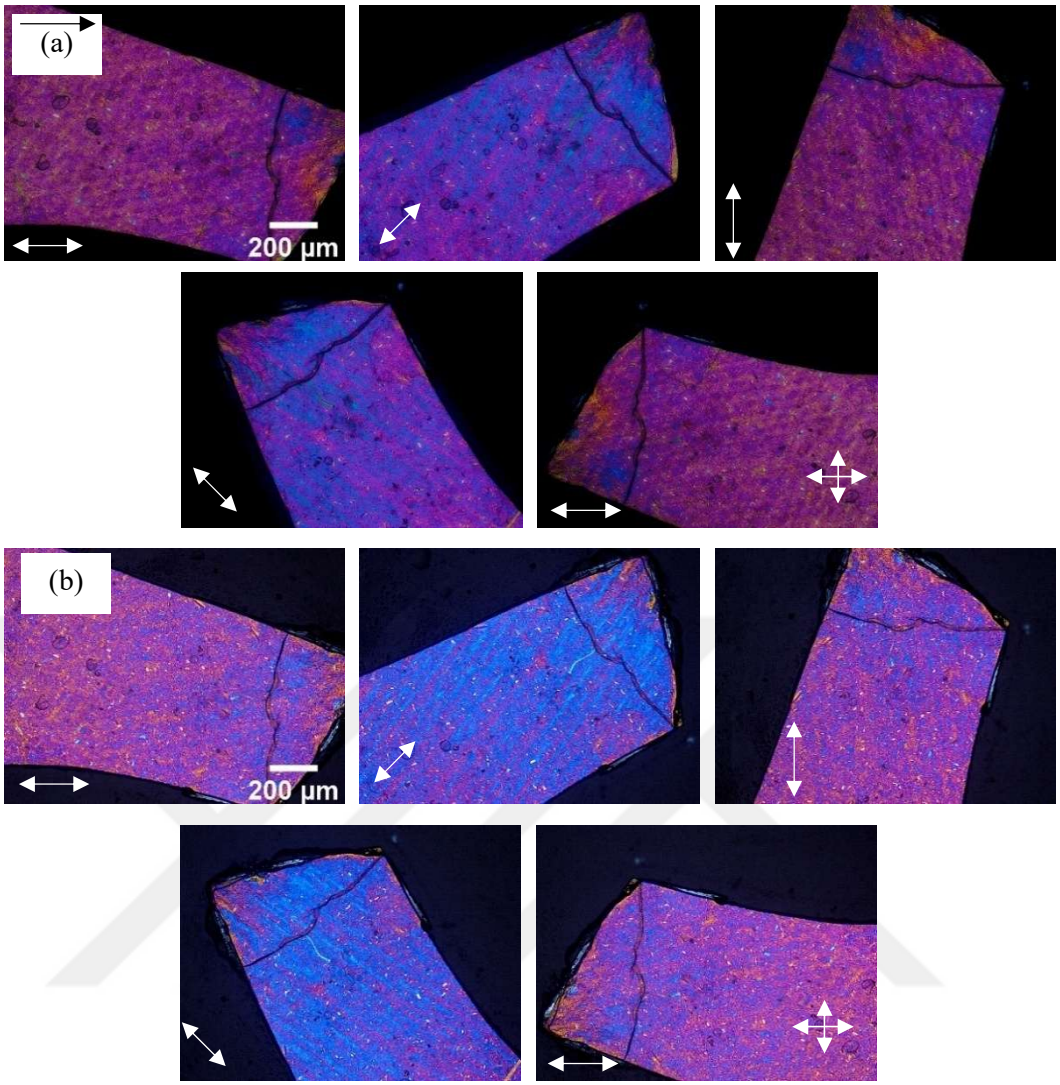

Figure 3-14. POM images of the sample with 0.30% TEMPO-CNC, 5 mM NaCl. Upper surface is the support membrane side. (a) Reflection images of wet TEMPO-CNC gel layer. (b) Transmission images of wet TEMPO-CNC gel layer. Black arrow shows the direction of flow during the deposition. Single white arrow shows the sample position according to the analyzer. Cross white arrows show the direction of analyzer and polarizer.

3.3 Salt Effect on the TEMPO-CNC Phase

Polarized optical images and SEM images were utilized to deduct information regarding the morphology and thickness in the deposit layers. For the salt concentrations, 0, 5, 10 and 100 mM in the TEMPO-CNC suspensions were considered.

3.3.1 0.075% TEMPO-CNC Suspensions

As seen in Figure 3-15 (a), there was no significant birefringence in the transmission images of the sample prepared by 0.075% TEMPO-CNC without NaCl under the cross-polarizers at 45° and 135° implying lack of nematic ordering. Additionally, it was seen in the reflection images taken when the upper surface is the bulk flow side (Figure 3-15 (b)) that the color was shifted from red to blue during drying of the sample. This blue color shift is a strong indicator of the presence of chiral nematic structure since this color shift occurs due to the Bragg reflection. This color shift can also be observed when the reflection images of the wet and dry samples are compared. The completely wet sample showed a red color, and this color changed to blue when it was completely dried due to decrease in the cholesteric pitch of the TEMPO-CNCs. Thus, it can be concluded that the significant portion of this TEMPO-CNC cake layer has cholesteric ordering.

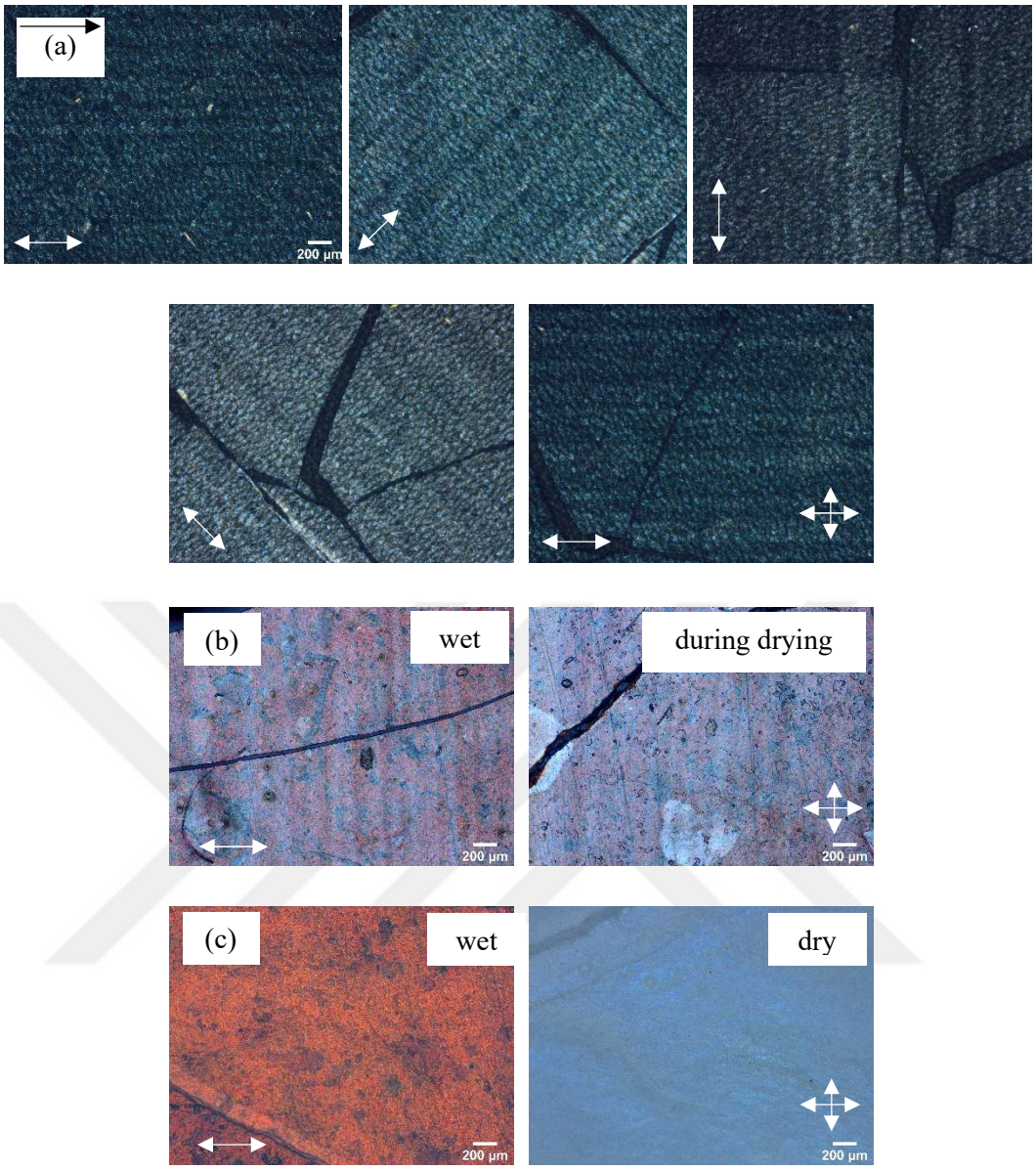

Figure 3-15. Polarized optical images of the cake layer prepared with 0.075% TEMPO-CNC and 0 mM NaCl. (a) Transmission images of the wet sample (b) Reflection images of the sample during drying. (c) Reflection images of the sample when it is completely wet (red) and when it is completely dry (blue). Black arrow shows the direction of flow during the deposition. Single white arrow shows the sample position according to the analyzer. Cross white arrows show the direction of analyzer and polarizer.

To understand the salt effect on the TEMPO-CNC cake layer structure, a similar analysis with the POM images were done for the salt concentrations of 5, 10 and 100 mM. Cross polarized optical images of the samples prepared with 0.075% TEMPO-CNC and 5 mM NaCl are provided in Figure 3-16 and Figure 3-17. It should be

considered that the first sample had approximately 30 minutes longer deposition duration since it took longer for that sample to have steady and constant flux. The first sample showed a slight birefringence under the cross-polarizers at 45° and 135° (Figure 3-16 (a)) which implies the nematic ordering. The reflection images of this one (Figure 3-16 (b)) showed Bragg reflection during drying which indicates the presence of chiral nematic structure. The second sample showed birefringence under the cross-polarizers at 45° and 135° as seen in Figure 3-17 (a), which indicated the presence of nematic ordering. Like the first one, the reflection images in Figure 3-17 (b) indicated the blue shift while the sample was drying. This Bragg reflection shows the presence of cholesteric structure. On the other hand, the blue color is lighter and less vibrant in this case. Thus, it might be said that not only the presence but also the appearance of colors in the polarized optical images may be an indicator of the degrees of the nematic or chiral nematic phases of TEMPO-CNC. Both samples prepared with 0.075% TEMPO-CNC and 5 mM showed both nematic and cholesteric ordering. The first one (Figure 3-16) showed more significant cholesteric ordering while the second one (Figure 3-17) showed more significant nematic ordering in their structures. The reason might be the duration of TEMPO-CNC filtration. As mentioned, the first sample had longer deposition duration thus this longer period may allow more time for more reorganization in the structure. This optical analysis also showed that slightly longer deposition duration can have significant impacts on the dominant ordering in the TEMPO-CNC structure even though the bulk TEMPO-CNC and salt concentration are constant.

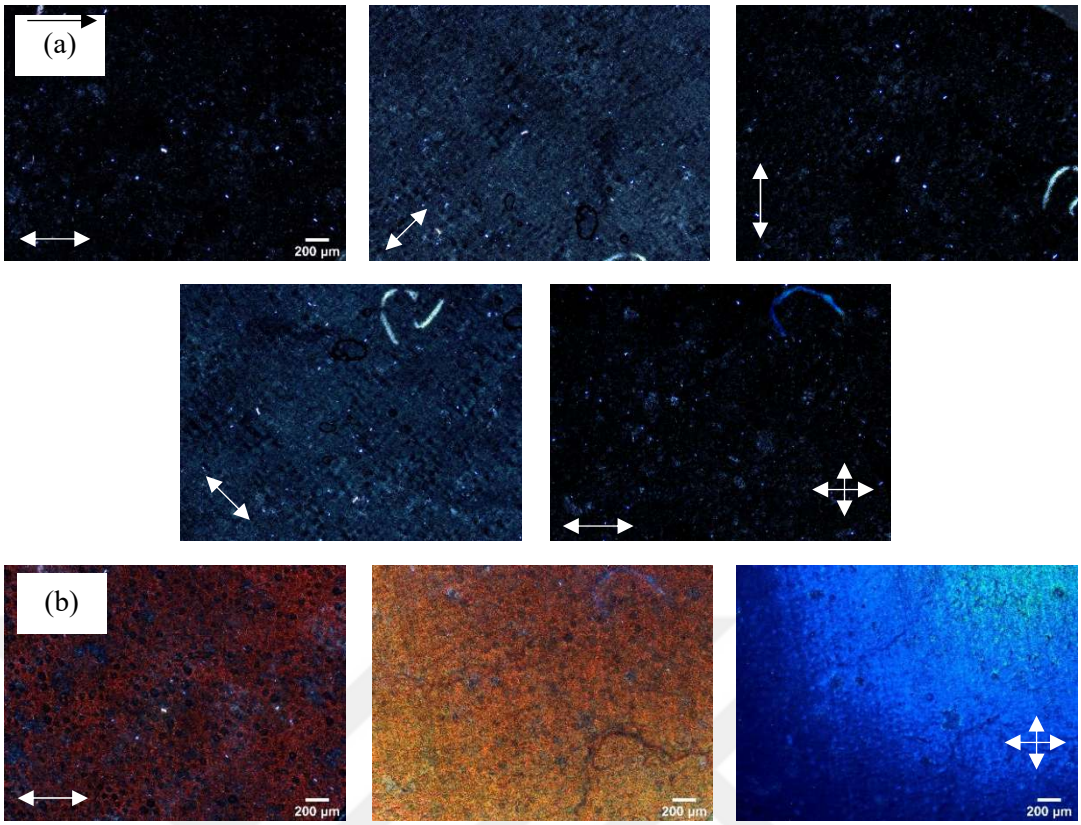

Figure 3-16. Polarized optical images of the cake layer prepared with 0.075% TEMPO-CNC and 5 mM NaCl. (a) Transmission images of the wet sample (b) Reflection images of the sample during drying. Black arrow shows the direction of flow during the deposition. Single white arrow shows the sample position according to the analyzer. Cross white arrows show the direction of analyzer and polarizer.

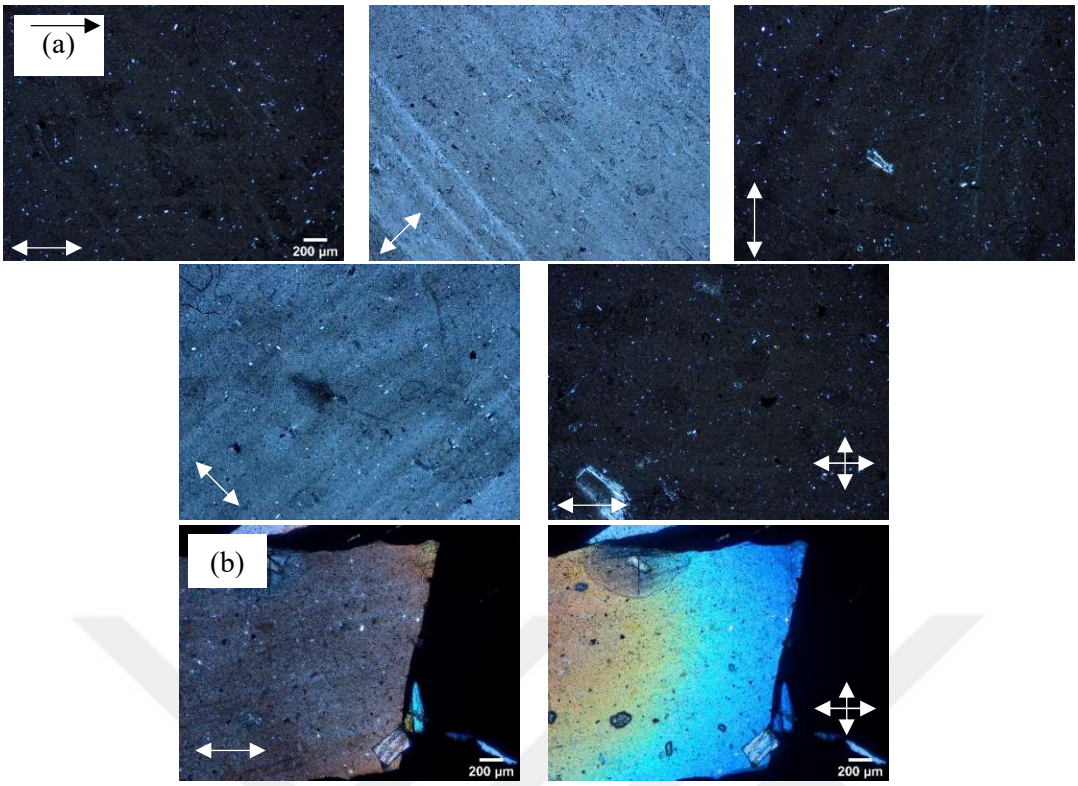

Figure 3-17. Polarized optical images of the second cake layer prepared with 0.075% TEMPO-CNC and 5 mM NaCl. (a) Transmission images of the wet sample (b) Reflection images of the sample during drying. Black arrow shows the direction of flow during the deposition. Single white arrow shows the sample position according to the analyzer. Cross white arrows show the direction of analyzer and polarizer.

Figure 3-18 and Figure 3-19 shows the POM images of the samples prepared with 0.075% TEMPO-CNC with 10 mM NaCl. As seen in the cross polarized transmission images of the first one, in Figure 3-18 (a), there was a slight birefringence at 45° and 135°. Additionally, the second one also showed birefringence at 45° and 135° under the cross polarizers as seen in Figure 3-19 (a) implying the presence of nematic ordering. The reflection images of both samples (Figure 3-18 (b) and Figure 3-19 (b)) indicated a blue color shift due to Bragg reflection during the drying under the microscope which is a sign of cholesteric phase. It was seen in Figure 3-19 (b) that red color was visible before the appearance of color shift for the second one. The first deposit layer had a darker appearance and there was no significant color as seen in Figure 3-18 (b). It might give information regarding the cholesteric phases of these two samples. When the reflection images of wet samples in Figure 3-18 (c) and Figure 3-19(c) are compared, it was seen that the second deposit layer has a more reddish color than the first one. Thus, it was concluded that the initial pitch size of the first

sample was higher than the second one. This higher pitch size results in reflection in infrared light region and no appearance of red at the beginning of drying. However, the pitch size became smaller during the drying and the reflection was shifted from infrared region to visible light region. So, the red color started to appear during the drying of the first sample as observable in Figure 3-18 (b). Since the second one has already a smaller pitch size from the beginning, its color was reddish even before the drying started. Even though their cholesteric pitches were not the same, both samples prepared with 0.075% TEMPO-CNC and 10 mM NaCl showed nematic and cholesteric ordering in their structures.

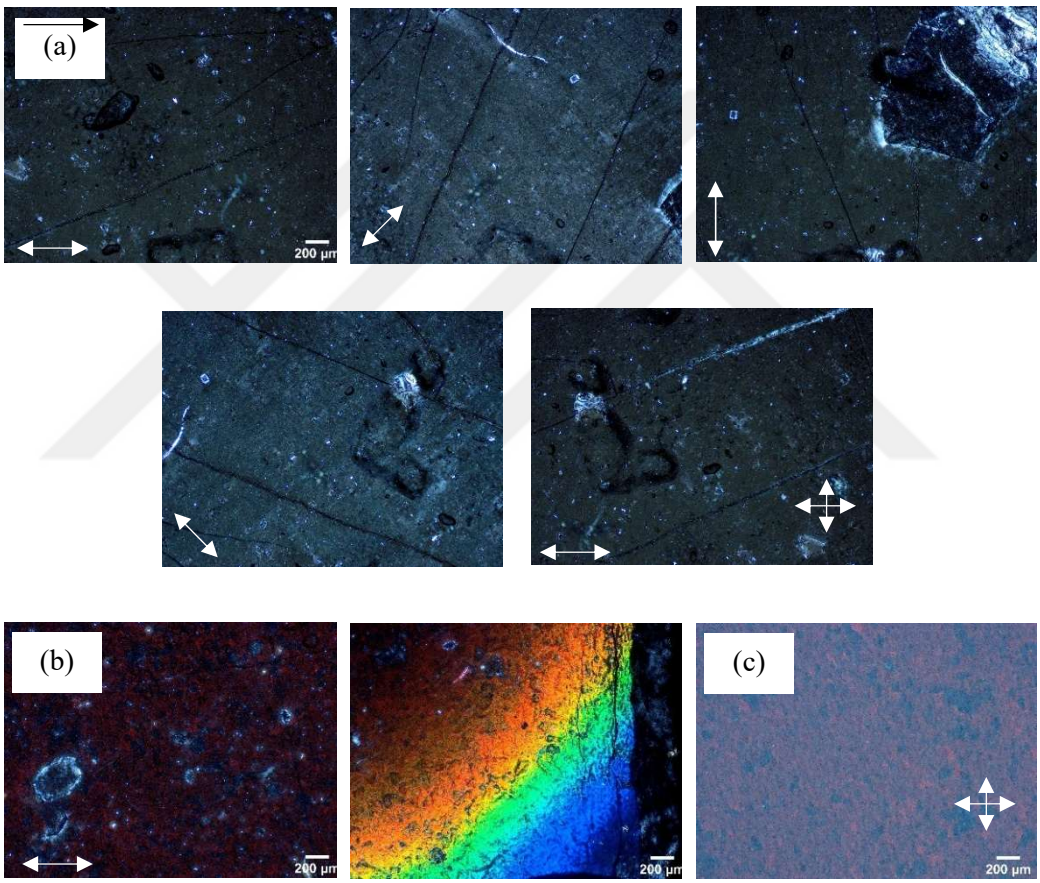

Figure 3-18. Polarized optical images of the sample with 0.075% TEMPO-CNC and 10 mM NaCl. (a)Transmission images of the wet sample (b) Reflection images of the sample during drying. (c) Reflection images of the sample when it is completely wet. Black arrow shows the direction of flow during the deposition. Single white arrow shows the sample position according to the analyzer. Cross white arrows show the direction of analyzer and polarizer.

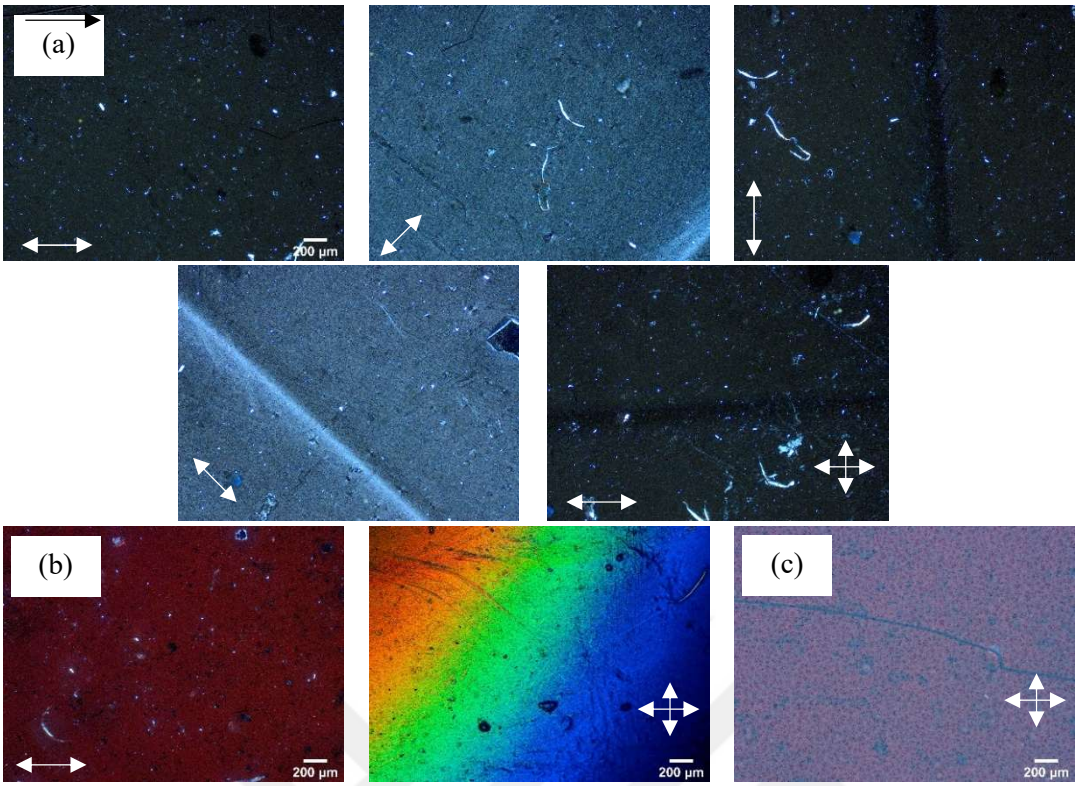

Figure 3-19. Polarized optical images of the sample with 0.075% TEMPO-CNC and 10 mM NaCl. (a) Transmission images of the wet sample (b) Reflection images of the sample during drying. (c) Reflection images of the sample when it is completely wet. Black arrow shows the direction of flow during the deposition. Single white arrow shows the sample position according to the analyzer. Cross white arrows show the direction of analyzer and polarizer.

As seen in Figure 3-20 (a), in the sample prepared with 0.075% TEMPO-CNC with 100 mM NaCl there was no change in the color or intensity in the transmission mode when the degree of sample was changed according to polarizer. Therefore, there was no nematic ordering observed. However, the color shift from red to blue was observed in the reflection mode while the sample was drying as observable in Figure 3-20 (b). Thus, it can be said that the TEMPO-CNC layer has Bragg reflection and chiral nematic behavior. Another remarkable result was the presence of shiny spots on the deposit layer surface. These spots were thought to be the cluster of some crystals, TEMPO-CNC aggregates in the cake layer. The presence of these aggregates was expected for higher salt concentrations since previous studies showed their presence in the similar systems of CNC (Kocaman et al., 2021).

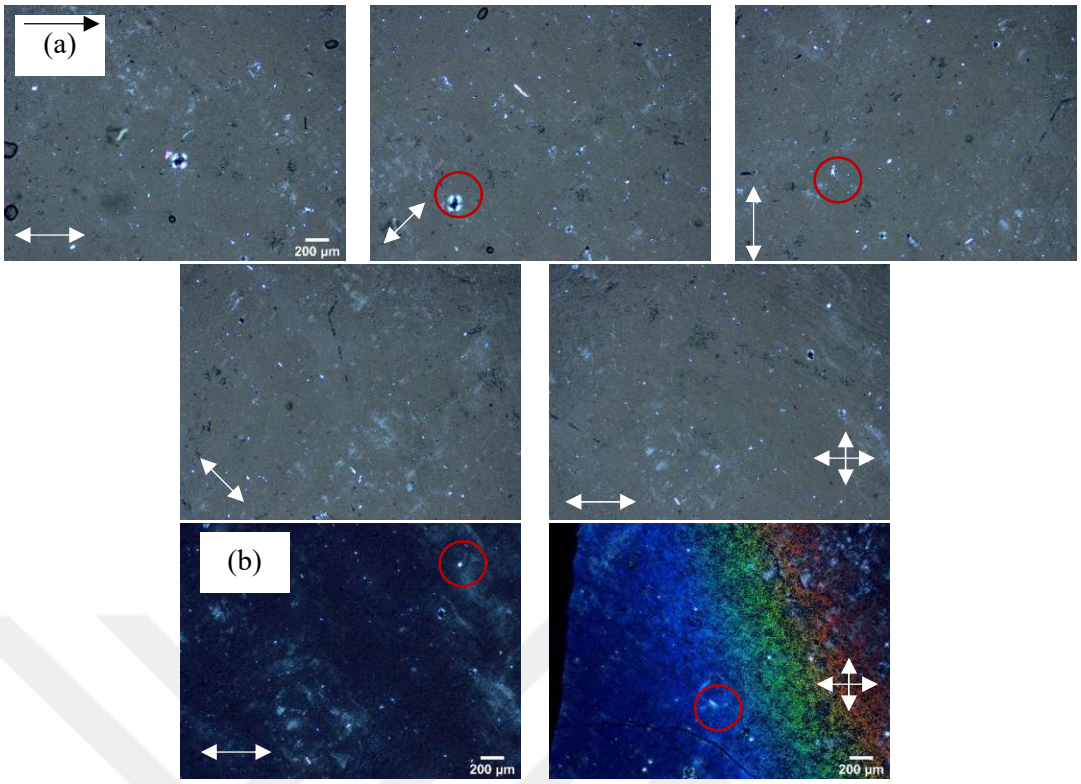

Figure 3-20. Polarized optical images of the sample with 0.075% TEMPO-CNC and 100 mM NaCl. (a) Transmission images of the wet sample (b) Reflection images of the sample during drying. Single white arrow shows the sample position according to the analyzer. Cross white arrows show the direction of analyzer and polarizer. Red circles show some of the aggregates.

3.3.2 0.15% TEMPO-CNC Deposition

According to Figure 3-21 (a), the reflection images of the sample prepared by the deposition of 0.15% TEMPO-CNC without salt showed the presence of cholesteric structure. The completely wet sample appeared as red under the cross polarizers and blue when it was completely dry as seen in Figure 3-21 (b). This color shift was also observed during the drying as seen in Figure 3-21 (a). As seen in Figure 3-21 (c), no birefringence was observed at 45° and 135° at transmission mode of POM. Hence, it can be concluded that this sample prepared with 0.15% TEMPO-CNC and 0 mM NaCl showed no nematic symmetry but showed cholesteric structure.

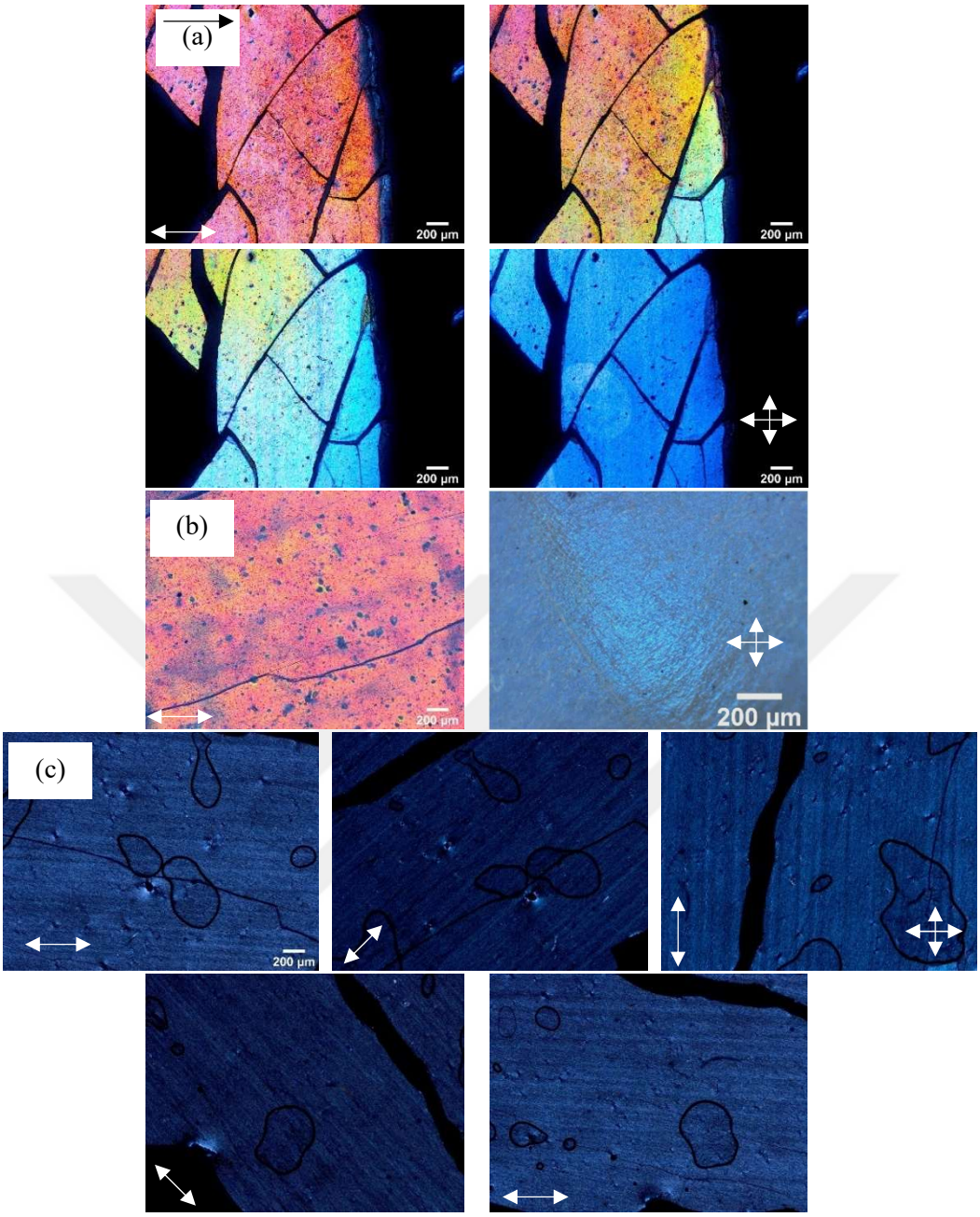

Figure 3-21. Polarized optical images of the sample with 0.15% TEMPO-CNC and 0 mM NaCl. (a) Reflection images of the sample during drying. (b) Reflection images of the sample when it is completely wet (reddish) and when it is completely dry (blue). (c) Transmission images of the wet sample. Single white arrow shows the sample position according to the analyzer. Cross white arrows show the direction of analyzer and polarizer.

The transmission images of samples prepared with the deposition of 0.15% TEMPO-CNC with 5 mM NaCl indicated the intensity change at 45° and 135° under the cross polarizers as seen in Figure 3-22 and Figure 3-23. Thus, both have nematic symmetry. When the reflection images of the drying samples in Figure 3-22 (b) and Figure 3-23 (b) were examined, the blue shift was observed as time passed. Thus, the presence of cholesteric structure was also deducted from these images for both. As observed in Figure 3-22 (c) and Figure 3-23 (c), completely wet samples in the reflection mode appeared as orange and colorless, respectively. This can also be seen from the first reflection images of the drying samples. The difference might arise from the layers' different cholesteric pitch sizes; the second one should have higher cholesteric pitch. In conclusion, both samples prepared with 0.15% TEMPO-CNC and 5 mM NaCl were found to have nematic and cholesteric ordering in their TEMPO-CNC structures.

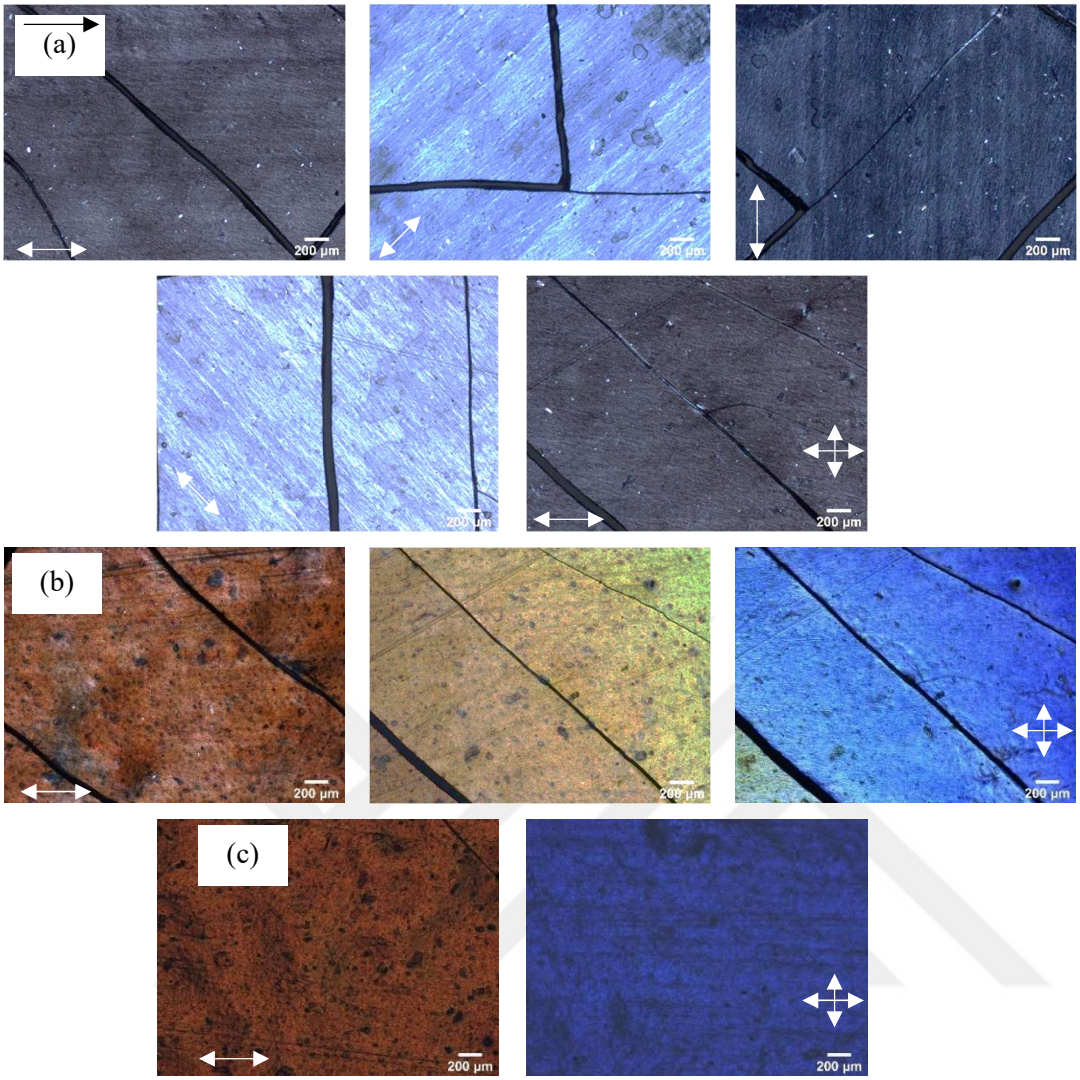

Figure 3-22. Polarized optical images of the sample with 0.15% TEMPO-CNC and 5 mM NaCl. (a)Transmission images of the wet sample (b) Reflection images of the sample during drying. (c) Reflection images of the sample when it is completely wet and when it is completely dry (blue). Black arrow shows the direction of flow during the deposition. Single white arrow shows the sample position according to the analyzer. Cross white arrows show the direction of analyzer and polarizer.

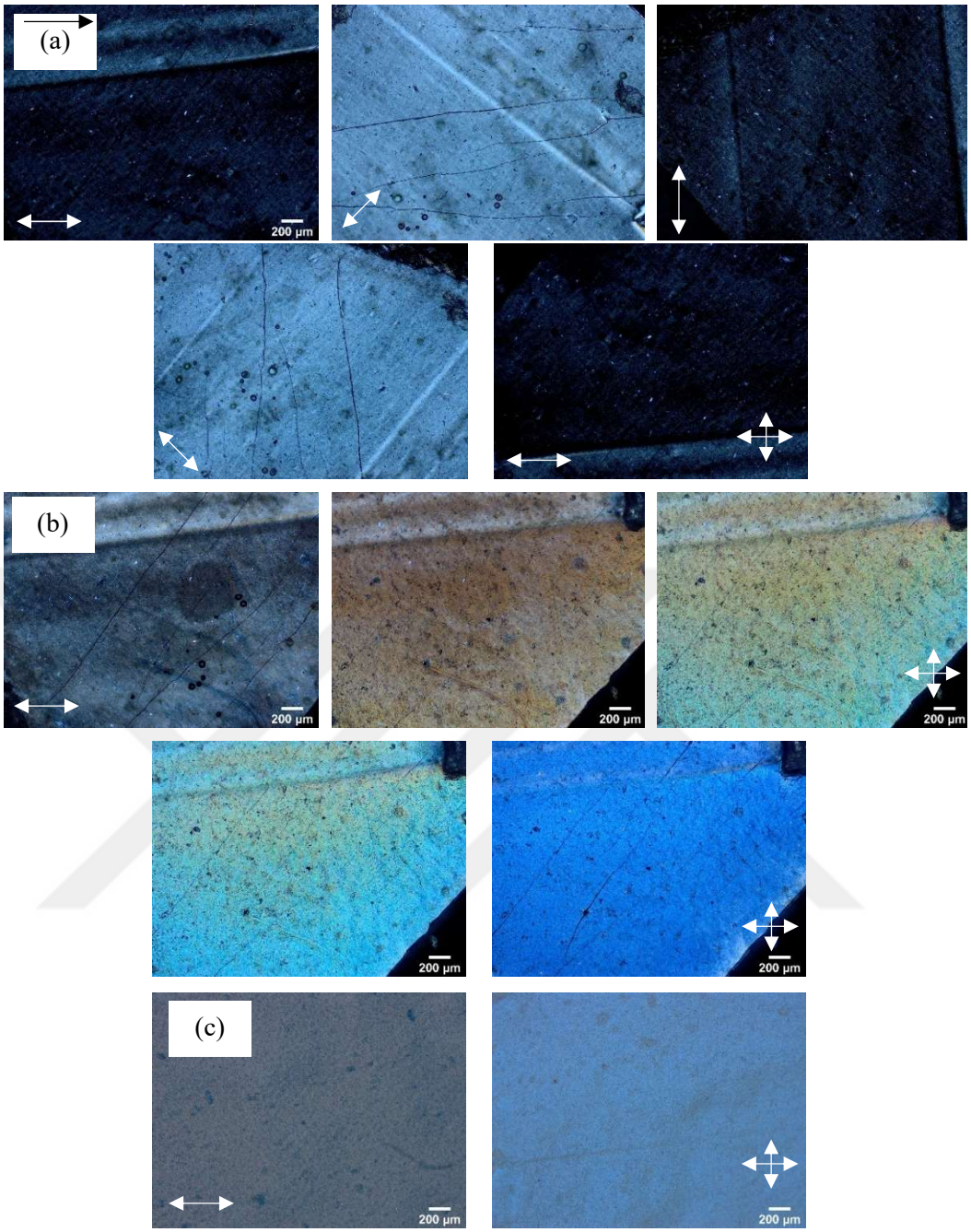

Figure 3-23. Polarized optical images of the second sample with 0.15% TEMPO-CNC and 5 mM NaCl. (a)Transmission images of the wet sample (b) Reflection images of the sample during drying. (c) Reflection images of the sample when it is completely wet and when it is completely dry (blue). Black arrow shows the direction of flow during the deposition. Single white arrow shows the sample position according to the analyzer. Cross white arrows show the direction of analyzer and polarizer.

As seen in Figure 3-24 (a), no significant birefringence was observed in the transmission images of the sample prepared by the deposition of 0.15% TEMPO-CNC with 10 mM NaCl. Therefore, it can be deduced that this cake layer does not show a significant nematic symmetry. The reflection images in Figure 3-24 (b) revealed that the color was shifted from red to blue during the drying process as an indication of Bragg reflection and therefore as an indication of presence of a chiral nematic structure in the deposit layer. To conclude, the sample prepared with the deposition of 0.15% TEMPO-CNC and 10 mM NaCl showed only cholesteric behavior.

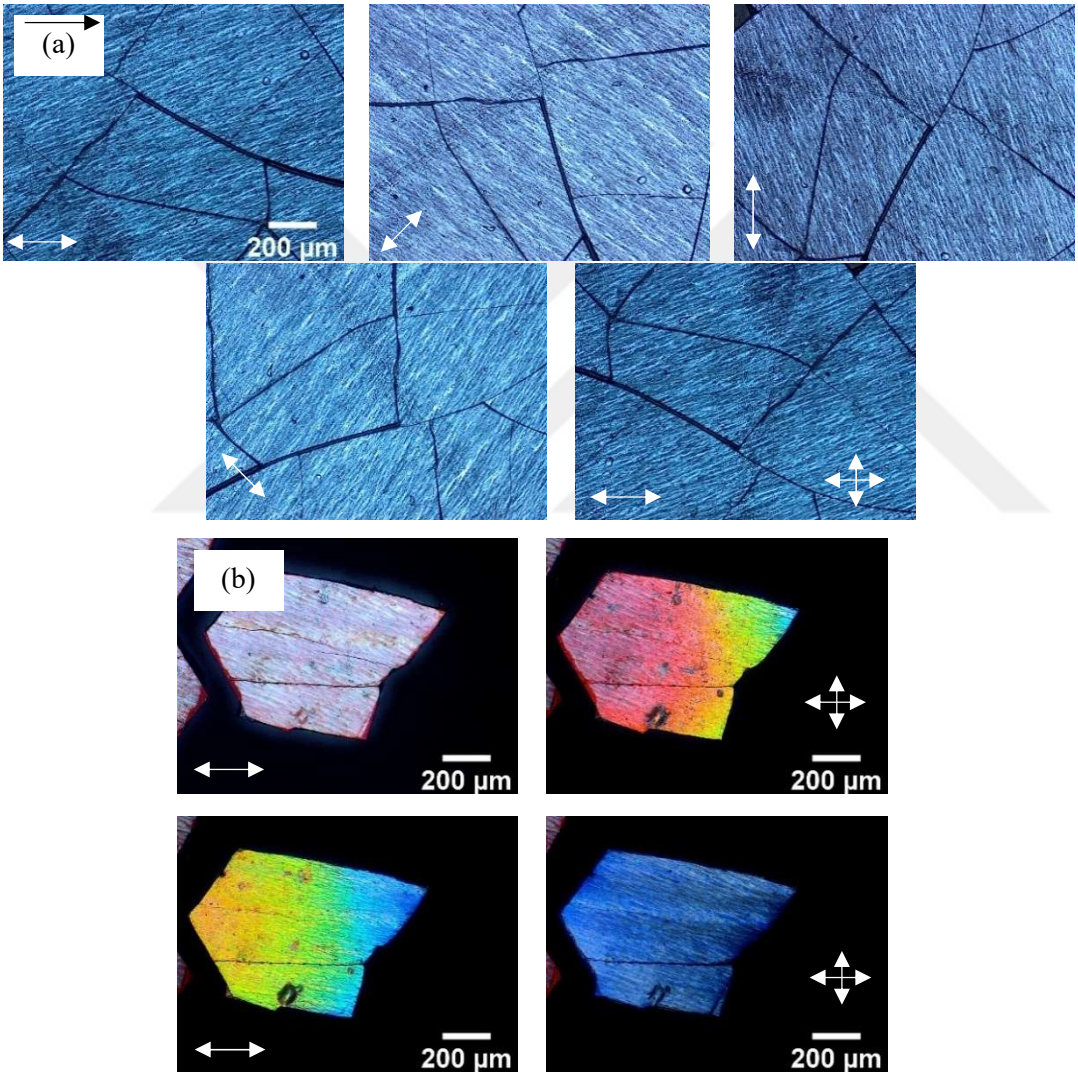

Figure 3-24. Polarized optical images of the sample with 0.15% TEMPO-CNC and 10 mM NaCl. (a)Transmission images of the wet sample (b) Reflection images of the sample during drying. Single white arrow shows the sample position according to the analyzer. Cross white arrows show the direction of analyzer and polarizer.

In the sample prepared with 0.15% TEMPO-CNC with 100 mM NaCl, blue shift was clearly observed in Figure 3-25 (a) under the cross polarizers with the reflection mode. Moreover, the completely wet layer appeared as reddish under the cross polarizers and with the reflection mode as seen in Figure 3-25 (b). Therefore, it can be concluded that the TEMPO-CNCs have cholesteric structure under these conditions. The sample was observed in the transmission mode of the microscope by changing the angle of sample to the polarizer in order to investigate the presence of nematic phases in the TEMPO-CNC. As seen in Figure 3-25 (c), no birefringence, thus, no nematic symmetry was observed. Additionally, some TEMPO-CNC aggregates onto the membrane were observed as the bright spots in the POM images of this cake layer. The formation of aggregates was expected at these salt concentrations, which was also the case for other samples prepared with different TEMPO-CNC bulk concentrations with the salt concentration of 100 mM. Additionally, presence of aggregates in the sample prepared with the same TEMPO-CNC and NaCl was observed in one of the previous studies in the literature (İçten et al., 2024). Also, in that study, it was noted that this sample showed cholesteric behavior under the POM, as stated here too.

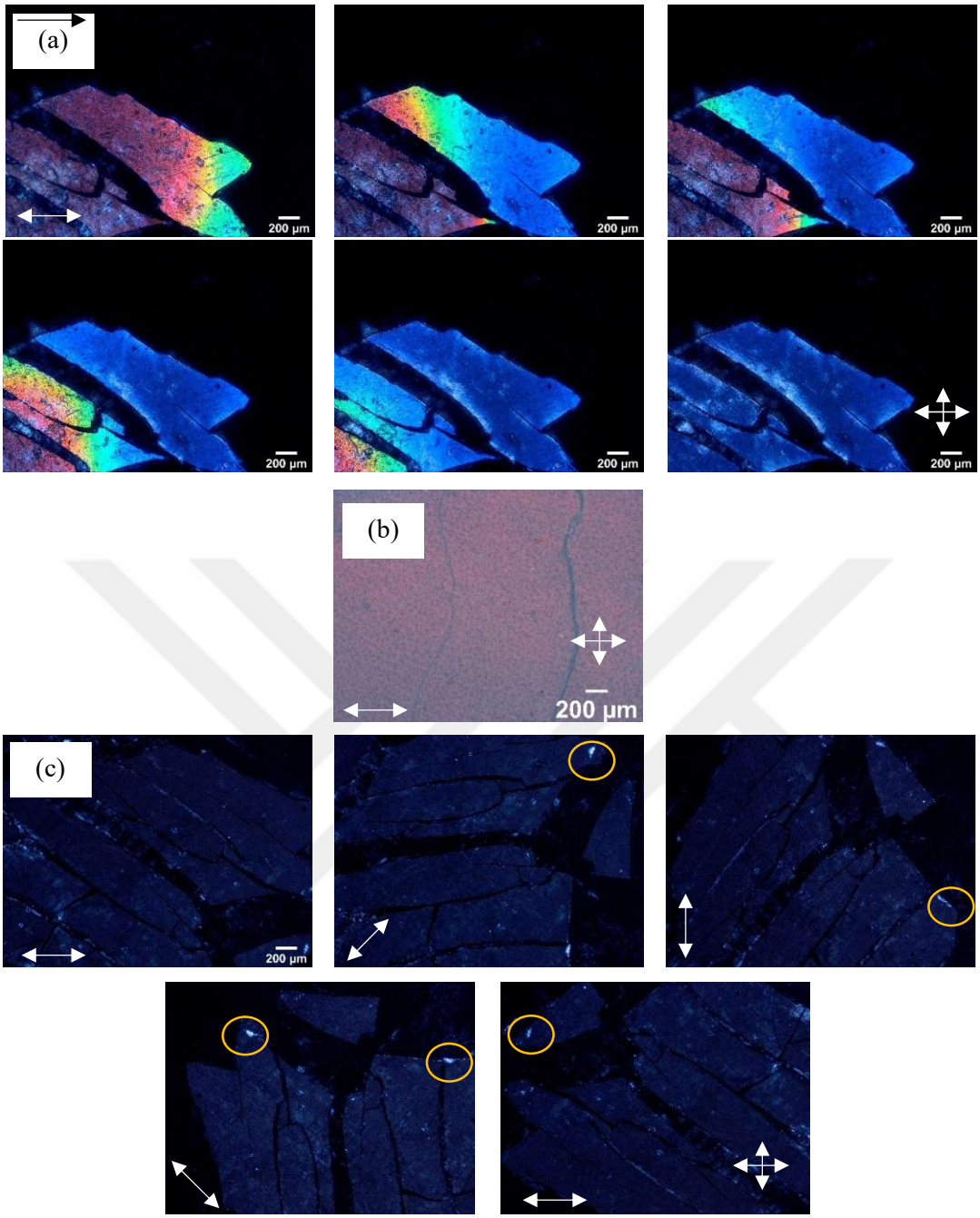

Figure 3-25. Polarized optical images of the sample with 0.15% TEMPO-CNC and 100 mM NaCl. (a) Reflection images of the sample during drying. (b) Reflection images of the sample when it is completely wet (reddish). (c) Transmission images of the wet sample. Single white arrow shows the sample position according to the analyzer. Cross white arrows show the direction of analyzer and polarizer. Yellow circles show the formed aggregates.

3.3.3 0.30% TEMPO-CNC Filtration

It was observed that the intensity of the transmission images of the sample prepared with 0.30% TEMPO-CNC without salt increased at the angles of 45° and 135° as seen in Figure 3-26 (a). Thus, the TEMPO-CNC deposit layer has a nematic ordering. The reflection images of the sample in Figure 3-26 (b) indicated no Bragg reflection during the drying under the microscope. However, it might be due to having significantly big cholesteric pitch size and having a Bragg reflection that is outside of the visible light region. To verify this hypothesis, cross-section SEM image of the dried sample provided in Figure B-1 was utilized. the layered morphology was seen, and the cholesteric pitch was measured to be 0.912 ± 0.08 μm. By utilizing the Bragg reflection (Equation 9), the wavelength of the reflected light was found to be 1423 nm. The details of this calculation can be found in Appendix B. This wavelength corresponds to near-infrared (NIR) region of the light spectrum (Palmer & Grant, 2010). Hence, it was concluded that the pitch size of the wet sample is even bigger than 1423 nm, which is too big to have a Bragg reflection in the visible region, and this can be the reason of lack of color shift during drying under the POM (Figure 3-26 (b)). Most probably, Bragg reflection occurred in the NIR region and then it rapidly turned to blue as seen in the final image of Figure 3-26 (b). In the literature, there were several studies reporting the presence of cholesteric CNC films with relatively bigger pitch sizes in micrometer scale (Frka-Petesic et al., 2019; Lin et al., 2021; Parton et al., 2022b).

As seen in Figure 3-26, several stripes were present in both the transmission and reflection modes under POM which might mean thickness or pitch inhomogeneity in the structure. Additional POM images of the sample were taken in reflection and transmission modes at the angle of 10°. The thickness fluctuations in these additional images can be seen in Figure 3-27. Also, there exist local colorful regions which might be an indicator of local cholesteric domains in the structure. Thus, there might be a non-uniformity in the thickness and cholesteric pitch, but the evidence of cholesteric structure was also seen in Figure 3-27.

Even though the visible Bragg reflection was not observed during the drying, the presence of cholesteric structure was seen in the SEM and POM images. As a

conclusion, the sample prepared with 0.30% TEMPO-CNC and no NaCl showed both nematic and cholesteric ordering in its structure.

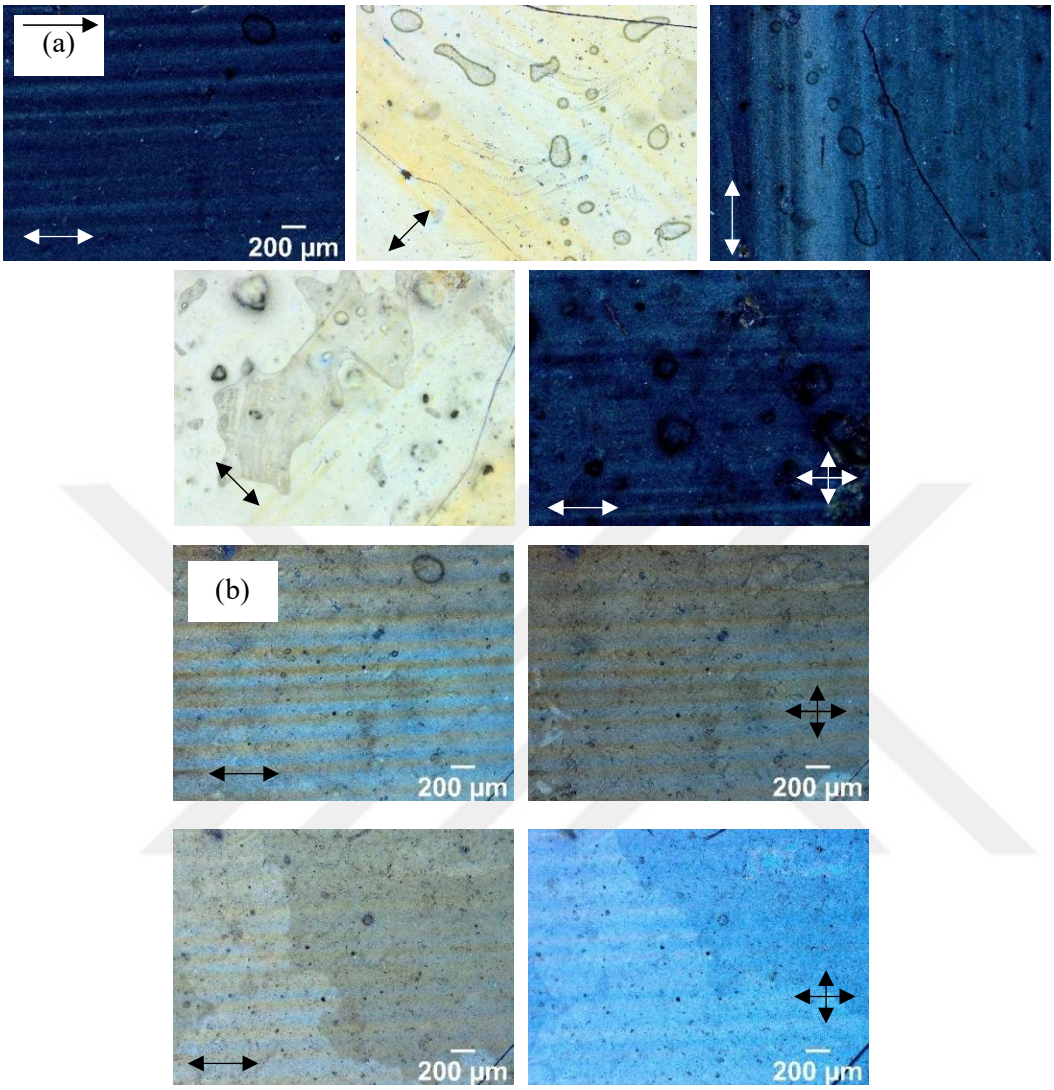

Figure 3-26. Polarized optical images of the sample with 0.30% TEMPO-CNC and 0 mM NaCl. (a) Transmission images of the wet sample (b) Reflection images of the sample during drying. Single white and black arrows show the sample position according to the analyzer. Cross white and black arrows show the direction of analyzer and polarizer.

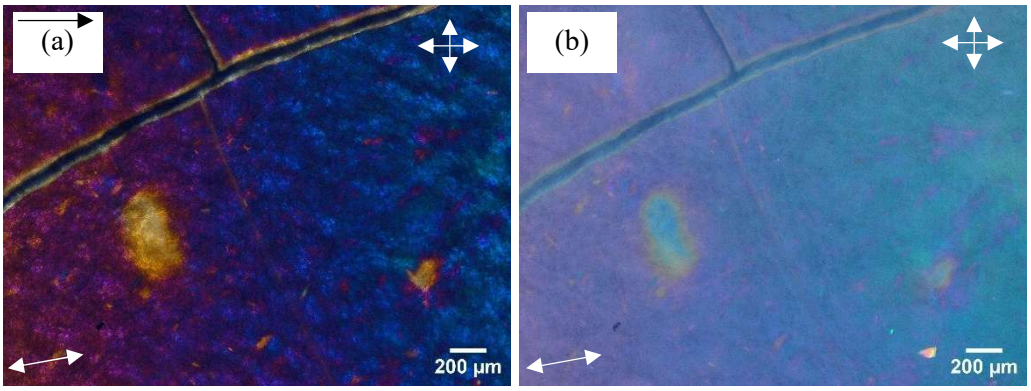

Figure 3-27. Polarized optical images of the sample with 0.30% TEMPO-CNC and 0 mM NaCl. (a) Transmission image of the wet sample at 10° (b) Reflection image of the sample at 10°. Single white arrows show the sample position according to the analyzer. Cross white arrows show the direction of analyzer and polarizer.

As seen in Figure 3-28 (a), sample prepared with 0.30% TEMPO-CNC, 5 mM NaCl appeared darker at 0°, 90° and 180° with respect to analyzer, while it showed birefringence at 45° and 135°. This presence of birefringence indicates the nematic alignment of some TEMPO-CNC particles. Also, the blue shift occurred while the sample was drying under the microscope. This color shift indicates the presence of Bragg reflection and chiral nematic structure in the sample. Therefore, this sample showed both cholesteric and nematic behaviors under cross polarized optical microscopy. This biphasic behavior was also observed in some other samples prepared with different bulk TEMPO-CNC and NaCl concentrations. However, ten samples were prepared with 0.30% TEMPO-CNC and 5 mM NaCl and both the nematic and cholesteric behavior were observed in all of these ten ones. Furthermore, 0.30% TEMPO-CNC and 5 mM NaCl were thought to be the suitable conditions for further observations in TEMPO-CNC phase to understand the resulting structure.

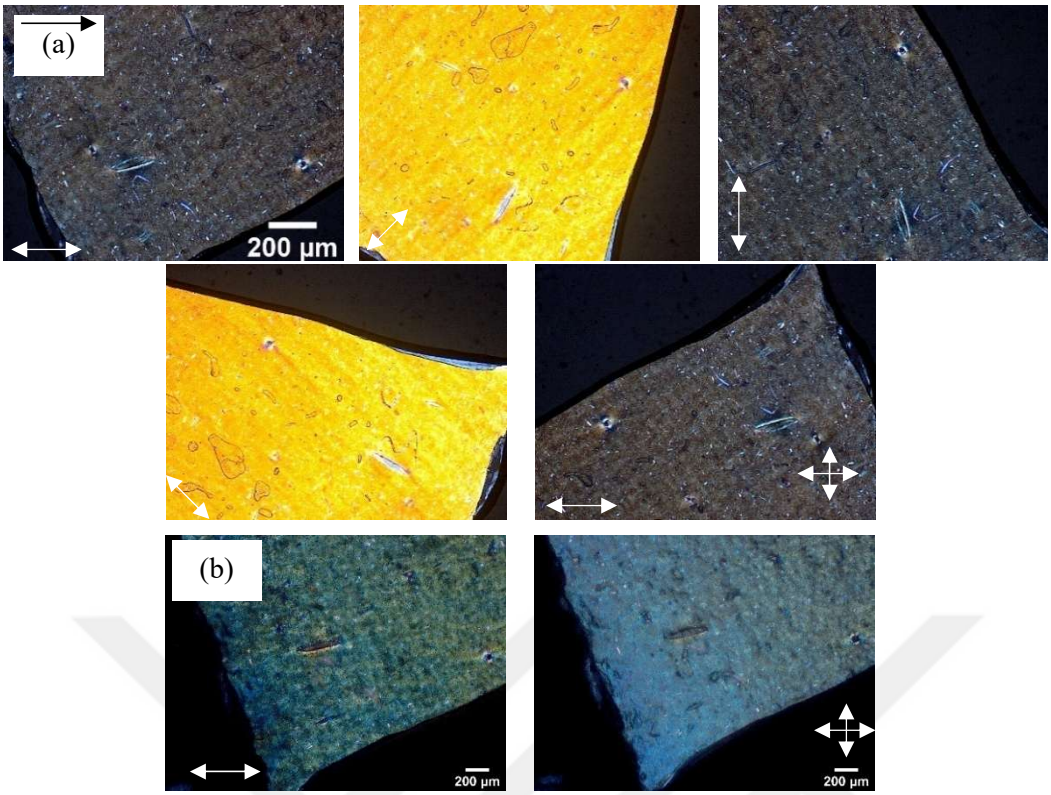

Figure 3-28. Polarized optical images of the sample with 0.30% TEMPO-CNC and 5 mM NaCl. (a)Transmission images of the wet sample (b) Reflection images of the sample during drying. Black arrow shows the direction of flow during the deposition. Single white arrows show the sample position according to the analyzer. Cross white arrows show the direction of analyzer and polarizer.

Figure 3-29 and Figure 3-30 shows the POM images of the two samples prepared by the deposition of 0.30% TEMPO-CNC with 10 mM salt under the cross polarizers. The first one showed a slight birefringence as seen in the transmission images in Figure 3-29 (a). The second one appeared darker at 0°, 90° and 180° as seen in the transmission images in Figure 3-30 (a). At 45° and 135°, it appeared lighter and brighter which implies the presence of nematic structure. When the reflection images of drying layers were examined, the color shift from red to blue was seen clearly for the first sample as seen in Figure 3-29 (b). Moreover, the blue shift was also observed in the second one as observed in Figure 3-30 (b), which concludes the presence of both nematic and chiral nematic phases in the sample prepared with the deposition of 0.30% TEMPO-CNC and10 mM NaCl.

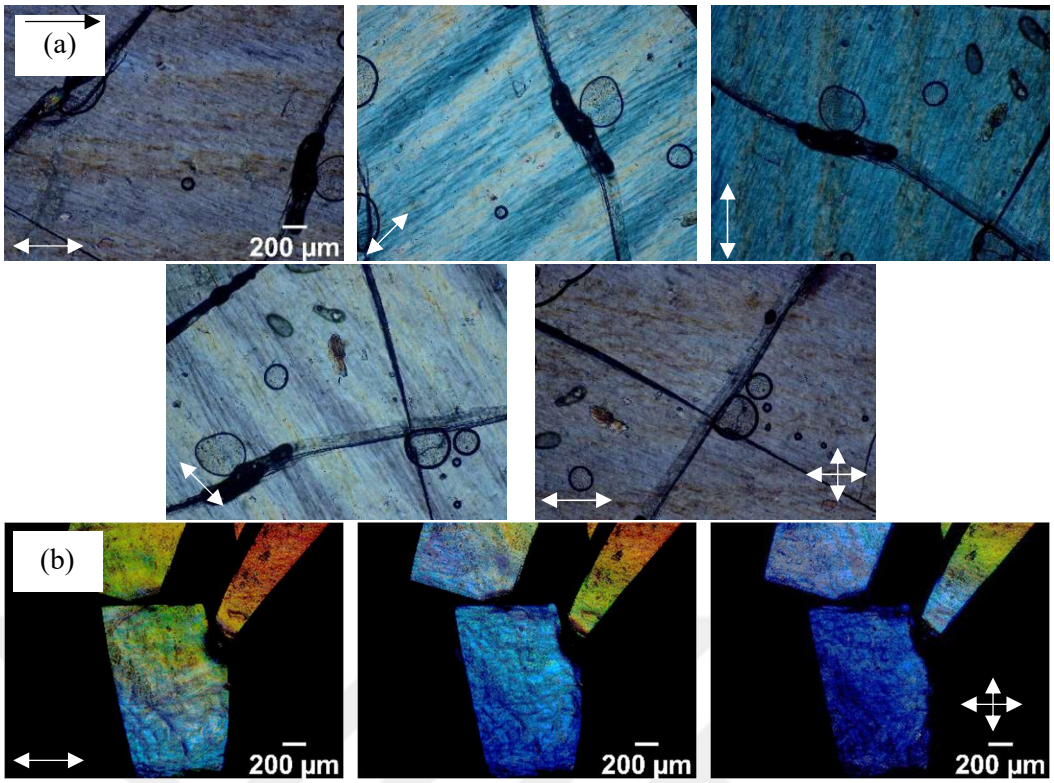

Figure 3-29. Polarized optical images of the sample with 0.30% TEMPO-CNC and 10 mM NaCl. (a)Transmission images of the wet sample (b) Reflection images of the sample during drying. Black arrow shows the direction of flow during the deposition. Single white arrows show the sample position according to the analyzer. Cross white arrows show the direction of analyzer and polarizer.

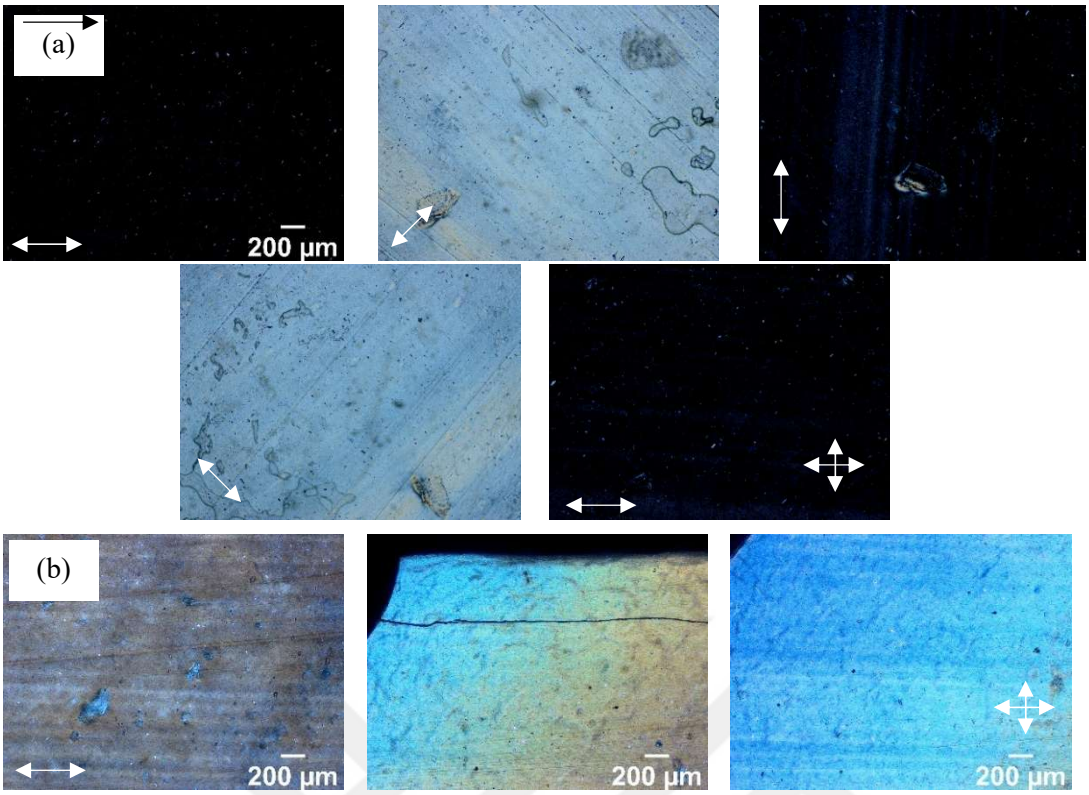

Figure 3-30. Polarized optical images of the second sample with 0.30% TEMPO-CNC and 10 mM NaCl. (a) Transmission images of the wet sample (b) Reflection images of the sample during drying. Black arrow shows the direction of flow during the deposition. Single white arrows show the sample position according to the analyzer. Cross white arrows show the direction of analyzer and polarizer.

In the transmission images of the sample prepared with 0.30% TEMPO-CNC with 100 mM NaCl, a slight intensity increase at 45° and 135° was observed as seen in Figure 3-31. It means that nematic structure exists in the TEMPO-CNC layer. But it is not wrong to say that the dominant one is cholesteric structure since the blue shift due to Bragg reflection was obviously seen in the reflection images of the drying sample in Figure 3-31 (b). This clear blue shift with the vibrant colors of the visible range indicates the significant amount of TEMPO-CNCs having the cholesteric structure. Additionally, the bright and shiny appearance of the TEMPO-CNC aggregates was observed in the POM images of the sample prepared with 100 mM NaCl and 0.30% TEMPO-CNC as marked with red circles in Figure 3-31. This observation was expected and indeed seen in the ones prepared with other TEMPO-CNC feed suspensions with 100 mM salt in it as mentioned before. To sum up, the sample

prepared with 0.30% TEMPO-CNC and 100 mM NaCl showed both nematic and cholesteric ordering but the dominant one was the cholesteric one.

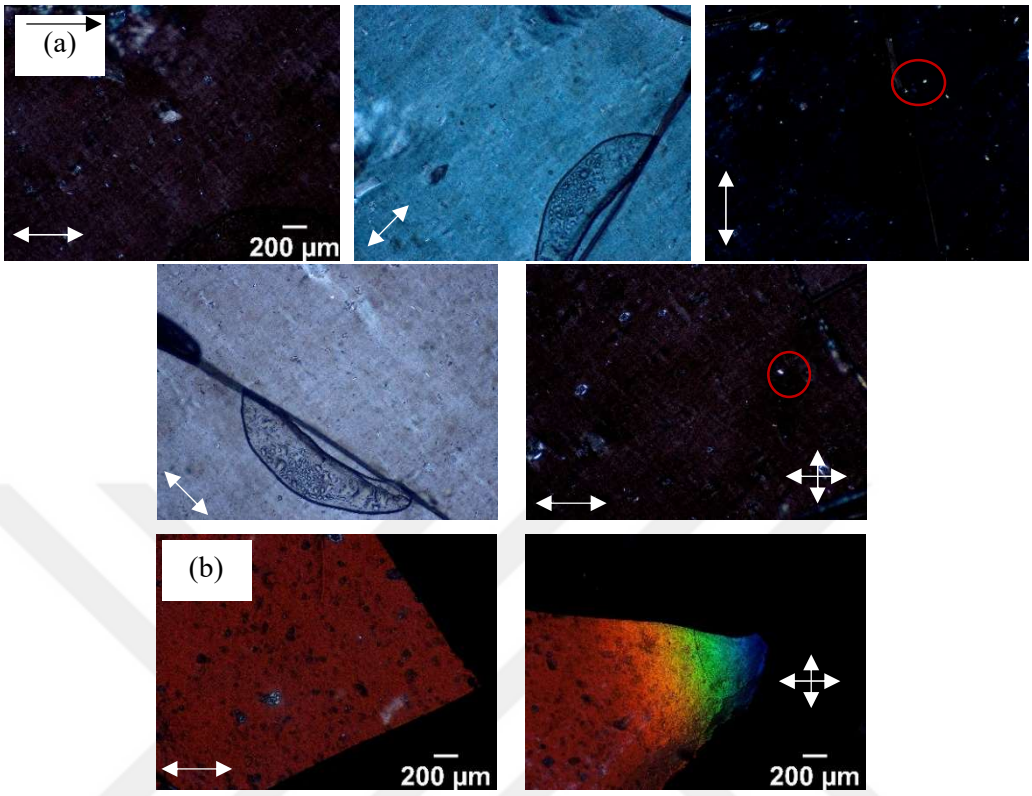

Figure 3-31. Polarized optical images of the sample with 0.30% TEMPO-CNC and 100 mM NaCl. (a)Transmission images of the wet sample (b) Reflection images of the sample during drying. Single white arrow shows the sample position according to the analyzer. Cross white arrows show the direction of analyzer and polarizer. Red circles show some of the aggregates.

To conclude, some of the samples showed both cholesteric and nematic optical behaviors while some of them only showed cholesteric phase behavior. The observed phases for the aforementioned samples can be seen in the phase diagram given in Figure 3-32. Even though a simple and obvious trend was not seen from the phase diagram, it might be possible to draw conclusions. For instance, the lowest and highest salt concentrations, 0 mM and 100 mM, generally resulted in a dominant and significant cholesteric structure in the TEMPO-CNC deposits prepared with the deposition of 0.075% and 0.15% TEMPO-CNC suspensions. Moreover, hybrid behavior, which was defined as the presence of both nematic and cholesteric structure, was generally observed at intermediate salt concentrations: 5 and 10 mM of NaCl for the suspensions of 0.075% and 0.15% TEMPO-CNC. For the TEMPO-CNC

suspensions of 0.30%, all NaCl concentrations resulted in hybrid behavior. Last but not the least, it was seen that the deposition of all TEMPO-CNC suspensions with various TEMPO-CNC and NaCl contents yielded a cholesteric structure in all TEMPO-CNC cake layers.

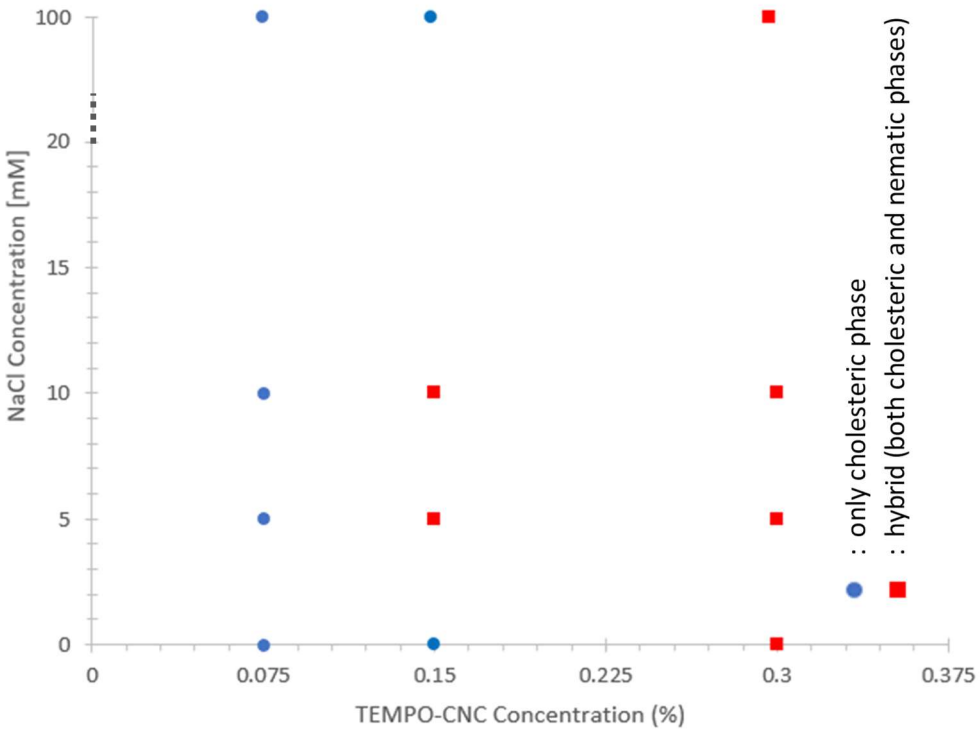

Figure 3-32. Summarized phase diagram for the samples prepared with the deposition of different TEMPO-CNC and NaCl suspensions

3.4 Salt Effect on the Resistances

For the salt effect investigation on the prepared samples characteristics, TEMPO-CNC layer resistances were calculated using Darcy's Law and resistances in series model. To see the effect of $AlCl_3$ permeation, resistances were calculated twice: before the $AlCl_3$ permeation and after the $AlCl_3$ filtration. The TEMPO-CNC gel layer thicknesses were measured from the SEM images of the cross sections of the samples and utilized for the calculation of specific TEMPO-CNC layer resistances. Specific resistances were calculated by dividing the resistance by the cross-sectional thickness of the deposit.

As seen in Figure 3-33 (a), TEMPO-CNC layer resistances of the samples prepared with 0.075% TEMPO-CNC with different NaCl contents were almost same after the $AlCl_3$ treatment. In a previous study by our group, it was seen that CNC cake layers' resistances prepared with the crossflow filtration of CNC suspensions significantly increased after the $AlCl_3$ permeation (Kocaman, 2022). It should be noted that the CNC suspensions were also synthesized with the sulfuric acid hydrolysis in that study. Therefore, CNCs have negatively charged sulfate groups that contribute to the electrostatic repulsion on the crystal surface (Habibi et al., 2010). Zeta potential of TEMPO-CNC suspensions was found to be (-59.5±1.69 mV) in a previous study (İçten, 2023). For the CNC suspensions synthesized by sulfuric acid hydrolysis having a concentration between 0.4% - 0.8%, the zeta potentials were reported around -25 mV (Zhang et al., 2021). In addition, the total charges of TEMPO-CNC and unmodified CNC were compared with conductometric titration in a previous study done by our group. The sulfate half-ester groups' concentration was found to be 390 ± 30 mmol/kg CNC for the unmodified CNC. On the other hand, the concentration of sulfate half-ester groups in TEMPO-CNC was found as 388 ± 8 mmol/kg CNC while the concentration of carboxyl groups was found to be 500 ± 40 mmol/kg CNC (İçten et al., 2024). As seen, the total net charge of TEMPO-CNC is more than twice the net charge of unmodified CNC due to the addition of carboxyl groups by TEMPO-oxidation. Hence, this difference in total charge might lead to difference in the resistances of TEMPO-CNC and CNC cakes after $AlCl_3$ treatment. Being less negatively charged might allow CNCs to have more decreased resistances after $AlCl_3$ treatment.

Specific resistances of the samples prepared with 0, 5 and 10 mM are close to each other by considering the error range. Sample with 100 mM NaCl has much lower specific resistance than the others. This may be the result of the aggregates formed in the concentration polarization layer or in the bulk during the deposition. The presence of aggregates was also detected in some POM images, as given and discussed previously. There might be less densely packed regions between these aggregates. Thus, these regions might have lower resistances which decreases the overall specific resistance of the deposit layer. Deposit layers prepared with 0 and 10 mM NaCl had

similar specific resistances, and the layer prepared with 10 mM NaCl had the highest specific resistance.

As seen in Figure 3-33 (b), resistances were increased after the $AlCl_3$ treatment for the samples prepared with 0.15% TEMPO-CNC suspension with 0 and 10 mM NaCl. For the sample prepared with 5 mM salt, $AlCl_3$ permeation does not change the layer resistance significantly. On the other hand, it decreased the layer resistance significantly for the sample prepared with 100 mM NaCl. This can be due to the partial detachment of the gel layer from the surface due to the instant transmembrane pressure change at the beginning of the $AlCl_3$ permeation. When the specific resistances were examined, it was observed that the sample with 100 mM NaCl have the lowest resistance among the others. Samples prepared with 10 mM NaCl had higher specific resistances than the ones prepared without salt, and the samples prepared with 5 mM NaCl had the highest specific resistance. Similarly, it was also the case for the deposit layers prepared with 0.075% TEMPO-CNC as previously mentioned and shown in Figure 3-33 (a). Addition of NaCl salt up to 5 mM increased the specific layer resistance and further addition resulted in lower specific layer resistance.

Samples prepared with 0.30% TEMPO-CNC and different NaCl concentrations were investigated according to their layer resistances. As seen in Figure 3-33 (c), $AlCl_3$ permeation resulted in a slight increase in the layer resistances of the samples with 0 and 10 mM NaCl. For the one with 5 mM, it did not have a remarkable impact on the resistance. Finally, in the one with 100 mM NaCl, the layer resistance remained almost the same after the salt permeation.

Figure 3-33 (c) shows that the specific resistances are almost same for the deposit layers prepared with the deposition of 0.30% TEMPO-CNC with 0 and 5 mM NaCl. For the 10 mM NaCl, the specific resistance was approximately the same with 0 and 5 mM NaCl within the error range. Specific resistance slightly increased with the addition of 100 mM salt.

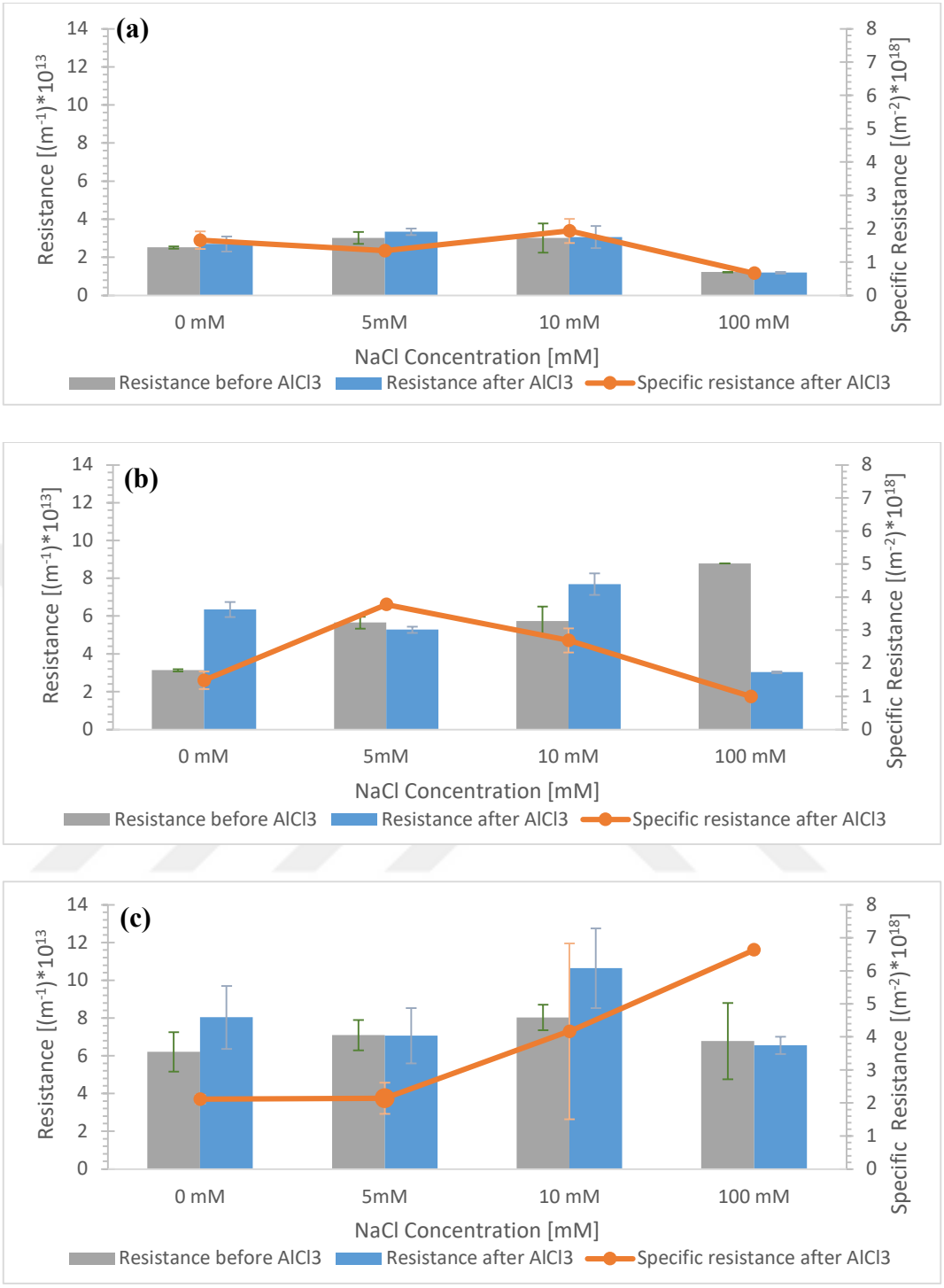

Figure 3-33. Plot of resistances before and after the $AlCl_3$ permeation together with the specific resistances for the deposit layers prepared with (a) 0.075% (b) 0.15% (c) 0.30% TEMPO-CNC suspensions with different NaCl concentrations

3.5 Salt Effect on the Limiting Flux and Gel Concentration

In order to predict the gel concentration of the deposit layers, Equation 7 was utilized. Because it was considered that the slow decline after the initial steep decline related to a rearrangement in the TEMPO-CNC layer, flux at the intersection of the two regions is taken as the limiting flux. This procedure was repeated for all samples, and a representative one was provided in Appendix C. After the limiting flux estimations, limiting fluxes were plotted against the natural logarithmic values of the bulk TEMPO-CNC concentration. This data was fitted to linear equations as seen in Figure 3-34.

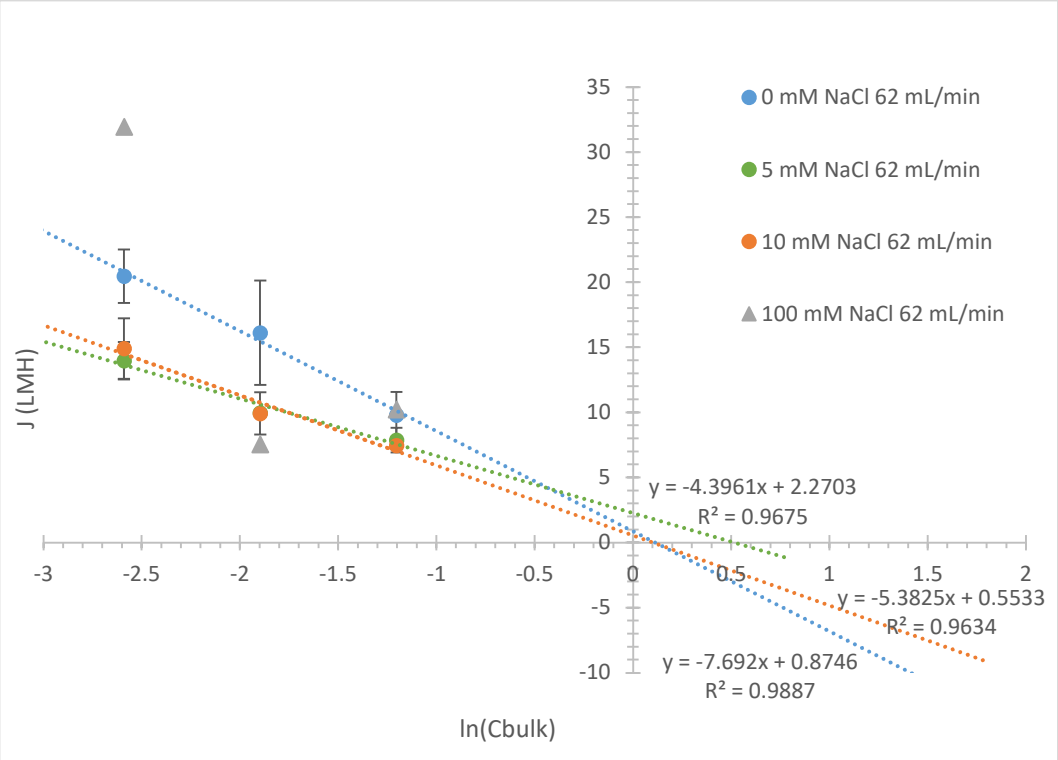

Figure 3-34. Plot of limiting flux vs ln(C_{bulk}) for the determination of gel concentrations of the prepared membranes

For the membranes prepared with TEMPO-CNC suspensions with 0, 5 and 10 mM NaCl, the data fits the linear model quite well. Additionally, 5 and 10 mM NaCl lines have similar magnitudes of slopes and x-axis-cross-sections, which represent convective mass transfer coefficient, k_c and gel concentration, respectively. The fitted line of 0 mM NaCl has slightly higher slope than the others. The linear regression for the membranes with 100 mM NaCl was not quite good. Thus, its data was not fit a

linear line in the plot. The reason might be the presence of aggregates and the high anisotropy in the system. The x-axis cross-sections of these linear lines are remarkably important since they are the natural logarithmic values of gel concentrations. The estimated gel concentrations from the x-axis-cross-sections are tabulated in Table 3-1 for different salt contents. A previous study showed that the gel concentration was estimated as 5.9% for the deposition of 0.30% CNC with different feed flowrates by using gel-polarization model (Kocaman, 2022)(Kocaman, 2022)(Kocaman, 2022)(Kocaman, 2022). The estimated values are much lower than 5.9%, as seen in Table 3-1. It should be noted that CNCs synthesized with sulfuric acid hydrolysis also have negative charge. However, it is possible that the gel concentration estimation might include not only the gel layer itself but also the concentration polarization layer. Furthermore, it is known that the concentration should be decreasing while going from the deposited gel layer to the bulk. As previously mentioned, conductometric titration and zeta potential measurements in the literature showed that total net charge of TEMPO-CNC is much higher than CNC (İçten et al., 2024; Zhang et al., 2021). Higher net total charge may result in higher resistance in the concentration polarization layer for TEMPO-CNC. Thus, estimated concentration may be the combined concentration of gel layer and concentration polarization layer with higher resistance, and this can explain finding a lower concentration value for TEMPO-CNC than the obtained one for CNC in literature.

Table 3-1. Predicted concentrations of TEMPO-CNC gels for different salt concentrations

NaCl Concentration [mM]	**Gel Concentration (%)**
0	1.12
5	1.68
10	1.11

The predicted gel concentrations of the deposit layers are around 1% as seen in Table 3-1. Also, rheological analysis was made to see whether this result is logical. For that analysis, TEMPO-CNC suspensions with different TEMPO-CNC and salt concentrations were prepared. The result of this rheological analysis was given in Figure 3-35.

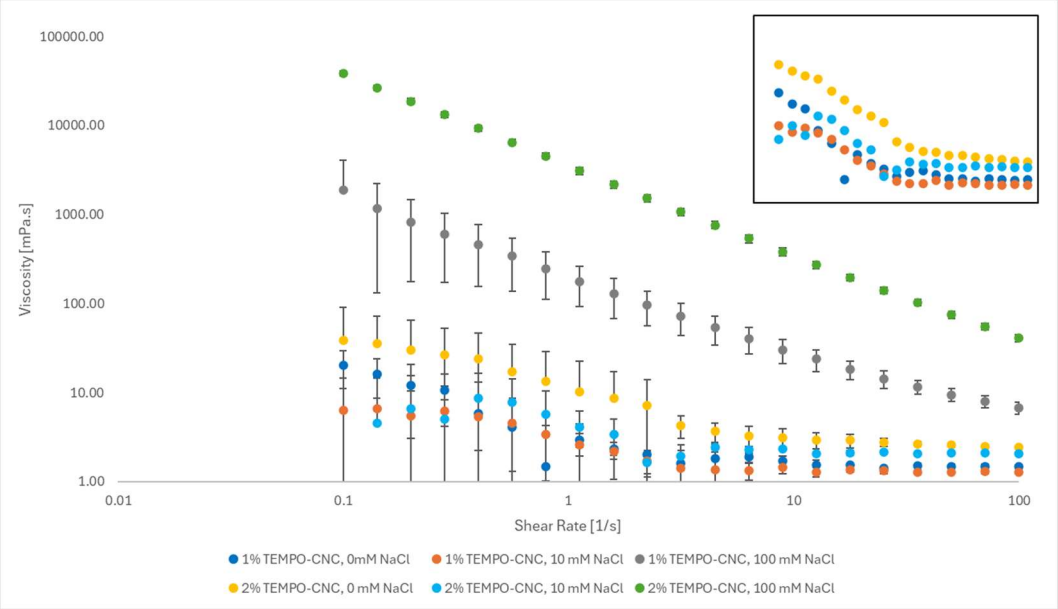

Figure 3-35. Steady shear viscosities of TEMPO-CNC suspensions with and without salt

As seen in Figure 3-35, three-region behavior was observed in the suspensions of 1% TEMPO-CNC without salt (dark blue), with 10 mM salt (orange) and 2% TEMPO-CNC without salt (yellow), with 10 mM salt (light blue). This presence of three-region behavior in the steady shear viscosities concludes that these suspensions are anisotropic. As stated earlier, steady shear viscosity of isotropic suspensions remains almost constant for low and high shear rates. The shear viscosities of the samples with 1% (grey) and 2% (green) TEMPO-CNC with 100 mM NaCl showed shear-thinning behavior at entire range of shear rates, which means complete gelation has occurred for these samples. Samples prepared with the deposition of TEMPO-CNC suspensions with 0, 5 and 10 mM NaCl were estimated to have gel concentrations between 1% and 2%, as provided in Table 3-1. Thus, this estimation was in line with the results obtained with rheological analysis since these suspensions should be anisotropic.

3.6 Estimation of Wet and Dried Solid Content for the Deposit Layers

For further investigation of the TEMPO-CNC deposit layers' structures, wet and dried solid contents were measured by TGA. A representative TGA plot for one of the samples was provided in Appendix D. Additionally, the dried layers' porosity values were calculated with Kozeny-Carman. Although these two analyses were based on different properties, that is volume for Kozeny-Carman, and weight for TGA, their results might be useful for comparison after the necessary conversion. Volume based solid contents calculated with Kozeny-Carman were converted to weight based solid contents. This conversion can be seen in Appendix E for one of the samples. The obtained results of the analyses were provided in Figure 3-36, Figure 3-37 and Figure 3-38.

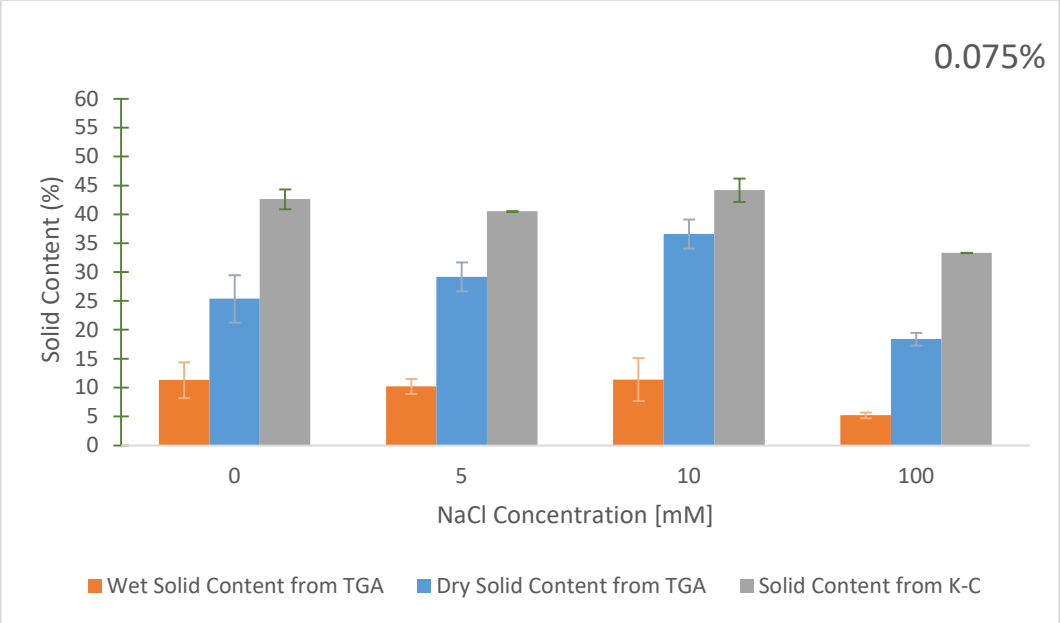

Figure 3-36. Solid contents from K-C and TGA for the samples prepared by 0.075% TEMPO-CNC and various salt contents

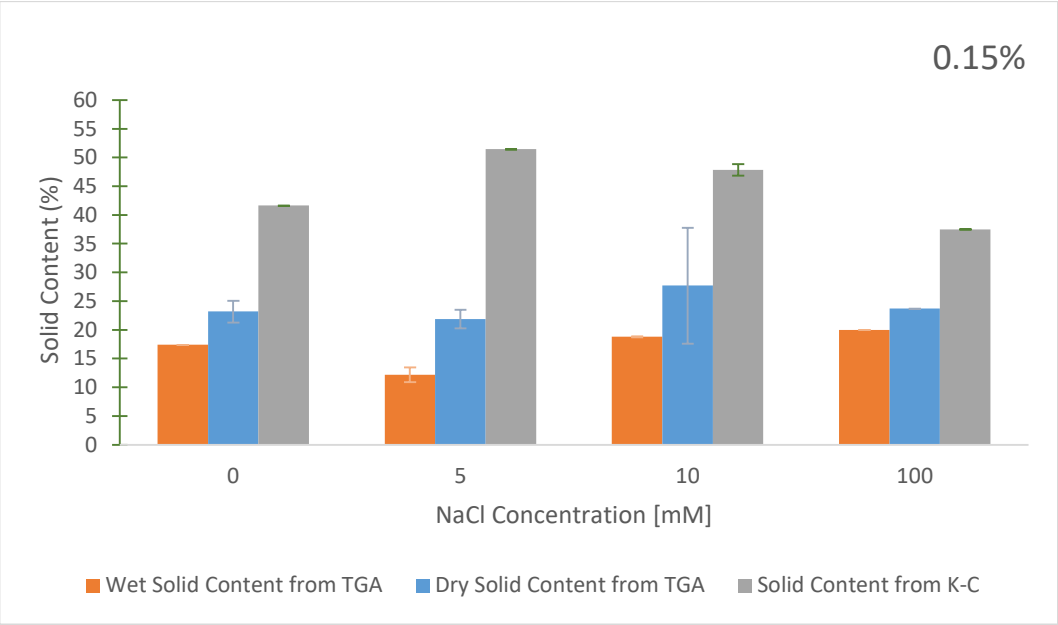

Figure 3-37. Solid contents from K-C and TGA for the samples prepared by 0.15% TEMPO-CNC and various salt contents

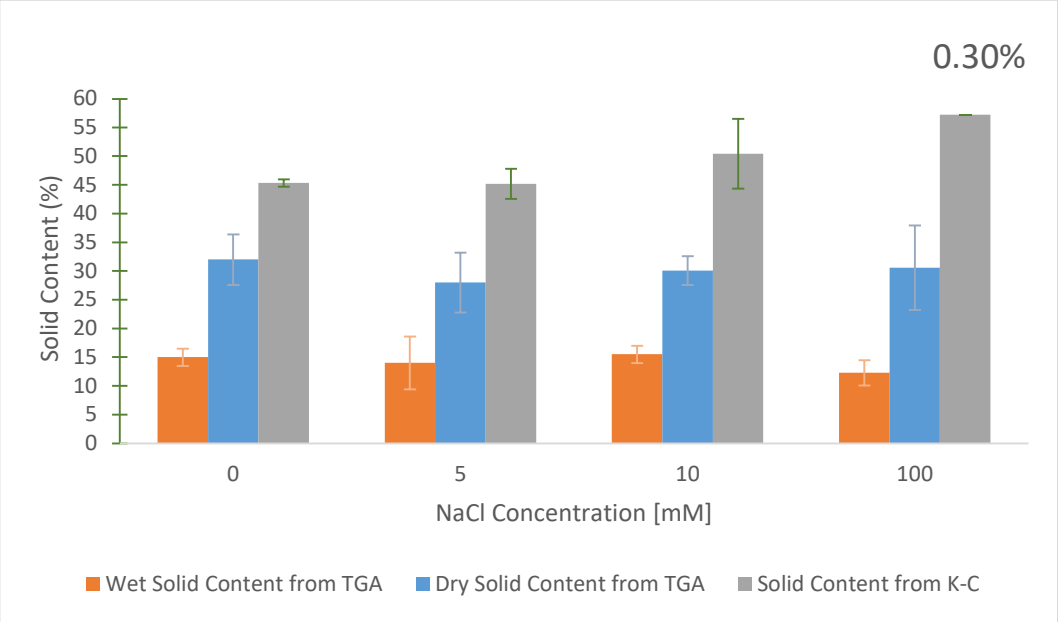

Figure 3-38. Solid contents from K-C and TGA for the samples prepared by 0.30% TEMPO-CNC and various salt contents

The wet and dry solid contents of the TEMPO-CNC deposits were compared to understand the effect of drying on the shrinkage of pores in the structure. Expectedly, the solid contents became higher when the deposit layers were dried as can be concluded from Figure 3-36, Figure 3-37 and Figure 3-38. This increase in solid

contents is due to the collapse of the pores in the TEMPO-CNC cake layers during drying. As previously explained, the gel concentrations of the deposit layers were calculated by utilizing the limiting fluxes of TEMPO-CNCs' crossflow filtrations and these concentrations were around 1% as tabulated in Table 3-1. When the wet solid contents of the samples were examined by looking at Figure 3-36, Figure 3-37 and Figure 3-38, it was seen that they are much higher than 1%. The main reason of this difference is the impact of $AlCl_3$ permeation on the porosity of deposit layers. Moreover, $AlCl_3$ permeation induces a decline in the porosity of cakes. As shown in 3.4, $AlCl_3$ permeation did not result in a significant increase in cake layer resistances even though it induced a significant increase in solid content. A possible explanation of this behavior could be that the calculated resistance before $AlCl_3$ permeation is not of solely the cake layer but is a combination of the cake and concentration polarization layers. In fact, previous studies showed the presence of this concentration polarization layer in the crossflow filtration of CNC by observing the velocity and concentration profiles during the filtration. That study showed that there was a highly concentrated layer next to the fouling layer and the velocity was low in that layer due to high concentration (Rey et al., 2019). Since the concentration polarization layer brings additional resistance, the resistances calculated before the $AlCl_3$ permeation might be due to both the gel layer and the concentration polarization layer. After the TEMPO-CNC deposition, the concentration polarization layer and its additional resistance were no longer existent and the calculated resistances after $AlCl_3$ permeation only correspond to the resistances of gel layer. Therefore, an expected increase in cake resistance after $AlCl_3$ permeation was not observed while the decrease in cake porosity after $AlCl_3$ permeation was seen from the estimated solid contents.

These studies showed that crossflow filtration of TEMPO-CNC results in formation of cake layer onto porous support membrane. It was seen that the formation and structure of the cake layers were dependent on the deposition duration. As the deposition proceeds, the layer appears to organize into a more cholesteric order. $AlCl_3$ permeation induced higher solid contents of the cakes whereas it did not increase the cake resistance. The estimated resistances before the salt permeation might be the combined resistances of cake and concentration polarization layers. The deposition duration also

affected the TEMPO-CNC ordering as evidenced from the optical properties of the cake layers. Longer depositions of 0.30% TEMPO-CNC with 5 mM NaCl suspensions led both cholesteric and nematic optical behaviors observed under POM. However, the samples prepared with shorter depositions showed only nematic symmetry under POM. The explanation of this observation may be that longer depositions can allow deposit layers to reorganize. The structure and characteristics of the deposit layers were also affected by the NaCl content. 100 mM NaCl addition to suspensions resulted in formation of TEMPO-CNC aggregates which were visible on the cake layer surface under POM. Cake layers prepared with 0.075%, 0.15% and 0.30% TEMPO-CNC with 5 mM NaCl showed both cholesteric and nematic behaviors. Lower and higher salt contents induced more dominant cholesteric structure in the deposit layers. The concentration of gel layers prepared with different salt contents were estimated around 1% by utilizing the permeate fluxes. However, it was thought that this estimated gel layer concentration was not solely for the gel layer but also for the concentration polarization layer. Solid contents of the cake layers estimated from Kozeny-Carman equation and TGA were higher which can also support the previous argument related to combined gel concentration estimation.

CHAPTER 4

CONCLUSION

In this study, it was aimed to investigate cake layer formation of TEMPO-CNC and the impacts of salt content, TEMPO-CNC concentration and deposition duration on the structure of deposit layers. To achieve this goal, TEMPO-CNCs that were obtained by TEMPO-oxidation of CNCs synthesized via sulfuric acid hydrolysis were deposited onto porous support with crossflow membrane filtration. The formed TEMPO-CNC cakes were stabilized with the permeation of 0.2 M $AlCl_3$ solution which induces irreversible coagulation and excess salt was washed with ultrapure water afterwards. Then, formed cakes were investigated in terms of flux performance, resistance, optical behaviors and solid content. For these investigations, POM, SEM and TGA were utilized.

The results showed a strong dependence on the duration of deposition for the formation and structure of the cake layers where flux decreases as the deposition continues. The decrease in the flux starts rapidly but proceeds in a decelerating manner. In the end, it becomes steady. Similarly, the cake resistance starts with a sudden increase at first and slows down as the deposition proceeds. No significant change in the deposit layer thickness and specific layer resistance was observed with increasing deposition durations. However, a significant difference in morphologies was seen in the SEM images of the samples prepared with the shortest and longest depositions. The sample with the longest deposition showed more layered and periodical structure which indicates the presence of more dominant cholesteric ordering in the cake layer.

The concentration of gel layers prepared with different salt contents were estimated to be around 1% by utilizing the permeate fluxes which was also supported by the rheological analysis. Solid contents of the cake layers estimated from Kozeny-Carman and TGA were higher due to the $AlCl_3$ permeation. The solid contents obtained with TGA were increased after drying due to collapse of the pores in the TEMPO-CNC deposit layer structure. It was observed that $AlCl_3$ permeation did not increase cake

resistance, however, it induced higher solid contents of the cakes. The estimated resistance before the salt permeation was assigned to the sum of resistances of cake and concentration polarization layers. Since TEMPO-CNCs are highly negatively charged, there exists a concentration polarization layer with high resistance during the filtration. After the salt permeation, this extra layer and its resistance was not present anymore. This extra resistance came from the concentration polarization layer resulted in high resistance before the salt permeation. Thus, an expected increase in the resistances after $AlCl_3$ permeation cannot be seen while the decrease in layer porosities was successfully observed.

Besides, it was understood that optical properties of the TEMPO-CNC cake layers are affected by the duration of the deposition as it was observed under POM that longer depositions of 0.30% TEMPO-CNC with 5 mM NaCl suspensions resulted in cholesteric and nematic optical symmetry whereas shorter depositions showed only nematic symmetry. This may be explained by the fact that deposit layers have more time to be reorganized at longer depositions since the layers are compressible gels which allows a reorganization to occur during the deposition. As the filtration proceeded, the deposits became denser and more compact, which can induce the observed phase transition in TEMPO-CNCs. Moreover, it was seen that both applied shear and the TEMPO-CNC deposition affected the final structure of the TEMPO-CNC deposits. On top of that, NaCl content also affects the structure and characteristics of the deposit layers. As observed under POM, TEMPO-CNC aggregates were formed on the cake layer surface with the addition of 100 mM NaCl to the suspensions. Cake layers prepared with 0.075%, 0.15% and 0.30% TEMPO-CNC with 5 and 10 mM NaCl generally showed both cholesteric and nematic symmetries while 0 and 100 mM NaCl generally yielded more dominant cholesteric ordering in the structures. The samples prepared with filtration of 0.30% TEMPO-CNC suspensions with different NaCl concentrations showed hybrid behavior where both cholesteric and nematic symmetries were present. On the other hand, samples prepared with 0.075% TEMPO-CNC suspensions showed more dominant cholesteric structure.

This study showed the dependence of final TEMPO-CNC cake layer structure to TEMPO-CNC concentration, NaCl concentration and TEMPO-CNC deposition duration. Moreover, it also showed that not only the deposition duration but also the shear impacted the final structures of cake layers. It provided information about the TEMPO-CNC cake layer formation and the factors that were affecting the structure, morphology and phase of the deposit layers.

REFERENCES

Abbasi Moud, A. (2022). Chiral Liquid Crystalline Properties of Cellulose Nanocrystals: Fundamentals and Applications. *ACS Omega*, *7*(35), 30673–30699. https://doi.org/10.1021/ACSOMEGA.2C03311/ASSET/IMAGES/LARGE/AO2C03311_0006.JPEG

Aliasghari Aghdam, M., Mirsaeedghazi, H., Aboonajmi, M., & Kianmehr, M. H. (2015). Effect of ultrasound on different mechanisms of fouling during membrane clarification of pomegranate juice. *Innovative Food Science & Emerging Technologies*, *30*, 127–131. https://doi.org/10.1016/J.IFSET.2015.05.008

Al-Najar, B., Peters, C. D., Albuflasa, H., & Hankins, N. P. (2020). Pressure and osmotically driven membrane processes: A review of the benefits and production of nano-enhanced membranes for desalination. *Desalination*, *479*, 114323. https://doi.org/10.1016/J.DESAL.2020.114323

Baker, R. W. (2012). Membrane Technology and Applications. *Membrane Technology and Applications*. https://doi.org/10.1002/9781118359686

Belfort, G., Davis, R. H., & Zydney, A. L. (1994). The behavior of suspensions and macromolecular solutions in crossflow microfiltration. *Journal of Membrane Science*, *96*(1–2), 1–58. https://doi.org/10.1016/0376-7388(94)00119-7

Blanpain-Avet, P., Migdal, J. F., & Bénézech, T. (2009). Chemical cleaning of a tubular ceramic microfiltration membrane fouled with a whey protein concentrate suspension-Characterization of hydraulic and chemical cleanliness. *Journal of Membrane Science*, *337*(1–2), 153–174. https://doi.org/10.1016/J.MEMSCI.2009.03.033

Cao, T., & Elimelech, M. (2021). Colloidal stability of cellulose nanocrystals in aqueous solutions containing monovalent, divalent, and trivalent inorganic salts.

Journal of Colloid and Interface Science, *584*, 456–463. https://doi.org/10.1016/J.JCIS.2020.09.117

Carman, P. G. (1997). Fluid flow through granular beds. *Chemical Engineering Research and Design*, *75*(1 SUPPL.), S32–S48. https://doi.org/10.1016/S0263-8762(97)80003-2

Chang, M. H., & Oh-e, M. (2022). Kinetic arrest during the drying of cellulose nanocrystal films from aqueous suspensions analogous to the freezing of thermal motions. *Scientific Reports 2022 12:1*, *12*(1), 1–12. https://doi.org/10.1038/s41598-022-24926-8

Cranston, E. D., & Gray, D. G. (2008). Birefringence in spin-coated films containing cellulose nanocrystals. *Colloids and Surfaces A: Physicochemical and Engineering Aspects*, *325*(1–2), 44–51. https://doi.org/10.1016/J.COLSURFA.2008.04.042

Dumanli, A. G., Van Der Kooij, H. M., Kamita, G., Reisner, E., Baumberg, J. J., Steiner, U., & Vignolini, S. (2014). Digital Color in Cellulose Nanocrystal Films. *ACS Applied Materials & Interfaces*, *6*(15), 12302. https://doi.org/10.1021/AM501995E

Duzik, A., Ko, H.-U., Kim, H.-J., Kim, J., Kim, J. H., Choi, S. H., & Bryant, R. G. (2019). *Fabrication Method, Characteristics and Applications of Cellulose Nano Fiber (CNF) Film*.

Espinha, A., Guidetti, G., Serrano, M. C., Frka-Petesic, B., Dumanli, A. G., Hamad, W. Y., Blanco, Á., López, C., & Vignolini, S. (2016). Shape memory cellulose-based photonic reflectors. *ACS Applied Materials and Interfaces*, *8*(46), 31935–31940. https://doi.org/10.1021/ACSAMI.6B10611/ASSET/IMAGES/LARGE/AM-2016-10611K_0005.JPEG

Frka-Petesic, B., Kamita, G., Guidetti, G., & Vignolini, S. (2019). Angular optical response of cellulose nanocrystal films explained by the distortion of the arrested suspension upon drying. *Physical Review Materials*, *3*(4), 045601.

https://doi.org/10.1103/PHYSREVMATERIALS.3.045601/FIGURES/21/THUMBNAIL

Frka-Petesic, B., Parton, T. G., Honorato-Rios, C., Narkevicius, A., Ballu, K., Shen, Q., Lu, Z., Ogawa, Y., Haataja, J. S., Droguet, B. E., Parker, R. M., & Vignolini, S. (2023). Structural Color from Cellulose Nanocrystals or Chitin Nanocrystals: Self-Assembly, Optics, and Applications. *Chemical Reviews*, *123*(23), 12595–12756. https://doi.org/10.1021/ACS.CHEMREV.2C00836/ASSET/IMAGES/LARGE/CR2C00836_0046.JPEG

Geng, Y., Honorato-Rios, C., Noh, J. H., & Lagerwall, J. P. F. (2024a). Cholesteric Spherical Reflectors with Tunable Color from Single-Domain Cellulose Nanocrystal Microshells. *Advanced Materials*, *36*(8), 2305251. https://doi.org/10.1002/ADMA.202305251;WEBSITE:WEBSITE:ADVANCED;CTYPE:STRING:JOURNAL

Geng, Y., Honorato-Rios, C., Noh, J. H., & Lagerwall, J. P. F. (2024b). Cholesteric Spherical Reflectors with Tunable Color from Single-Domain Cellulose Nanocrystal Microshells. *Advanced Materials*, *36*(8), 2305251. https://doi.org/10.1002/ADMA.202305251;WEBSITE:WEBSITE:ADVANCED;CTYPE:STRING:JOURNAL

Gul, A., Hruza, J., & Yalcinkaya, F. (2021). Fouling and Chemical Cleaning of Microfiltration Membranes: A Mini-Review. *Polymers 2021, Vol. 13, Page 846*, *13*(6), 846. https://doi.org/10.3390/POLYM13060846

Habibi, Y., Lucia, L. A., & Rojas, O. J. (2010). Cellulose nanocrystals: Chemistry, self-assembly, and applications. *Chemical Reviews*, *110*(6), 3479–3500. https://doi.org/10.1021/CR900339W,

Hadi, M. K., Wang, X., Peng, Y., Sangaraju, S., & Ran, F. (2024). Functional Polymeric Membrane Materials: A Perspective from Versatile Methods and Modification to Potential Applications. *Polymer Science & Technology*. https://doi.org/10.1021/POLYMSCITECH.4C00030

Hengl, N., Jin, Y., Pignon, F., Baup, S., Mollard, R., Gondrexon, N., Magnin, A., Michot, L., & Paineau, E. (2014). A new way to apply ultrasound in cross-flow ultrafiltration: Application to colloidal suspensions. *Ultrasonics Sonochemistry*, *21*(3), 1018–1025. https://doi.org/10.1016/J.ULTSONCH.2013.11.008

Hoeger, I., Rojas, O. J., Efimenko, K., Velev, O. D., & Kelley, S. S. (2011). Ultrathin film coatings of aligned cellulose nanocrystals from a convective-shear assembly system and their surface mechanical properties. *Soft Matter*, *7*(5), 1957–1967. https://doi.org/10.1039/C0SM01113D

Hongladarom, K., & Burghardt, W. R. (1993). Molecular Alignment of Polymer Liquid Crystals in Shear Flows. 2. Transient Flow Behavior in Poly(benzyl glutamate) Solutions. *Macromolecules*, *26*(4), 785–794. https://doi.org/10.1021/MA00056A033/ASSET/MA00056A033.FP.PNG_V03

İçten, B. C. (2023). *Membrane fabrication VIA shear induced deposition and chemical stabilization of cellulose nanocrystals*. https://open.metu.edu.tr/handle/11511/105298

İçten, B. C., Bukusoglu, E., & Çulfaz-Emecen, P. Z. (2024). Cross-Linked Cellulose Nanocrystal Membranes with Cholesteric Assembly. *Langmuir*, *40*(25), 13247–13255. https://doi.org/10.1021/ACS.LANGMUIR.4C01443/ASSET/IMAGES/LARGE/LA4C01443_0007.JPEG

Iritani, E., Hattori, K., & Murase, T. (1993). Analysis of dead-end ultrafiltration based on ultracentrifugation method. *Journal of Membrane Science*, *81*(1–2), 1–13. https://doi.org/10.1016/0376-7388(93)85026-S

Javadi, F. S., Saidur, R., & Kamalisarvestani, M. (2013). Investigating performance improvement of solar collectors by using nanofluids. *Renewable and Sustainable Energy Reviews*, *28*, 232–245. https://doi.org/10.1016/J.RSER.2013.06.053

Jin, Y., Hengl, N., Baup, S., Pignon, F., Gondrexon, N., Sztucki, M., Gésan-Guiziou, G., Magnin, A., Abyan, M., Karrouch, M., & Blésès, D. (2014). Effects of

ultrasound on cross-flow ultrafiltration of skim milk: Characterization from macro-scale to nano-scale. *Journal of Membrane Science*, *470*, 205–218. https://doi.org/10.1016/J.MEMSCI.2014.07.043

Jin, Y., Hengl, N., Baup, S., Pignon, F., Gondrexon, N., Sztucki, M., Romdhane, A., Guillet, A., & Aurousseau, M. (2015). Ultrasonic assisted cross-flow ultrafiltration of starch and cellulose nanocrystals suspensions: Characterization at multi-scales. *Carbohydrate Polymers*, *124*, 66–76. https://doi.org/10.1016/J.CARBPOL.2015.01.073

Jinkins, K. R., Wang, J., Dwyer, J. H., Wang, X., & Arnold, M. S. (2021). Confined Shear Alignment of Ultrathin Films of Cellulose Nanocrystals. *ACS Applied Bio Materials*, *4*(11), 7961–7966. https://doi.org/10.1021/ACSABM.1C00884,

Juárez-Rivera, O. R., Mauricio-Sánchez, R. A., Järrendahl, K., Arwin, H., & Mendoza-Galván, A. (2021). Shear-coated linear birefringent and chiral cellulose nanocrystal films prepared from non-sonicated suspensions with different storage time. *Nanomaterials*, *11*(9). https://doi.org/10.3390/NANO11092239,

Kádár, R., Spirk, S., & Nypelö, T. (2021). Cellulose Nanocrystal Liquid Crystal Phases: Progress and Challenges in Characterization Using Rheology Coupled to Optics, Scattering, and Spectroscopy. *ACS Nano*, *15*(5), 7931–7945. https://doi.org/10.1021/ACSNANO.0C09829/ASSET/IMAGES/LARGE/NN0C09829_0008.JPEG

Kocaman, C. (2022). *PROCESSING CELLULOSE NANOCRYSTAL SUSPENSIONS FOR ALIGNED DEPOSITION*. https://open.metu.edu.tr/handle/11511/97305

Kocaman, C., Bukusoglu, E., & Culfaz-Emecen, P. Z. (2021). Controlling Ultrafiltration Membrane Rejection via Shear-Aligned Deposition of Cellulose Nanocrystals from Aqueous Suspensions. *ACS Applied Materials and Interfaces*, *13*(30), 36548–36557. https://doi.org/10.1021/ACSAMI.1C09815/ASSET/IMAGES/LARGE/AM1C09815_0009.JPEG

Kocaman, C., Bukusoglu, E., & Çulfaz-Emecen, P. Z. (2022). Tuning electrostatic interactions for controlled structure and rejection of cellulose nanocrystal membranes. *Journal of Membrane Science*, *661*, 120932. https://doi.org/10.1016/J.MEMSCI.2022.120932

Kong, S., Zhao, C., Sun, Y., Huang, J., Zhang, L., Ru, Y., Zhou, H., Zhou, T., & Liu, M. (2024). Large-area, high-strength cellulose nanocomposites enhanced by confined polymer nanocrystallization in Bouligand structures. *Matter*, *7*(6), 2250–2264. https://doi.org/10.1016/J.MATT.2024.04.014

Lagerwall, J. P. F., Schütz, C., Salajkova, M., Noh, J., Park, J. H., Scalia, G., & Bergström, L. (2014). Cellulose nanocrystal-based materials: From liquid crystal self-assembly and glass formation to multifunctional thin films. *NPG Asia Materials*, *6*(1), e80–e80. https://doi.org/10.1038/AM.2013.69;SUBJMETA=119,301,357,544,639,919,923;KWRD=LIQUID+CRYSTALS,NANOSCALE+MATERIALS,SURFACES

Le Gars, M., Delvart, A., Roger, P., Belgacem, M. N., & Bras, J. (2020). Amidation of TEMPO-oxidized cellulose nanocrystals using aromatic aminated molecules. *Colloid and Polymer Science*, *298*(6), 603–617. https://doi.org/10.1007/S00396-020-04640-5/FIGURES/6

Lin, C., Chen, B., Liu, Y., Chen, Y., Liu, M., & Zhu, J. Y. (2021). Carboxylated cellulose nanocrystals with chiral nematic property from cotton by dicarboxylic acid hydrolysis. *Carbohydrate Polymers*, *264*, 118039. https://doi.org/10.1016/J.CARBPOL.2021.118039

Loeb, S., & Sourirajan, S. (1963). *Sea Water Demineralization by Means of an Osmotic Membrane*. 117–132. https://doi.org/10.1021/BA-1963-0038.CH009

Madaeni, S. S., Sharifnia, S., & Moradi, G. (2001). Chemical cleaning of microfiltration membranes fouled by whey. *Journal of the Chinese Chemical Society*, *48*(2), 179–191. https://doi.org/10.1002/JCCS.200100031

Mahlangu, T. O., Thwala, J. M., Mamba, B. B., D'Haese, A., & Verliefde, A. R. D. (2015). Factors governing combined fouling by organic and colloidal foulants in cross-flow nanofiltration. *Journal of Membrane Science*, *491*, 53–62. https://doi.org/10.1016/J.MEMSCI.2015.03.021

Mandin, S., Metilli, L., Karrouch, M., Bleses, D., Lancelon-Pin, C., Sailler, P., Chevremont, W., Paineau, E., Putaux, J. L., Hengl, N., Jean, B., & Pignon, F. (2024a). Multiscale study of the chiral self-assembly of cellulose nanocrystals during the frontal ultrafiltration process. *Nanoscale*, *16*(40), 19100–19115. https://doi.org/10.1039/D4NR02840F

Mandin, S., Metilli, L., Karrouch, M., Bleses, D., Lancelon-Pin, C., Sailler, P., Chevremont, W., Paineau, E., Putaux, J. L., Hengl, N., Jean, B., & Pignon, F. (2024b). Multiscale study of the chiral self-assembly of cellulose nanocrystals during the frontal ultrafiltration process. *Nanoscale*, *16*(40), 19100–19115. https://doi.org/10.1039/D4NR02840F

May, P., Laghmari, S., & Ulbricht, M. (2021). Concentration polarization enabled reactive coating of nanofiltration membranes with zwitterionic hydrogel. *Membranes*, *11*(3). https://doi.org/10.3390/MEMBRANES11030187,

Mitov, M. (2012). Cholesteric Liquid Crystals with a Broad Light Reflection Band. *Advanced Materials*, *24*(47), 6260–6276. https://doi.org/10.1002/ADMA.201202913

Motsa, M. M., Mamba, B. B., & Verliefde, A. R. D. (2018). Forward osmosis membrane performance during simulated wastewater reclamation: Fouling mechanisms and fouling layer properties. *Journal of Water Process Engineering*, *23*, 109–118. https://doi.org/10.1016/J.JWPE.2018.03.007

Mu, X., & Gray, D. G. (2014). Formation of chiral nematic films from cellulose nanocrystal suspensions is a two-stage process. *Langmuir*, *30*(31), 9256–9260. https://doi.org/10.1021/LA501741R/SUPPL_FILE/LA501741R_SI_001.PDF

Mulder, M. (1996). *Basic Principles of Membrane Technology*. https://doi.org/10.1007/978-94-009-1766-8

Niskanen, I., Suopajärvi, T., Liimatainen, H., Fabritius, T., Heikkilä, R., & Thungström, G. (2019). Determining the complex refractive index of cellulose nanocrystals by combination of Beer-Lambert and immersion matching methods. *Journal of Quantitative Spectroscopy and Radiative Transfer*, *235*, 1–6. https://doi.org/10.1016/J.JQSRT.2019.06.023

Nthunya, L. N., Bopape, M. F., Mahlangu, O. T., Mamba, B. B., Van der Bruggen, B., Quist-Jensen, C. A., & Richards, H. (2022). Fouling, performance and cost analysis of membrane-based water desalination technologies: A critical review. *Journal of Environmental Management*, *301*, 113922. https://doi.org/10.1016/J.JENVMAN.2021.113922

Palmer, J. M. ., & Grant, B. G. . (2010). *The art of radiometry*. 369. https://www.scribd.com/doc/214645223/The-Art-of-Radiometry-J-M-Palmer-B-G-Grant

Parker, R. M., Guidetti, G., Williams, C. A., Zhao, T., Narkevicius, A., Vignolini, S., & Frka-Petesic, B. (2018). The Self-Assembly of Cellulose Nanocrystals: Hierarchical Design of Visual Appearance. *Advanced Materials*, *30*(19). https://doi.org/10.1002/ADMA.201704477

Parton, T. G., Parker, R. M., van de Kerkhof, G. T., Narkevicius, A., Haataja, J. S., Frka-Petesic, B., & Vignolini, S. (2022a). Chiral self-assembly of cellulose nanocrystals is driven by crystallite bundles. *Nature Communications 2022 13:1*, *13*(1), 1–9. https://doi.org/10.1038/s41467-022-30226-6

Parton, T. G., Parker, R. M., van de Kerkhof, G. T., Narkevicius, A., Haataja, J. S., Frka-Petesic, B., & Vignolini, S. (2022b). Chiral self-assembly of cellulose nanocrystals is driven by crystallite bundles. *Nature Communications 2022 13:1*, *13*(1), 1–9. https://doi.org/10.1038/s41467-022-30226-6

Purkait, M. K., Sinha, M. K., Mondal, P., & Singh, R. (2018). Introduction to Membranes. *Interface Science and Technology*, *25*, 1–37. https://doi.org/10.1016/B978-0-12-813961-5.00001-2

Revol, J. F., Bradford, H., Giasson, J., Marchessault, R. H., & Gray, D. G. (1992). Helicoidal self-ordering of cellulose microfibrils in aqueous suspension. *International Journal of Biological Macromolecules*, *14*(3), 170–172. https://doi.org/10.1016/S0141-8130(05)80008-X

Rey, C., Hengl, N., Baup, S., Karrouch, M., Gicquel, E., Dufresne, A., Djeridi, H., Dattani, R., Jin, Y., & Pignon, F. (2019). Structure, Rheological Behavior, and in Situ Local Flow Fields of Cellulose Nanocrystal Dispersions during Cross-Flow Ultrafiltration. *ACS Sustainable Chemistry and Engineering*, *7*(12), 10679–10689. https://doi.org/10.1021/ACSSUSCHEMENG.9B01333/ASSET/IMAGES/LARGE/SC-2019-01333Y_0008.JPEG

Rodionova, G., Eriksen, Ø., & Gregersen, Ø. (2012). TEMPO-oxidized cellulose nanofiber films: Effect of surface morphology on water resistance. *Cellulose*, *19*(4), 1115–1123. https://doi.org/10.1007/S10570-012-9721-5

Sioutopoulos, D. C., & Karabelas, A. J. (2016). Evolution of organic gel fouling resistance in constant pressure and constant flux dead-end ultrafiltration: Differences and similarities. *Journal of Membrane Science*, *511*, 265–277. https://doi.org/10.1016/J.MEMSCI.2016.03.057

Sioutopoulos, D. C., Yiantsios, S. G., & Karabelas, A. J. (2010). Relation between fouling characteristics of RO and UF membranes in experiments with colloidal organic and inorganic species. *Journal of Membrane Science*, *350*(1–2), 62–82. https://doi.org/10.1016/J.MEMSCI.2009.12.012

Solhi, L., Guccini, V., Heise, K., Solala, I., Niinivaara, E., Xu, W., Mihhels, K., Kröger, M., Meng, Z., Wohlert, J., Tao, H., Cranston, E. D., & Kontturi, E. (2023). Understanding Nanocellulose-Water Interactions: Turning a Detriment into an Asset. *Chemical Reviews*, *123*(5), 1925–2015. https://doi.org/10.1021/ACS.CHEMREV.2C00611/ASSET/IMAGES/LARGE/CR2C00611_0029.JPEG

St. John, W. D., Fritz, W. J., Lu, Z. J., & Yang, D. K. (1995). Bragg reflection from cholesteric liquid crystals. *Physical Review E*, *51*(2), 1191. https://doi.org/10.1103/PhysRevE.51.1191

T. Ebeling, M. Paillet, R. Borsali, *, O. Diat, †, A. Dufresne, J-Y. Cavaillé, ‡ and, & Chanzy, H. (1999). *Shear-Induced Orientation Phenomena in Suspensions of Cellulose Microcrystals, Revealed by Small Angle X-ray Scattering*. https://doi.org/10.1021/LA990046+

Tatsumi, M., Kimura, F., Kimura, T., Teramoto, Y., & Nishio, Y. (2014). Anisotropic polymer composites synthesized by immobilizing cellulose nanocrystal suspensions specifically oriented under magnetic fields. *Biomacromolecules*, *15*(12), 4579–4589. https://doi.org/10.1021/BM501629G/ASSET/IMAGES/LARGE/BM-2014-01629G_0009.JPEG

Tayeh, Y. A., Alazaiza, M. Y. D., Alzghoul, T. M., & Bashir, M. J. (2025). A comprehensive review of RO membrane fouling: Mechanisms, categories, cleaning methods and pretreatment technologies. *Journal of Hazardous Materials Advances*, *18*, 100684. https://doi.org/10.1016/J.HAZADV.2025.100684

Thiruganasambanthan, T., Ilyas, R. A., Faiz Norrrahim, M. N., Muthu Kumar, T. S., Siengchin, S., Mohamad Misenan, M. S., Ahmad Farid, M. A., Mohd Nurazzi, N., Muhammad Asyraf, M. R., Syed Zakaria, S. Z., & Rizal Razman, M. (2022a). Emerging Developments on Nanocellulose as Liquid Crystals: A Biomimetic Approach. *Polymers*, *14*(8), 1546. https://doi.org/10.3390/POLYM14081546

Thiruganasambanthan, T., Ilyas, R. A., Faiz Norrrahim, M. N., Muthu Kumar, T. S., Siengchin, S., Mohamad Misenan, M. S., Ahmad Farid, M. A., Mohd Nurazzi, N., Muhammad Asyraf, M. R., Syed Zakaria, S. Z., & Rizal Razman, M. (2022b). Emerging Developments on Nanocellulose as Liquid Crystals: A Biomimetic Approach. *Polymers*, *14*(8), 1546. https://doi.org/10.3390/POLYM14081546

Volkan, E. (2020). *Membrane fabrication using nanocrystalline cellulose*. https://open.metu.edu.tr/handle/11511/69072

Wang, P. X., Hamad, W. Y., & MacLachlan, M. J. (2016). Structure and transformation of tactoids in cellulose nanocrystal suspensions. *Nature Communications*, *7*(1), 1–8. https://doi.org/10.1038/NCOMMS11515;TECHMETA=123;SUBJMETA=1002,119,301,357,440,638,639;KWRD=NANOSCALE+MATERIALS,PHYSICAL+CHEMISTRY,STRUCTURE+OF+SOLIDS+AND+LIQUIDS

Wang, X., Zhang, Z., & Zhang, Y. (2025). The Latest Applications of Cellulose Nanocrystals Liquid Crystal. *Crystal Research and Technology*. https://doi.org/10.1002/CRAT.70008

Xue, M. D., Kimura, T., Revol, J. F., & Gray, D. G. (1996). Effects of ionic strength on the isotropic-chiral nematic phase transition of suspensions of cellulose crystallites. *Langmuir*, *12*(8), 2076–2082. https://doi.org/10.1021/LA950133B/ASSET/IMAGES/LARGE/LA950133BF00012.JPEG

Yang, H., Yu, X., Liu, J., Tang, Z., Huang, T., Wang, Z., Zhong, Y., Long, Z., & Wang, L. (2022). A Concise Review of Theoretical Models and Numerical Simulations of Membrane Fouling. *Water 2022, Vol. 14, Page 3537*, *14*(21), 3537. https://doi.org/10.3390/W14213537

Zhang, H., Wu, Y., Yang, F., Dong, H., Bian, Y., Jia, H., Xie, X., & Zhang, J. (2021). Using Cellulose Nanocrystal as Adjuvant to Improve the Dispersion Ability of Multilayer Graphene in Aqueous Suspension. *Frontiers in Bioengineering and Biotechnology*, *9*, 638744. https://doi.org/10.3389/FBIOE.2021.638744

APPENDICES

A. Intensity Analysis of the POM Images with Gray Values

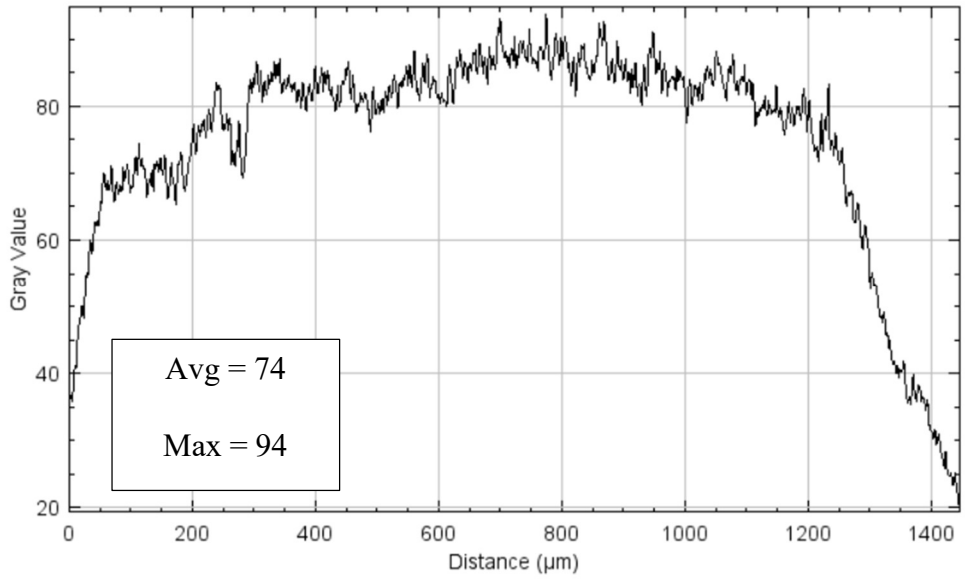

Figure A-1. Gray value vs distance plot of the POM transmission image provided in Figure 3-13, 0° with the polarizer (when the bulk flow side is the upper surface)

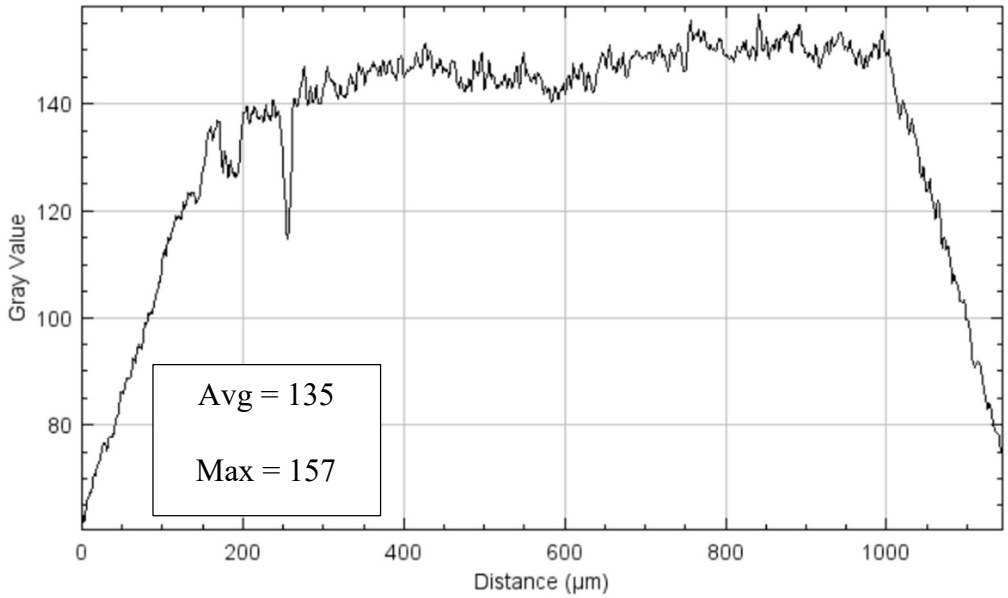

Figure A-2. Gray value vs distance plot of the POM transmission image provided in Figure 3-13, 45° with the polarizer (when the bulk flow side is the upper surface)

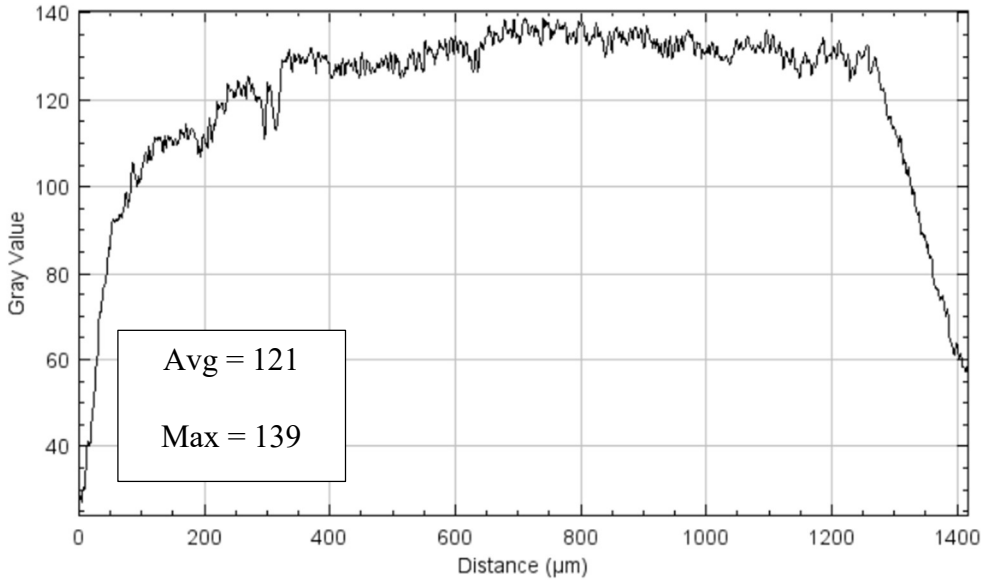

Figure A-3. Gray value vs distance plot of the POM transmission image provided in Figure 3-14, 0° with the polarizer (when the support membrane side is the upper surface)

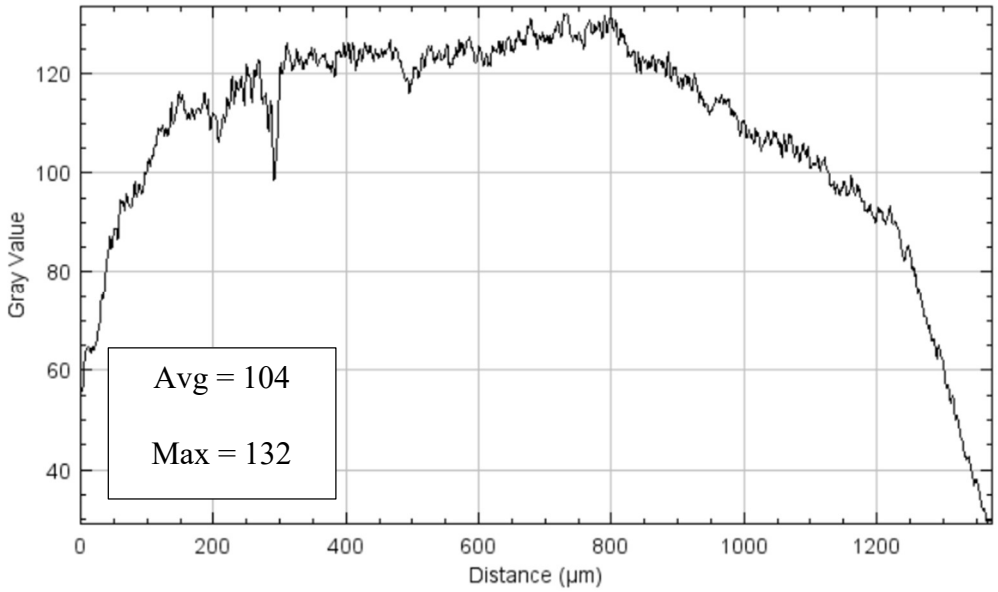

Figure A-4. Gray value vs distance plot of the POM transmission image provided in Figure 3-14, 45° with the polarizer (when the support membrane side is the upper surface)

B. Calculation of Pitch Size and Wavelength of Bragg Reflection

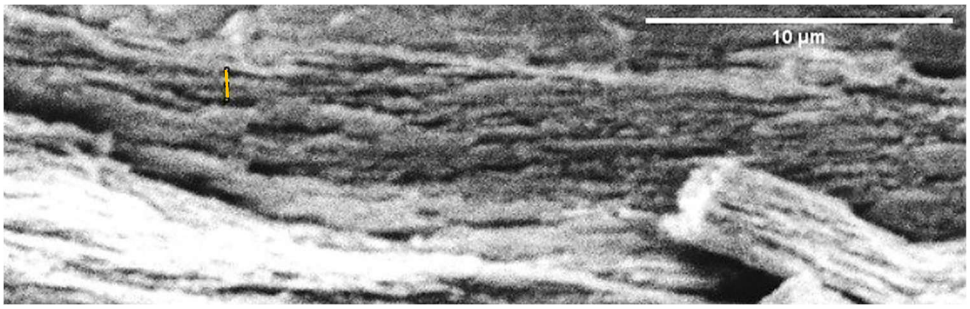

Figure B-1. Cross-section SEM image of the dried sample prepared with the deposition of 0.30% TEMPO-CNC without NaCl. Scale bar is 10 µm. Yellow line represents the cholesteric pitch.

As seen in Figure B-1, the cholesteric pitch of the sample prepared with 0.30% TEMPO-CNC and 0 mM NaCl was measured, and it was found to be 0.912±0.08 µm. This is almost equal to 912 nm. As previously mentioned, the average refractive index of TEMPO-CNC films can be taken as 1.56. Since the incident light is perpendicular to the film surface, the angle between them is 90°. Then, Bragg reflection formula (Equation 9) can be utilized to calculate the reflection range:

$$\lambda = 2n \times (p/2) \times sin\theta$$

$$\lambda = 2 \times 1.56 \times (912/2)\ nm \times \sin(90°)$$

$$\lambda = 1423\ nm$$

The wavelength of the reflected light was found to be 1423 nm that is in the NIR region in the light spectrum.

C. Estimation of Limiting Flux

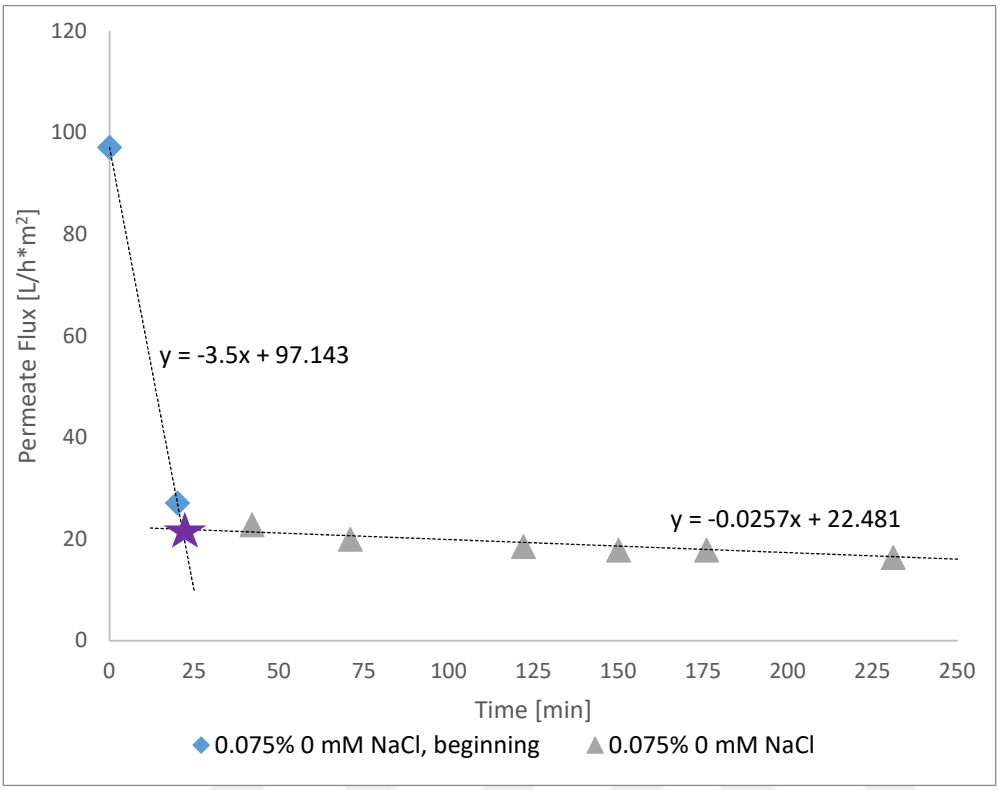

Figure C-1. Data fitting for 0.075% TEMPO-CNC with 0 mM NaCl to estimate the limiting flux. Purple star represents the cross-sections of two functions which is the limiting flux for this case.

For the calculation of limiting flux, the y-intersection point of two lines should be calculated. For that calculation, the x-intersection point should be known, and it can be calculated as the following:

$$y_1 = (slope_1 \times x) + intercept_1$$

$$y_2 = (slope_2 \times x) + intercept_2$$

$$x - intersection = \frac{intercept_2 - intercept_1}{slope_1 - slope_2}$$

By inserting the values :

$$x - intersection = \frac{22.5 - 97.1}{(-3.50) - (-0.03)} = 21.5\ min$$

Then , y-intersection can be found by inserting this value into one of the functions:

$$y - intersection = (slope_1 \times x - intersection) + intercept_1$$

By inserting the values, the limiting flux for 0.075% TEMPO-CNC with no NaCl was found as follows:

$$y - intersection = (-3.50 \times 21.5) + 97.1 = 21.9 \frac{L}{h \times m^2}$$

$$J_{limiting} = 21.9 \frac{L}{h \times m^2}$$

D. TGA Profile of a Representative Sample

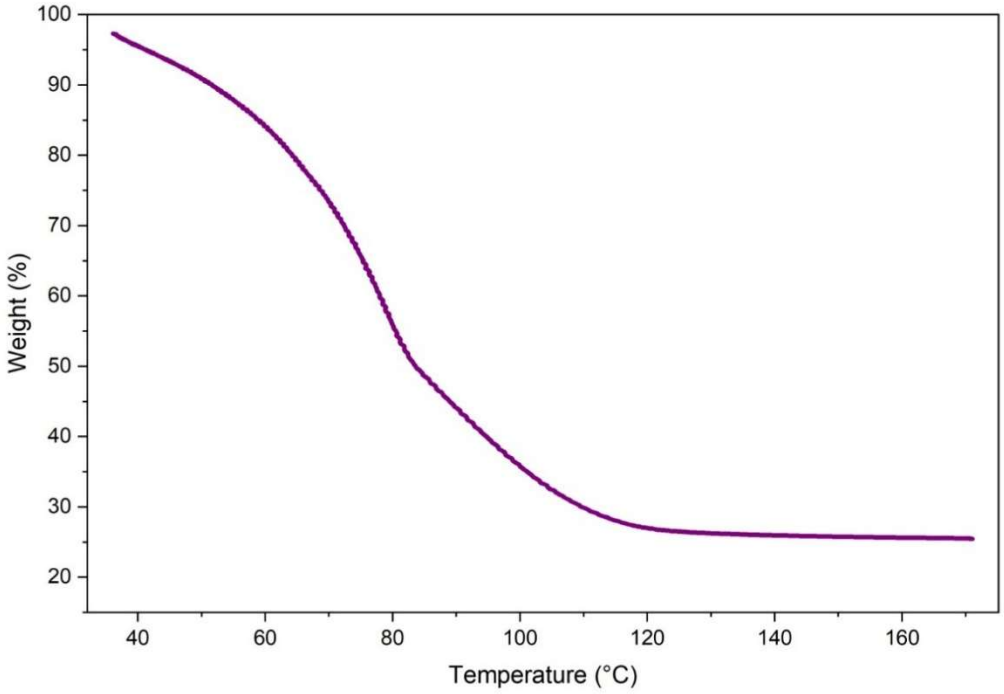

Figure D-1. TGA plot of the sample prepared with the deposition of 0.15% TEMPO-CNC with no NaCl

E. Conversion of Volume-Based Solid Content to Weight-Based Solid Content for a Representative Sample

In order to convert volume-based solid contents to weight-based solid contents, the skeletal and pore densities of TEMPO-CNC samples should be known. The solid parts of TEMPO-CNC cakes have a density of approximately 1.6 g/cm^3 (Rodionova et al., 2012; Volkan, 2020). Since the pores of TEMPO-CNC cake layers are filled with water, the pore density can be taken as 1 g/cm^3. Then, the weight-based solid contents of the cakes can be calculated with the following equation:

$$SC_{wt} = \frac{\rho_{TEMPO-CNC}(1-\varepsilon_{vol})}{\rho_{TEMPO-CN}\ (1-\varepsilon_{vol}) + (\rho_{pore})(\varepsilon_{vol})}$$

For the sample prepared with 0.15% TEMPO-CNC without NaCl, the volume-based porosity was found to be 0.69 by Kozeny-Carman equation. After substituting this porosity and aforementioned densities in the previous equation, the weight-based solid content can be calculated as the following:

$$SC_{wt} = \frac{1.6\ \frac{g}{cm^3}(1-0.69)}{1.6\ \frac{g}{cm^3}(1-0.69) + \left(1\ \frac{g}{cm^3}\right)(0.69)} = 0.418$$

Finally, the weight-based solid content can be reported as percentage:

$$SC_{wt}(\%) = 0.418 \times 100 = 41.8\%$$